Isosteric design of friction-reduction and anti-wear lubricant additives with less sulfur content

Galvanically induced potentials to enable minimal tribochemical wear of stainless steel lubricated with sodium chloride and ionic liquid aqueous solution

TSINGHUA UNIVERSITY PRESS

Springer

PIIJ

Contents

REVIEW ARTICLE

Adhesion and surface forces in polymer tribology—A review

Nikolai MYSHKIN[1]**, Alexander KOVALEV**[2,*]

[1] *Metal-Polymer Research Institute of Belarus National Academy of Sciences, Gomel 246050, Belarus*

[2] *State Key Laboratory of Tribology, Tsinghua University, Beijing 100084, China*

© The author(s) 2018. This article is published with open access at Springerlink.com

Abstract: Polymer tribology is a fast growing area owing to increasing applications of polymers and polymer composites in industry, transportation, and many other areas of economy. Surface forces are very important for polymer contact, but the real origin of such forces has not been fully investigated. Strong adhesive interaction between polymers leads to an increase in the friction force, and hence, the asperities of the material may be removed to form wear particles or transfer layers on the counterface. The theory of polymer adhesion has not been completely elucidated yet and several models of adhesion have been proposed from the physical or chemical standpoints. This paper is focused on the research efforts on polymer adhesion with emphasis on adhesion mechanisms, which are very important in the analysis of polymer friction and wear.

1 Introduction

The fundamentals of tribology are based on mechanics, surface physics, and chemistry [1–3]. For tribological applications of polymers, the dynamic contact inter-action is crucial, and contact adhesion and deformation are affected by roughness, hardness, and surface forces [4–8].

The behavior of polymers in the bulk is dependent on their viscoelastic properties [9, 10]. Contact pressure, velocity, and temperature are the main parameters affecting the performance of polymers at friction. These factors determine the formation of the real contact area, coefficient of friction, and wear of the contacting bodies [4, 11–14].

It is generally accepted that friction is mainly governed by two types of interaction: deformation and adhesion. Derjaguin [15] was the first to discuss both factors in his model of friction. Subsequently, this concept was developed further by Bowden and Tabor, along with their co-authors [1, 9] in Cambridge (UK), and by Kragelskii et al. [16] in Moscow (Russia).

Nowadays, these ideas are receiving both experimental support and theoretical justification in many research papers [2, 17–19]. However, the basic problem in this regard is the difficulty in distinguishing deformation and adhesion components [16, 20–22]. Accordingly, the relevant discussion is ongoing [2, 7, 8, 23, 24].

Theories involving the Lennard–Jones potential are prominent as they are based on the assumption that attraction and repulsion forces act between approaching single charged particles, and hence, forces of electrostatic origin become equal at equilibrium distance. The theory proposed by Lifshitz [25] is more general and accordingly, attraction occurs owing to the overlapping electromagnetic fields of the surfaces in contact. There are several simplifications widely used in polymer surface science, facilitating the estimation of the specific surface energy [26–28].

Owing to rapid progress in nanotechnology, the understanding of the surface contact of polymers has become a fundamental issue for further development of new polymer-based materials and their applications.

---

* Corresponding author: Alexander KOVALEV, E-mail: akovalev@tsinghua.edu.cn

2 Adhesion phenomenon

The adhesion force is defined as the maximum force required for separating contacting surfaces. There is a dual opinion on the nature of adhesion [1, 29–32]. First, it is defined as the attraction resulting in the formation of bonds between solids. Second, adhesion is considered as the force necessary to rupture interface bonds when bodies are separated. The complicated nature of adhesion has been studied extensively [6–8, 33]. Further, the surfaces forces—attractive and repulsive ones—operate between the atoms or molecules of mating surfaces. These forces neutralize each other at some equilibrium separation h_0. If the distance between the surfaces is $h<h_0$, the repulsive force is dominant; otherwise, if $h>h_0$, the attractive force is dominant.

It is generally accepted that a polymer surface operates with a counterbody mainly through van der Waals and electrostatic interactions (see Figs. 1(a) and 1(b)). The orientation, ionic dispersion, induction, and hydrogen intermolecular bonds may be generated within the polymer interface.

A hydrogen bond is formed at very short distances between polymer molecules containing the functional groups OH, COOH, NHCO, etc. The hydrogen atom of the molecule can be linked with an electronegative atom of other polymer molecules. Under favorable conditions, two contacting molecules are bonded together by a common electron, providing a strong and stable combination [34].

Owing to the direct interaction of contacting polymer surfaces, physisorption and direct molecular bonding coexist within the real contact spots as shown in Fig. 1(c). The adsorption of polymer molecules occurs because molecular bonds are formed owing to the existence of energy instability in the contact interface.
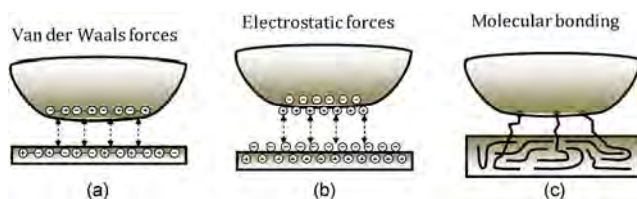
Fig. 1 General types of an adhesion interaction in the polymer interface (adopted from Ref. [35]).

The chemisorption of polymer chains is explained by the appearance of strong chemical bonds at the contact points. Chemical bonds are considerably stronger than intermolecular bonds within the polymer interface.

2.1 Thermodynamic surface energy

The interfacial energy of a polymer is one of the most fundamental parameters characterizing its surface state. Depending on the temperature and molecular weight, polymers can be in liquid or solid state. If two substances interact directly with each other, the molecules of one must come to interplay with the other. In the case of long-chain polymer molecules, some tiles of molecules are adsorbed onto the opposite surface. This is an exothermic process as can be readily represented with a simple thermodynamic argument. The free energy of molecular adsorption dG is written as follows:

$$dG = dH - TdS \tag{1}$$

where dH is the enthalpy, T is the temperature, and dS is the change of entropy. Generally, the energy change, dW, required to increase the surface by the unit area, dA, is proportional to the specific surface energy

$$\gamma = \frac{dW}{dA} \tag{2}$$

The work of adhesion interaction between solids 1 and 2, which is equal to the work of adhesion rupture, is determined by the Dupre formula

$$\gamma = \gamma_1 + \gamma_2 - \gamma_{12} \tag{3}$$

where γ_1 and γ_2 are the energies required to form the unit surfaces of solids 1 and 2 (their free surface energy) and γ_{12} is the excessive or interfacial energy.

The equation governing the energy balance of microscopic solid/liquid/gas interface is Young's equation

$$\gamma_{sl} = \gamma_{sv} + \gamma_{lv} \cos\theta \tag{4}$$

where θ is the contact angle and subscripts s, v, and l correspond to the solid, vapor, and liquid phases, respectively.

2.2 Electric double layer

In some instances, intrinsic adhesion arises owing to an electric double layer (EDL) formed between materials with dissimilar electronic band structures [36]. These forces are attributed to the free transfer electrons within the polymer interface. The idea of the formation of an EDL at the interface between the surfaces in contact was first advanced by Helmholtz. The mechanisms responsible for the formation of EDL in an interface vary, ranging from direct electron transfer under donor–acceptor interaction to polarization effects. This results in positive and negative surface charge attract each another [20]. However, this approach has a serious disagreement on the magnitude of electrostatic attraction under certain conditions [37]. Some researchers have determined that electrostatic interaction mainly depends on environmental conditions and can significantly influence the contribution to adhesion [38]; others believe that these forces are dominant [39].

The EDL model of contact proposed by Derjagin and Toporov [39] describes the adhesion owing to contact electrification in an EDL appearing at the boundary of two phases in the form of an electric capacitor. In a frame of this theory, for the elastic sphere–plane contact surface, the effective molecular interaction is given by $F_m = AR/6\varepsilon^2$, where ε is the minimal distance of separation of the surfaces (a quantity of the order of a molecular diameter), R is the sphere radius, and A is the Hamaker constant.

Moreover, the elastic compliance follows the Hertz theory. It is evident that repulsion must overcome the interaction arising from the EDL charges in the annular zone around the points of contact. The electrostatic component (F_e) of this interaction is expressed as the derivative of the energy of interaction between the charges on the deformed portion of the spherical particle and the charge on the planar base, and its value is calculated using the Hertz theory. The ratio between the electrostatic component and molecular interaction F_m is proportional to the elastic reaction of the surface and is written as

$$\frac{F_e}{F_m} = \frac{3\pi^2 \sqrt[3]{2}}{2} \left(1-\nu^2\right)^{2/3} \sigma^2 \left(\frac{R\varepsilon^2}{AE^2}\right) \tag{5}$$

where ν is Poisson's ratio, E is elastic modulus, and R is the radius of the spherical particle.

Confirmation of the electrical theory of adhesion can be found in the electrification of the delaminated surfaces, luminescence, and characteristic discharge, in addition to the process of electron emission. However, the electrical theory provides a poor explanation for the adhesion of polymers between themselves.

3 Direct measurements of surface forces

The measurement of the molecular forces between solid surfaces is one of the most important challenges in surface science [14, 25]. As the forces are weak and their action radius is short, the measuring instruments should satisfy specific requirements. The first correct measurement of molecular attraction between solids was conducted by Derjaguin and Abrikosova in 1951 [40]. They determined an elegant solution to detect attraction force. An active feedback scheme was realized to stabilize the distance between solids. Subsequently, many other methods have been developed to measure the surface energies of polymers directly. In the following short survey, experimental data on polymer adhesion measured using surface force apparatus (SFA), atomic force microscope (AFM), and contact adhesion meter (CAM) are summarized.

3.1 Surface force apparatus

The surface force apparatus allows direct measurement of the molecular forces in liquids and vapors at the Ångström resolution level [41]. The classical design of SFA contains two crossed atomically smooth mica cylinders between which the interaction forces are measured [42]. One cylinder is mounted to a piezoelectric transducer. The other mica cylinder is mounted to a spring with a known and adjustable spring constant. The separation between the two surfaces is measured optically using multiple beam interference fringes as schematically shown in Fig. 2. In the case of studying polymers, the thin polymer film is deposited on the mica surface.

SFA has been widely used to measure both normal and lateral forces between surfaces in vapors and liquids for many types of materials. Further, SFA is
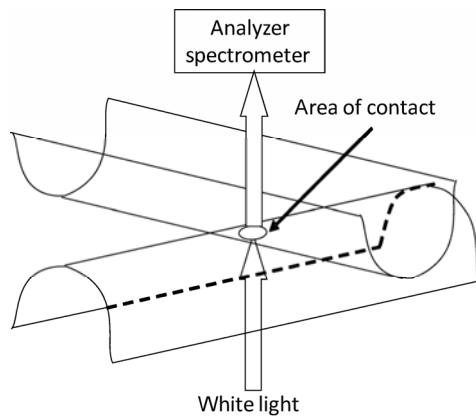
Fig. 2 Sketch of measurement of interfacial forces realized in SFA.

capable of measuring the dynamic interactions and time-dependent interfacial effects. SFA measures forces as a function of absolute surface separation between the contact surfaces. The force sensitivity is ~1 nN and the distance resolution is less than 0.1 nm.

3.2 Atomic force microscopy

In recent years, atomic force microscopy (AFM) has been widely used to investigate polymers. The main capabilities of AFM are surface imaging, thickness measurement [43], probing of surface mechanical properties [44], and direct measurement of surface forces using force–distance curve technique [45].

AFM is a powerful device for the investigation of surface properties at the nanoscale [46]. The major application of AFM is the measurement of the tip–sample interaction using force–distance curves. AFM force–distance curves have been used for the study of numerous material properties and for the characterization of surface forces. A force–distance curve directly reflects the relationships between the interfacial tip–polymer interactions and mechanical properties of the polymer. The schematic representation of adhesion measurements is discussed in detail elsewhere [45]. The dependence of cantilever deflection and distance at approaching and retracing is schematically shown in Fig. 3. The jump-off occurs when the adhesion force is overcome by the elastic deflection of the cantilever. The corresponding value of force $F_{\text{pull-off}}$ is assumed to be an adhesion force.

As both attractive and repulsive forces localized over nanometer scale regions can be probed, forces
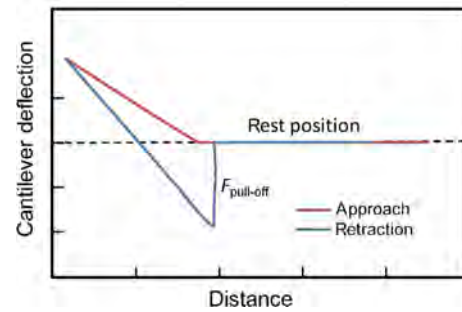
Fig. 3 Schematic representation of an AFM force-displacement curve showing the typical behavior of cantilever at tip-sample interaction.

owing to negative loading of the probe from the van der Waals attraction between the tip and sample prior to contact, or from adhesive forces occurring subsequent to contact can be investigated.

3.3 Contact adhesion meter

The available evaluations of molecular forces correspond to the sensitivity of an analytical balance. The main problem is that the force increases rapidly with the decrease of the distance between the specimens under testing. Hence, the measurements should be carried out at a very small speed, which cannot be implemented technically using the design of a common balance. Derjaguin et al. [47, 48] proposed to use a feedback balance. This principle was successfully realized in a contact adhesion meter (CAM). This device was designed at Metal-Polymer Research Institute (MPRI), Gomel, Belarus. Figure 4 shows a view of CAM
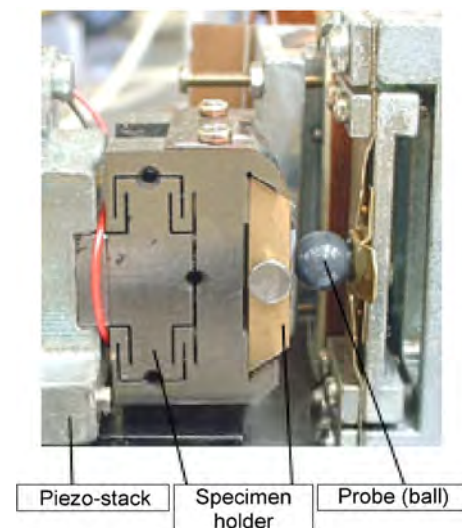
Fig. 4 Photograph of a measure unit realized in CAM device.

detecting unit where the silicon ball and silicon wafer were used in the experiments.

The measurement was realized as follows. The probe is moved toward or away from a surface within the nanometer range using a piezo-stack and the force is registered with a gage fixed on the free arm of a highly sensitive electromagnetic balance. When the probe approaches the surface, the attraction force is recorded. Once the probe touches the test surface, it does not stop and continues moving until a few nanometers are passed. Over this distance, the repulsion force acting between the contacting bodies is recorded.

4 Contact theories considering adhesion

The basics of contact mechanics are used for the explanation of elastic contact and tribological behavior of polymers [31]. The real and nominal contact areas are determined based on solutions to the problems of the theory of elasticity and classical Hertz theory of contact.

Contact mechanics uses two generally accepted theories of adhesion contact involving the surface energy as the measure of attraction between solids. They are the JKR (Johnson–Kendall–Roberts) [27] and DMT (Deryagin–Muller–Toporov) [49] models. Borodich [28] conducted a comparative analysis of these models and concluded that the basis of calculation of adhesion contact of elastic bodies for both models was based on Derjaguin's idea for the calculation of the total energy in adhesion contact, published in 1934 [50].

4.1 Johnson–Kendall–Roberts model

The Johnson–Kendall–Roberts (JKR) model [27] is based on the assumption of infinitely small radius of surface forces. It is assumed that interactions occur only within the contact area. The elastic contact between a sphere of radius R and half-space is analyzed with the consideration of van der Waals forces operating together with the applied external load. The contact stiffness is resistant to the action of the forces.

The formula for calculating the radius of adhesive contact in the JKR model is

$$a^3 = \frac{3}{4}\frac{R}{E^*}\left(F + 3\pi R\gamma + \sqrt{6\pi RF\gamma + (3\pi R\gamma)^2}\right) \quad (6)$$

where F is the normal load and E^* is the effective elastic modulus.

Therefore, it is apparent that, without adhesion ($\gamma = 0$), the Hertz equation is obtained, whereas if $\gamma > 0$, the contact area always exceeds the Hertzian contact area under the same normal load F.

Only the application of a tensile (negative) load can reduce this radius, and thereafter, the contacting surfaces would be separated at the load corresponding to the conversion of the radicand to zero:

$$F_{\text{pull-off}} = -\frac{3}{2}\pi R\gamma \quad (7)$$

This equation describes the pull-off force required to separate contact bodies. It depends on the specific surface energy γ and is independent of the elastic properties of solids.

4.2 Derjaguin–Muller–Toporov model

The Derjaguin–Muller–Toporov (DMT) model [49] describes the contact of elastic sphere with a rigid half-space. This model is based on the following two postulates: surface forces do not change the deformed profile of the sphere and it remains Hertzian; the attraction force acts outside the contact circle while the contact is under compression by the stresses distributed according to Hertz.

Equilibrium is reached if the deformation is sufficient for the elastic response (restoration of the sphere) F_e to counterbalance the joint effect of the applied external load F and the forces of molecular attraction F_s, i.e.,

$$F_e = F + F_s \quad (8)$$

The DMT model leads to adhesive (tensile) stresses that are finite outside the contact zone but zero inside, resulting in a stress discontinuity at the edge of the contact zone. The relation between the load and approach obtained for the conditions of the DMT model is given as

$$F_e = F - 2\pi\int_0^\infty R\mathrm{d}h(r)\frac{\mathrm{d}V}{\mathrm{d}h} \quad (9)$$

where R is the radius of contacting sphere, $h(r)$ is the gap between bodies, and $V(h)$ is the interaction potential.

The separation of surfaces occurs at the maximal adhesion force of

$$F_{adh} = 2\pi R \gamma \qquad (10)$$

The DMT and JKR theories predict different adhesion force interactions for identical solids and conditions, which has resulted in long-lasting discussion. Tabor compared the JKR and DMT theories and pointed out their main drawbacks [51] and Maugis proposed a unified model for elastic contacts [52].

4.3　Contact of rough surfaces considering adhesion

In 1940, Zhuravlev published the pioneering work related to contact mechanics, where the statistical approach for describing surface roughness was proposed. He considered a linear distribution of heights of aligned spherical asperities and obtained an almost linear relation between the external load F and real contact area A_r. A historical paper by Zhuravlev has been translated by Borodich [53].

The well-known Greenwood–Williamson model [54] is assumed to predict the real contact area (RCA) of formation of rough solids and local pressure distribution. However, an in-depth analysis indicates that it is impossible to study the contact of polymers unless the molecular interactions between the surfaces are considered [31]. In 1975, Fuller and Tabor published a classic paper on the adhesion between elastic solids and the effect of roughness in reducing the adhesion [55]; it was also concluded that a relatively small surface roughness could completely remove the adhesion interaction. The effect of intermolecular forces can be tentatively assessed using the adhesion parameter proposed by Tabor as follows:

$$\Delta_C = \frac{1}{3\sigma}\left(\frac{9\pi R^{1/2}\Delta\gamma}{8E}\right)^{2/3} \qquad (11)$$

where σ is the root-mean-square parameter of asperity distribution and R is the average radius of asperities. The estimation of the adhesion forces shows that the discrete contact is highly sensitive to its adhesion ability [30]. Hence, larger magnitudes of Δ_C can increase the RCA more than 100 times. The relation $\Delta_C < 0.1$ can occur only if at least one of the contacting bodies is completely elastic. Theoretical and experimental studies have shown that contact is formed by adhesion and surface forces are dominant when $\Delta_C > 0.1$.

The condition $\Delta_C \geq 0.1$ can determine the ultimate mean arithmetic deviations of the equivalent roughness Ra = $(Ra_1 + Ra_2)^{1/2}$ below which the degree of adhesion in the contact should be considered. This correlation is shown in Fig. 5.

A transition region exists above this level when the condition $\Delta_C > 0.1$ is fulfilled only for a certain combination of properties of contact materials. Hence, each specific case requires validation. This analysis indicates that it is impossible to study the contact of any materials at nanoscale unless the atomic and molecular interactions between the surfaces are considered.

5　Experimental results and discussion

Several types of adhesive forces operate within polymer–solid interfaces. A correct analysis of adhesive forces is a crucial challenge in the tribology of polymers [12, 14, 35]. Strong adhesion interaction between the contacting asperities of sliding surfaces is mainly accompanied by the following effects: frictional force is increased and the material may be removed from the surface to form wear particles or transfer layers. The removal of the external load results in a complete or partial restoration of the shape of the surfaces and the corresponding disintegration of the adhesion bonds. This renders it difficult to determine quantitatively the
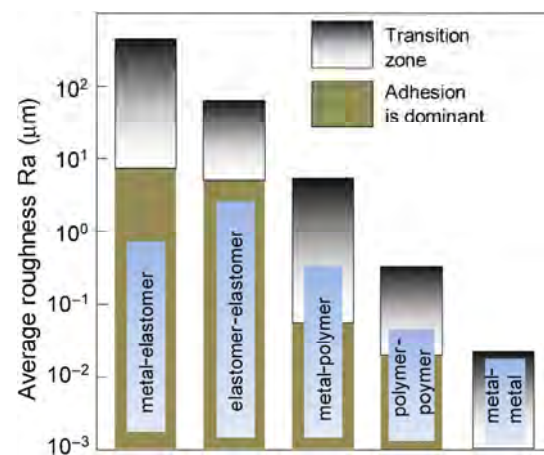

Fig. 5　Influence of adhesion interaction within contact of rough surfaces.

strength of the adhesion interaction for contacting polymers.

The adhesion of a surface has strong relation to its wetting [56–58]. A common method of observing surface wetting is to measure the contact angle as the edge angle of the liquid droplet in contact with the solid surface. It indicates the energetic balance between the solid, liquid, and gas phases involved. Contact angles for some polymers are listed in Table 1. One can conclude that their values for certain polymers can significantly vary. The diffusion of long-chain polymers has been the subject of intense research activity in the last decade but the nature of this process is still not clear [8, 57].

In the case of low surface energy of solids, high adhesion bonding is usually explained by the contribution of chemical interaction to the adhesion bonding. However, the real origin of "chemical interaction" remains unclear in certain cases. For example, Derulle at al. [62] examined the interaction between elastomeric lens of cross-linked poly(dimethyl-siloxane) (PDMS) and a silicon wafer covered with a grafted layer of monodisperse PDMS. It was observed that the work of adhesion was higher than that expected by considering only the surface energy of PDMS. The adhesion energy was measured to be approximately 80 mJ/m^2, which is higher than the value of 45 mJ/m^2, the expected value for symmetrical PDMS-PMMS. Generally, segments of PDMS elastomer can be adsorbed onto silica if they find their way to the wafer surface. Accordingly, increasing the grafting

density and thereby capping more hydroxyl groups on the silica surface should lead to the decrease of interfacial energy. However, this has not been observed in this experiment.

Mangipudi used SFA to measure the surface energies of PET and PE, and the interfacial energy between them. He also reported the increase in the surface energy of PE from 33 up to 56 mJ/m^2 after corona-treatment procedure [63]. Tirrell [26] analyzed SFA data on adhesion force and applied the JKR model for the estimation of adhesion contact for polymers. Using SFA, Chen et al. [56] studied the adhesion of glassy polystyrene (PS) and poly(vinylbenzyl chloride) (PVBC) surfaces with various molecular weights. It was observed that cross-linking of high-molecular-weight polymers leads to lower adhesion. The surface energy was approximately 38 mJ/m^2 for PS and approximately 50 mJ/m^2 for PVBC. A friction is relative to the untreated polymers, whereas scission (bond-breaking) leads to higher adhesion, showing the surface energy hysteresis of approximately 13.5 mJ/m^2. It is associated with the interdiffusion point of view, which supposes that the chains cross the interface and diffuse into the other medium. Selected experimental results on the work of adhesion probed using SFA are listed in Table 2.

Adhesion hysteresis [64, 65] has often been observed in polymer materials. In hysteretic systems such as polymers of low molecular weight, the loading and unloading paths are not the same, as observed for polystyrene-*graft*-poly-(ethylene oxide) (PS-g-PEO) [66]. The use of the JKR model for the loading

Table 1 Values of contact angle measured on polymer surface (liquid is water).

Material	Contact angle, θ(°)	Reference
Polytetrafluoroethyene (PTFE)	105, 112	[60, 56]
Polyethylene (PE)	86, 103, 33	[26, 56, 60]
Nylon-6	65	[60]
Polyvinylcyclohexane (PVCH)	29	[26]
Poly-4-methyl-1-pentene (TPX)	26	[26]
Polysterol (PS)	30, 90	[26, 61]
Polymethylmethacrylate (PMMA)	53	[26]
Polyethylene terephthalate (PET)	38	[26]
Poly-2-vinylpyridine (PVP)	50	[26]
Polyvinylbenzyl chloride (PVBC)	88	[61]

Table 2 Selected results on work of adhesion measured by means of SFA.

Polymer	Work of adhesion, γ(mJ/m^2)	References
Polyethylene terephthalate (PET)	61	[26]
Polyethylene (PE)	32 (56)	[63]
Polyvinylcyclohexane (PVCH)	28	[26]
Poly-4-methyl-1-pentene (TPX)	21	[26]
Poly-methyl methacrylate (PMMA))	40	[26]
Polysterol (PS)	44, 38	[26, 61]
Poly-2-vinylpyridine (PVP)	63	[26]
Polyvinylbenzyl chloride (PVBC)	50	[61]
Polydimethylsiloxane (PDMS)	80 (45)	[61]

path yields γ = 37.0 mJ/m^2, which corresponds to the thermodynamic surface energy of the PS-g-PEO film. An analysis of the unloading path yields the adhesion force of $\gamma \approx$ 47.7 mJ/m^2, resulting in the adhesion hysteresis $\Delta\gamma$ of 10.7 mJ/m^2. The adhesion hysteresis of PS-g-PEO surfaces is explained mainly by the interdigitation of polymer chains/segments across the contact interface, and the hydrogen bonding between the PEO chains at the polymer–polymer interface should also be considered [67].

Taylor measured the energies between various polymer layers and crystal 1,3,5-trinitro-1,3,5-triazacyclohexane (RDX) [68]. It was observed that the specific surface energy varies depending on the crystallinity of polymers. The influence of the substrate on the adhesion of polymers should also be considered. Ahn and Shull [10, 69] observed that the adhesion of methylated PNBA (m-PNBA), carboxylated PNBA (c-PNBA), and neutralized PNBA (n-PNBA) varies depending on the substrates used. An increase in adhesion is attributed to the acid/base interactions at the elastomer/substrate interface and ionized groups, which can increase the relaxation times of the elastomer, presumably owing to the enhanced segmental mobility of molecules.

The values of work of adhesion calculated from the AFM data are listed in Table 3. Polymer brushes have become an important subject of research [6, 70] owing to their unique ability to change the surface property. They are layers of polymer molecules attached to a surface at one end whereas the rest of the molecule chain extends out of the surface. Densely grafted polymer molecules tend to stretch away from the surface in order to reduce their interaction with other molecules, thus attaining a different conformation than the optimal one for the free polymer molecules

in the bulk or solution [71].

Polymer brushes are usually attached to the surface owing to the chemical adsorption of chain ends, resulting in a polymer layer of nanometer thickness [72]. In the case of a functionalized polymer chain, a copolymer layer of nanometer thickness can also be generated on a surface [73–75]. The technique of preparation and deposition of self-assembled molecular layer (SAM) is described in detail elsewhere [76–77]. A comparative analysis of adhesion and friction forces of DDPO$_4$ (dodecylphosphoric acid ester), ODPO$_4$ (octadecylphosphoric acid ester), and OTS (octadecyltrichlorosilane) revealed a significant effect of polymer brushes on friction at light loads [78]. Such tailoring may be of utmost importance for controlling the interaction between the polymer brushes and biological systems such as proteins and cells.

Figure 6 shows the typical dependence of adhesion force during approaching and retracting of a silicon ball to the OTS polymer nanolayer obtained using CAM. For DDPO$_4$ and ODPO$_4$ SAMs, the initial silicon substrates were covered with Ti or TiO$_x$ interlayers. Polymer nanolayers on metal oxides are of particular interest to biomaterials and biosensors. They allow the tailoring of surface properties. Experimental data on polymer brushes and substrates are summarized in Table 4 [79]. If the characteristics of the adhesion force of the probe are known, the specific surface energy of the polymer nanolayers can be estimated based on the experimental data. The maximal attraction force P_{max} was determined from the experimental curve. The calculation of γ was based on the DMT

Table 3 Work of adhesion for polymers measured by AFM.

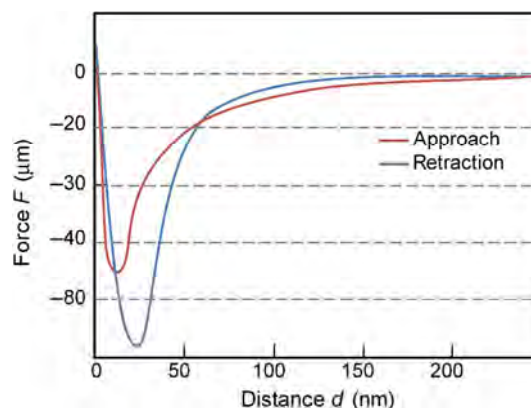| Polymer	Work of adhesion, γ (mJ/m^2)	Reference
Polyethylene (PE)	81	[68]
Polypropylene (PP)	76	[68]
Polystyrene (PS)	92	[68]
Polyvinylidene fluoride (PVDF)	69	[68]
Polychlorotrifluoroethylene (PCTFE)	64	[68]
Polytetrafluoroethyene (PTFE)	58	[68]

Fig. 6 An example of experimental force-distance curves measured by means of CAM (adopted from Ref. [78]).

Table 4 Adhesion characteristics of polymer brush layers measured by CAM.

Material (substrate)	Attraction force P_{max} (μN)	Attraction distance h (nm)	Specific surface energy γ (mJ/m^2)
Silicon ball of 1 mm radius			
ODPO$_4$ (TiO$_x$)	99	91	6.7
ODPO$_4$ (Ti)	125	121	11
DDPO$_4$ (Ti)	67	115	1.6
Epoxilane (Si)	33	92	3.8
OTS (Si)	80	115	3.6
Titanium ball of 1.5 mm radius			
Epoxilane (Si)	38	51	2.9
OTS (Si)	12	50	2.4
ODPO$_4$ (TiO$_x$)	34	14	3.5

theory because the thickness of the polymer layer was very small compared with the radius of contact.

Table 4 also lists the measurement results of the characteristics of force field of coatings on the silicon plate paired with the titanium ball. The calculated values of γ for Si and epoxilane (on Si substrate) specimens are very close to those calculated for the interaction of these specimens with the silicon probe in tests with the silicon ball. All the samples show similar dependence of attraction forces on the distance from the sample to silicon ball. Figure 7 shows the adhesion forces normalized with the radius of the indenter in comparison with similar data obtained with AFM and CAM. The data well concise except with AFM pull-off force measurements of Ti and TiO$_x$ samples. This difference can be explained by the
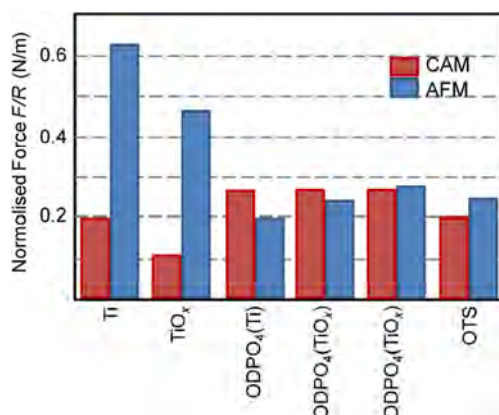
Fig. 7 Comparison of adhesion forces measured with AFM and CAM.

influence of capillary forces and the low hydrophobic properties of the samples. For much bigger size of the indenter of CAM as compared with the AFM tip, capillary forces play a dominant role in the interaction of samples during retraction.

In all the aforementioned examples, the surface adhesion is associated with both physical and chemical contributions of the active chains of polymer molecules. To uniquely distinguish the contribution of given polymer surfaces is an ambiguous task because adhesion interaction slightly depends on the nature of the polymer, but mostly depends on local physical conditions within the real contact, which can activate different types of molecular bonding. The specific molecular activities and certain physical properties of molecular chains more strongly affect the final adhesion force than can be measured using SFA, AFM, or ADM.

Based on the results presented in Tables 1, 2, and 3, we can conclude that the "value" of adhesion interaction still "depends" on the method and device used for measuring adhesion. The confusion in notions, which still plagues scientists, such as the work of adhesion, surface energy, adhesion force, and specific surface energy, influences the conception of adhesion as a physical phenomenon and initiates unnecessary discussions about the veracity of adhesion measurements.

6 Concluding remarks

Significant advances have been made, particularly during the last four decades, in the field of polymer tribology and contact mechanics. Various experimental techniques and theoretical methods have been developed to discover the origin of polymer adhesion.

The classical thermodynamic theory of adhesion cannot be directly applied to polymer systems. According to the experimental results of adhesion of polymers, there are several effects strongly influencing polymer adhesion.

The simplest mechanical approach is to consider interlocking the interaction of surface irregularities on the polymer surface. Other effects are related to the specific molecular activities occurring within the contact area. Cross-linking of the polymer surfaces reduces the adhesion and friction whereas increasing the number of chain ends at the surfaces, via either

scission or addition of short-chain polymers, leads to increased adhesion and friction.

Molecular irregularities also strongly influence the adhesion of polymers. There is partial untwisting of molecules, mutual penetration of polymer molecules resulting in "brush-to-brush" contact, and local cross-linking effect at the interface.

Proper analysis of the adhesion effects in polymer contacts is very important for the fundamentals of polymer tribology owing to the key role played by adhesion in self-lubrication, mass transfer, and wear of polymers and polymer-based materials with increasingly more practical applications in engineering and daily life.

References

[1] Bowden F P, Tabor D. *Friction and Lubrication of Solids*. Oxford (UK): Oxford University Press, 1964.

[2] Myshkin N, Kovalev A. Adhesion and friction of polymers. In *Polymer Tribology*. Sinha S, Briscoe B, Eds. London: Imperial College London, 2009: 3–37.

[3] Myshkin N, Kovalev A, Spaltman D, Woydt M. Contact mechanics and tribology of polymer composites. *Journal of Applied Polymer Science* **131**(3): 3987(1)–3987(9) (2014)

[4] Myshkin N K, Tkachuk D V. Polymer Tribology Fundamentals. In *Encyclopedia of Tribology*. Wang Q J, Chung Y-W, Eds. Boston: Springer US, 2013: 2614–2619.

[5] Kovalev A, Myshkin N. Polymer Contact Mechanics. In *Encyclopedia of Tribology*. Wang QJ, Chung Y-W, Eds. Boston: Springer US, 2013:2570–2577.

[6] Klein J, Briscoe W H, Chen M, Eiser E, Kampf N, Raviv U, Tadmor R, Tsarkova L. Polymer Brushes and Surface Forces. In *Polymer Adhesion, Friction, and Lubrication*. Zeng H, Ed. Hoboken: John Wiley & Sons, 2013: 135–176.

[7] Pollock H M. Surface forces and adhesion. In *Fundamentals of Friction: Macroscopic and Microscopic Processes*. Singer

I L, Pollock H M, Eds. Dordrecht: Springer Netherlands, 1992: 77–94.

[8] Brown H R. The adhesion between polymers. *Annual Review of Materials Science* **21**(1): 463–489 (1991)

[9] Ludema K C, Tabor D. The friction and visco-elastic properties of polymeric solids. *Wear* **9**(5): 329–348 (1966)

[10] Shull K R. Contact mechanics and the adhesion of soft solids. *Materials Science and Engineering: R: Reports* **36**(1): 1–45 (2002)

[11] Zhang S W. State-of-the-art of polymer tribology. *Tribology International* **31**(1–3): 49–60 (1998)

[12] Briscoe B J. Friction of organic polymers. In *Fundamentals of Friction: Macroscopic and Microscopic Processes*. Singer I L, Pollock H M, Eds. Dordrecht: Springer Netherlands, 1992: 167–182.

[13] Briscoe B. Wear of polymers: an essay on fundamental aspects. *Tribology International* **14**(4): 231–243(1981)

[14] Zeng H. Adhesion and friction mechanisms of polymer surfaces and thin films. In *Polymer Adhesion, Friction, and Lubrication*. Zeng H, Ed. Hoboken: John Wiley & Sons, 2013: 391–442.

[15] Derjaguin B. Molekulartheorie der äußeren Reibung. *Zeitschrift für Physik* **88**(9–10): 661–675 (1934)

[16] Kragelskij I V, Dobychin M N, Kombalov V S. *Friction and Wear: Calculation Methods*. Oxford (UK): Pergamon Press, 1982.

[17] Briscoe B J. Interfacial friction of polymer composites. General fundamental principles. In *Friction and wear of polymer composites*. Klaus F, Ed. Amsterdam: Elsevier, 1986: 25–59.

[18] Satyanarayana N, Sinha S K, Shen L. Effect of molecular structure on friction and wear of polymer thin films deposited on Si surface. *Tribology Letters* **28**(1): 71–80 (2007)

[19] Borodich F M, Savencu O. Hierarchical models of engineering rough surfaces and bio-inspired adhesives. In *Bio-inspired Structured Adhesives*. Heepe L, Xue L, Gorb S N, Eds. Cham: Springer, 2017: 179–219.

[20] Bely V A, Sviridenok A I, Petrokovets M I, Savkin V G. *Friction and Wear in Polymer Based Materials*. Oxford(UK): Pergamon Press, 1982.

[21] Olea-Mejia O, Brostow W, Buchman E. Wear resistance and wear mechanisms in polymer plus metal composites. *Journal of Nanoscience and Nanotechnology* **10**(12): 8254–8259 (2010)

[22] Buckley D H, Tribological properties of surfaces. *Thin Solid Films* **53**(3): 271–283 (1978)

[23] Friedrich K, Reinicke P. Friction and wear of polymer-based composites. *Mechanics of Composite Materials* **34**(6): 503–514 (1998)

[24] Friedrich K, Lu Z, Hager A M. Recent advances in polymer composites tribology. *Wear* **190**(2): 139–144 (1995)

[25] Israelachvili J N. *Intermolecular and Surface Forces*. Elsevier, 2011.

[26] Tirrell M. Measurement of Interfacial Energy at Solid Polymer Surfaces. *Langmuir* **12**(19): 4548–4551 (1996)

[27] Johnson K L, Kendall K, Roberts A D. Surface energy and the contact of elastic solids. *Proceedings of the Royal Society A* **324**(1558): 301–313 (1971)

[28] Borodich F M. The Hertz-type and adhesive contact problems for depth-sensing indentation. *Advances in Applied Mechanics* **47**: 225–366 (2014)

[29] Myshkin N K, Kovalev A V. Adhesion and friction of polymers. In *Polymer Tribology*. Sinha S K, Briscoe B J, Eds. London: ImperialCollege Press, 2009: 3–37.

[30] Myshkin N K, Petrokovets M I, Chizhik S A. Basic problems in contact characterization at nanolevel. *Tribology International* **32**(7): 379–385 (1999)

[31] Myshkin N K, Petrokovets M I. Mechanical behavior of plastics: surface properties and tribology. In *Mechanical Tribology, Materials, Characterization, and Applications*. Totten G, Liang H, Eds. New York: Marcel Dekker, 2004: 57–94.

[32] Myshkin N K, Petrokovets M I, Kovalev A V. Tribology of polymers: Adhesion, friction, wear, and mass-transfer. *Tribology International* **38**(11–12): 910–921 (2005)

[33] Derjaguin B V, Rabinovich Y I, Churaev N V. Direct measurement of molecular forces. *Nature* **272**(5651): 313–318 (1978)

[34] He Y, Zhu B, Inoue Y. Hydrogen bonds in polymer blends. *Progress in Polymer Science* **29**(10): 1021–1051 (2004)

[35] Kovalev A, Sturm H. Polymer adhesion. In *Encyclopedia of Tribology*. Wang Q J, Chung Y-W, Eds. Boston: Springer, 2013: 2551–2556.

[36] Deryagin B V, Krotova N A, Smilga V P. *Adhesion of Solids*. New York (US): Consultant Bureau, 1978.

[37] Barouch E, Matijević E, Parsegian V A. The accuracy of the Derjaguin approximation for the electrostatic double-layer interaction between curved surfaces bearing constant potentials. *Journal of the Chemical Society, Faraday Transactions 1: Physical Chemistry in Condensed Phases* **82**(9): 2801–2809 (1986)

[38] Joly L, Ybert C, Trizac E, Bocquet L. Hydrodynamics within the electric double layer on slipping surfaces. *Physical Review Letters* **93**(25): 257805 (2004)

[39] Deryagin B V, Toporov Y P. Role of the electric double layer in adhesion. *Bull Acad Sci USSR Div Chem Sci* **31**(8): 1544–1548 (1982)

[40] Derjaguin B V, Abrikossova I I. Direct measurement of the molecular attraction as a function of the distance between spheres. *Zhurn Eksp Teor Fiz* **21**: 945–946 (1951)

[41] Israelachvili J N, Tabo rD. The measurement of van der Waals dispersion forces in the range 1.5 to 130 nm. *Proceedings of the Royal Society of London A* **331**(1584): 19–38 (1972)

[42] Tian Y, Surface Force Apparatus .In *Encyclopedia of Tribology*. Wang Q J, Chung Y-W, Eds. Boston: Springer, 2013: 3431–3434.

[43] Adhikari S, Frankel G S, Bammel B D, Zimmerman J. AFM scratching for adhesion studies of thin polymer coatings on steel. *Journal of Adhesion Science and Technology* **26**: 1591–1609 (2012)

[44] Kovalev A, Shulha H, Lemieux M, Myshkin N, Tsukruk V. V. Nanomechanical probing of layered nanoscale polymer films with atomic force microscopy. *Journal of Materials Research* **19**(3): 716–728 (2004)

[45] Cappella B, Dietler G. Force-distance curves by atomic force microscopy. *Surface Science Reports* **34**(1–3): 1–104 (1999)

[46] Brogly M, Noel O, Castelein G, Schultz J. Adhesion at the nanoscale: an approach by AFM. In *Adhesion: Current Research and Applications*. Possart W, Ed. Weinheim: Wiley-VCH Verlag, 2006: 33–45.

[47] Derjaguin B V, Rabinovich Y I, Churaev N V. Measurement of forces of molecular attraction of crossed fibres as a function of width of air gap. *Nature* **265**(5594): 520–521 (1977)

[48] Derjaguin B V, Abrikossova I I. Direct measurements of molecular attraction of solids. *Journal of Physics and Chemistry of Solids* **5**(1–2): 1–10 (1958)

[49] Derjaguin B V, Muller V M, Toporov Yu P. Effect of contact deformations on the adhesion of particles. *Journal of Colloid and Interface Science* **53**(2): 314–326 (1975)

[50] Derjaguin B. Untersuchungen über die Reibung und Adhäsion. *Kolloid-Zeitschrift* **69**(2): 155–164 (1934)

[51] Tabor D. Surface forces and surface interactions. *Journal of Colloid and Interface Science* **58**(1): 2–13 (1977)

[52] Maugis D. Adhesion of spheres: The JKR-DMT transition using a Dugdale model. *Journal of Colloid and Interface Science* **150**(1): 243–269 (1992)

[53] Zhuravlev V A. On the question of theoretical justification of the Amontons—Coulomb law for friction of unlubricated surfaces. *Proc Inst Mech Eng Part J: J Eng Tribol* **221**(8): 893–898 (2007)

[54] Greenwood J B P, Williamson J A. Contact of nominally flat surfaces. *Proceedings of the Royal Society of London. Series A* **295**(1442): 300–319 (1966)

[55] Fuller K N G, Tabor D. The effect of surface roughness

on the adhesion of elastic solids. *Proceedings of the Royal Society of London. Series A* **345**(1642): 327–342 (1975)

[56] Marshall S J, Bayne S C, Baier R, Tomsia A P, Marshall G W. A review of adhesion science. *Dental Materials* **26**(2): e11–e16 (2010)

[57] Packham D E, Work of adhesion: contact angles and contact mechanics. *International Journal of Adhesion and Adhesives* **16**(2): 121–128 (1996)

[58] Awaja F, Gilbert M, Kelly G, Fox B, Pigram P J. Adhesion of polymers. *Progress in Polymer Science* **34**(9): 948–968 (2009)

[59] Hoda N, Kumar S, Parameters influencing diffusion dynamics of an adsorbed polymer chain. *Physical Review E* **79**(2): 020801 (2009)

[60] Lee L-H, Effect of surface energetics on polymer friction and wear. In *Advances in Polymer Friction and Wear*. Lee L-H, Ed. Boston: Springer US, 1974: 31–68.

[61] Chen N, Maeda N, Tirrell M, Israelachvili J. Adhesion and friction of polymer surfaces: The effect of chain ends. *Macromolecules* **38**(8): 3491–3503 (2005)

[62] Deruelle M, Leger M, Tirrell M. Adhesion at the solid-elastomer interface: Influence of the interfacial chains. *Macromolecules* **28**(22): 7419–7428 (2002)

[63] Mangipudi V, Tirrell M, Pocius A V. Direct measurement of the surface energy of corona-treated polyethylene using the surface forces apparatus. *Langmuir* **11**(1): 19–23 (1995)

[64] She H, Chaudhury M K. Estimation of adhesion hysteresis using rolling contact mechanics. *Langmuir* **16**(2): 622–625 (2000)

[65] Greenwood J A, Johnson K L, Choi S-H, Chaudhury M K. Investigation of adhesion hysteresis between rubber and glass using a pendulum. *Journal of Physics D* **42**(3): 35301 (2009)

[66] Zhang L, Zeng H, Liu Q. Probing molecular and surface interactions of comb-type polymer polystyrene-graft-poly(ethylene oxide) (PS-g-PEO) with an SFA. *Journal of Physical Chemistry C* **116**(33): 17554–17562 (2012)

[67] Deruelle M, Tirrell M, Marciano Y, Hervet H, Leger L. Adhesion energy between polymer networks and solid surfaces modified by polymer attachment. *Faraday Discussions* **98**: 55–65 (1994)

[68] Taylor D E, Strawhecker K E, Shanholtz E R, Sorescu D C,

Sausa R C. Investigations of the intermolecular forces between RDX and polyethylene by force–distance spectroscopy and molecular dynamics simulations. *Journal of Physical Chemistry A* **118**(27): 5083–5097 (2014)

[69] Ahn D, Shull K R. Effects of substrate modification on the interfacial adhesion of acrylic elastomers. *Langmuir* **14**(13): 3646–3654 (1998)

[70] Zhao B, Brittain W J. Polymer brushes: Surface-immobilized macromolecules. *Progress in Polymer Science* **25**(5): 677–710 (2000)

[71] Peng S,Bhushan B. Smart polymer brushes and their emerging applications. *RSC Advances* **2**(23): 8557–8578 (2012)

[72] Kovalev A, Tsukruk V. Polymer nanolayers. In *Encyclopedia of Tribology*. Wang Q J, Chung Y-W, Eds. Boston: Springer, 2013: 2602–2607.

[73] Luzinov I, Julthongpiput D, Bloom P D, Sheares V V, Tsukruk V V. Bilayer nanocomposite molecular coatings from elastomeric/rigid polymers: Fabrication, morphology, and micromechanical properties. *Macromolecular Symposia* **167**(1): 227–242 (2001)

[74] Luzinov I, Tsukruk V V. Ultrathin triblock copolymer films on tailored polymer brushes. *Macromolecules* **35**(15): 5963–5973 (2002)

[75] Iyer K S,Luzinov I. Surface morphology of mechanically heterogeneous ultrathin polymer films. *Langmuir* **19**(1): 118–124 (2003)

[76] Hofer R, Textor M, Spencer N D. Alkyl phosphate monolayers, self-assembled from aqueous solution onto metal oxide surfaces. *Langmuir* **17**(13): 4014–4020 (2001)

[77] Zwahlen M, Tosatti S, Textor M, Hähner G. Orientation in methyl- and hydroxyl-terminated self-assembled alkanephosphate monolayers on titanium oxide surfaces investigated with soft X-ray absorption. *Langmuir* **18**(10): 3957–3962 (2002)

[78] Grigor'ev A Y, Dubravin A M, Kovalev A V, Kovaleva I N, Komkov O Y, Myshkin N K. Measurement of contact adhesion and attraction between engineering surfaces. *Trenie i Iznos* **24**(4): 405–412 (2003)

[79] Kovalev A V, Kovaleva I N, Myshkin N K. Phenomenological model of adhesion contact. *Trenie i Iznos* **26**(6): 575–585 (2005)

Nikolai K. Myshkin. He received his M.S. degree in electromechanics (1971) and PhD degree in tribology in 1977 from the Institute for Problems in Mechanics in Moscow, Russia. He has moved to Metal-Polymer Research Institute of Belarus National Academy of Sciences (MPRI) in Gomel, Belarus, and has got DSc in tribology (1985) and professor in materials (1991). He elected a Full Member (Academician) of the Belarus National Academy of Sciences in 2009. He was Director of MPRI in 2002–2017. His current position is the Head of Tribology Department in MPRI. His research areas are contact mechanics, micro/nanotribology, surface phenomena in friction and lubrication, polymer tribology, wear monitoring, electrical contacts, etc.

Alexander Kovalev. He received his M.S. degree in physics from the Gomel State University, Gomel, Belarus in 1997. He has earned PhD degree in tribology and physics of solids in 2007 from Metal-Polymer Research Institute, Gomel, Belarus. His current position is Research Fellow at State Key Laboratory of Tribology at Tsinghua University, China. His research focuses on micro/nano-tribology, contact mechanics, interfacial phenomena, surface characterization, etc.

RESEARCH ARTICLE

Film forming behavior in thin film lubrication at high speeds

He LIANG, Dan GUO[*], **Jianbin LUO**[*]

State Key Laboratory of Tribology, Tsinghua University, Beijing 100086, China

Abstract: The film forming condition may transit into thin film lubrication (TFL) at high speeds when it is under severe starvation. Central film thicknesses and film thickness profiles are obtained via a technique of relative optical interference intensity. These profiles show a critical film thickness lower than which the absolute values of the film thickness gradient against speed or time decrease. It is possible to be in the thin film lubrication mode under such conditions. The high speed flow drives the lubricant molecules to rearrange in TFL and critical film thickness higher than 100 nm is achieved. The viscosity is one of the main factors controlling the decreasing rate and the critical film thickness. This paper is designed to investigate the thin film lubrication behavior at high speeds.

Keywords: thin film lubrication; thin EHL film; high speeds; starvation

1 Introduction

In a nanoscale the lubrication behavior may be determined by both physical characteristics of the lubricant and the interaction between lubricant molecules and solid surfaces. It is defined as thin film lubrication (TFL) [1–4], which is a transition between elastohydrodynamic lubrication (EHL) [5–7] and boundary lubrication (BL) [8, 9]. In TFL ordered layers are formed essentially by aligned molecules driven by shearing or flowing in a confined space and these layers determine the behavior of the lubrication as has been proven both theoretically and experimentally [1–4, 10, 11]. It results in higher effective viscosity as well as thicker film thickness in TFL compared with that of absorbed layers in BL as long as the shear rate is less than the critical value of approximately 10^6–10^8 s^{-1} for shear thinning in confined lubricants [12]. Furthermore the side leakage and fluidity are minimized compared with EHL. Some factors like an external electrical field that have the ability to change the orientation of molecules can also change the film thickness and friction characteristics in TFL [13].

Most of the researches on thin film lubrication have been conducted under very low speed, for instance 10 mm/s, in order to reach the necessary nanoscale. It is hypothesized that there can be thin film lubrication at high speeds as long as the two friction surfaces are close enough to form a nano gap of tens of nanometers. Such condition is normally one of severely starved lubrication. The published researches on starvation mainly focus on the declining flow and the starvation degree [14–16]. The relationship between the inlet replenishment and the central film thickness was studied [17, 18]. The inlet replenishment is mainly driven by surface tension as well as van del Waals force which might be important for an extremely thin film [19, 20]. The asymmetric film thickness distribution induced by the centrifugal effects must be considered for high speeds [16, 21]. The lubrication condition and the characteristics in TFL at high speeds still need to be investigated as the film thickness falls down to tens of nanometers.

In the current work, the study of thin film lubrication is extended to high speeds and the basic properties for thin film lubrication are proposed for these high-speed conditions. The influence of factors like the viscosity, speed, and oil supply is investigated.

---

* Corresponding authors: Dan GUO, E-mail: guodan26@tsinghua.edu.cn; Jianbin LUO, E-mail: luojb@tsinghua.edu.cn

Nomenclature

EHL	Elastohydrodynamic lubrication
TFL	Thin film lubrication
BL	Boundary Lubrication
t_0	Operating temperature (K)
η_0	Ambient viscosity (Pa·s)
u	Lubricant entrainment speed, $u = (u_1 + u_2)/2$
u_1, u_2	Surface velocities of disc and ball (m/s)
E'	Reduced modulus (Pa)
p_H	Maximum Herzian pressure (Pa)
b	Theoretical Hertz contact radius (m)
h	Lubricant film thickness (m)
h_c	Central film thickness (m)
h_{cff}	Central film thickness under fully flooded lubrication (m)
λ	The wavelength of the incident light
k	The reflective index of lubricant
n	The interference order
I, I_{max}, I_{min}	The light intensity, the maximum and minimum interference light intensity
$\bar{I}$	The relative interference light intensity ($\bar{I} = (2I - I_{max} - I_{min})/(I_{max} - I_{min})$)
$\bar{I}_0$	The relative light intensity of zero film thickness
n_d	The revolution of disc
t	The time for operating the test
r	The radius of the oil track on the disc
ψ, ψ_1, ψ_2	The decreasing gradient of film thickness against entrainment speed defined in Eq. (2)
λ_t	The decreasing gradient of film thickness against time defined in Eq. (4)

2 Experimental condition

All the tests were conducted at up to 30 m/s on a custom made high-speed ball-on-disc test rig whose properties and functions were first introduced in Ref. [16]. A highly polished ball was loaded normally on a disc coated with a chromium layer. The roughnesses of the ball and the disc were 5 nm and 3 nm, respectively. Compared to the tens of nanometers of the film thickness formed between the ball and the disc, the influence of the roughness could be ignored. The ball and the disc were driven by high-speed spindles and the rotating speeds were controlled individually. The oil was introduced through near the contact inlet employing an oil-jet system. All tests were carried out at pure rolling and at a constant load of 15 N such that the maximum Hertz pressure in the contact zone was approximately 431 MPa. The room temperature was a constant 25 °C. Table 1 shows the material

properties of the balls and discs used in the tests. The coated glass disc gives optical access to the contact so that the relative optical interference intensity (ROII) technique [2, 13] can be utilized to measure the film thickness. The following equation [22] was used to determine the film thickness in the contact zone:

$$h = \frac{\lambda}{4\pi k}\left[\left(n + \left|\sin\frac{n\pi}{2}\right|\right)\cdot\pi + \arccos(\bar{I})\cdot\cos n\pi - \arccos(\bar{I}_0)\right]$$

$$(1)$$

where λ, k, and n represent the wavelength of the incident light, reflective index of lubricant and interference order respectively. I, I_{max} and I_{min} are the light intensity, and the maximum and minimum interference light intensity, respectively, $\bar{I}$ is used as the relative interference light intensity ($\bar{I} = (2I - I_{max} - I_{min})/(I_{max} - I_{min})$) and $\bar{I}_0$ represents the relative light intensity of zero film thickness.

Table 1 Operating conditions for measurements.

Operating conditions	Load (N)	E' (GPa)	p_H (MPa)	b (μm)	t_0 (°C)
	15	117	431	128	25
Material properties	Material	Radius (mm)	Roughness (nm)		
	Ball	Steel	11.1125	5	
	Disc	Glass with Cr coating	45	3	

Three viscosities of polyalphaolefin (PAO) oil were used in the test and their physical properties measured by a viscometer (Anton Paar, Austria) are shown in Table 2.

Table 2 Lubricant properties (t_0 = 25 ℃).

	PAO2	PAO4	PAO8
η_0 (mPa·s)	6.96	29.59	86.55
ρ (kg/m³)	798.8	819.0	832.6

3   Results

3.1   The film forming under severe starvation at high speeds

Figure 1 shows the measured central film thickness under fully flooded lubrication and under starved lubrication at speeds up to 30 m/s on the dual logarithmic coordinate. Three kinds of oil with various viscosities were tested (shown in Table 2).
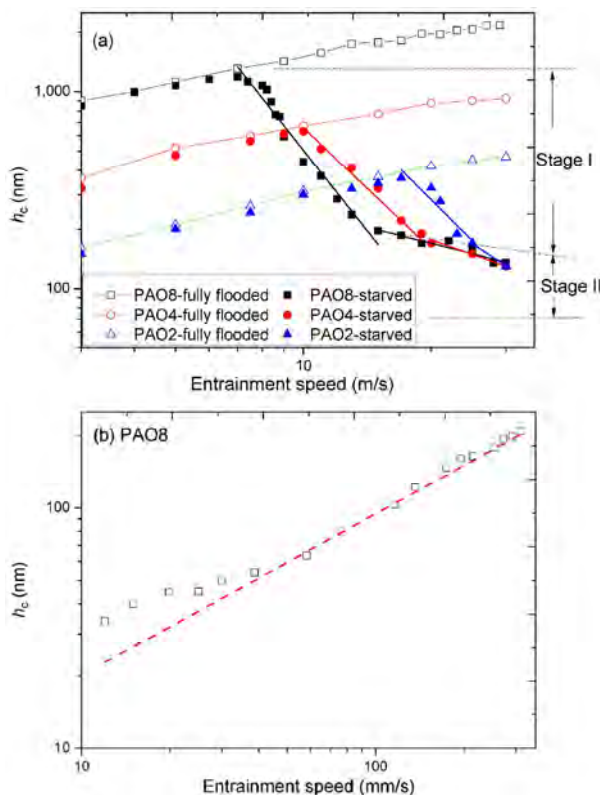
Fig. 1 Measurements of fully flooded and starved central film thickness for a range of speeds, pure rolling, p_H = 431 MPa, t_0 = 25 ℃, oil supply: 4.25 mL/s for fully flooded lubrication and 0.85 mL/s for starved lubrication.

For fully flooded lubrication, the central film thicknesses increase with speed and can achieve hundreds of nanometers. It is under elastohydrodynamic lubrication (EHL) as the typical horseshoe-shaped film thickness distribution can be obtained from the interference images shown in Ref. [16]. At very low speed, the central film thickness deviates from the traditional Hamrock-Dowson curve, which shows transition from EHL to TFL. The critical film thickness is approximately 50 nm at 30 mm/s for PAO8.

For starved lubrication, the central film thicknesses starts to decrease exponentially with speed beyond a critical speed and can be divided into two stages (shown in Fig. 1(a)). The second stage occurs when the film thickness reaches a low value beyond which the film thickness decreases more slowly against the entrainment speed. In order to compare the decreasing rate for the two stages, the decreasing gradient of central film thickness against entrainment speed is defined as

$$\psi = \mathrm{abs}\left[\log\left(\frac{h_1}{h_2}\right) \Big/ \log\left(\frac{u_1}{u_2}\right) \right] \tag{2}$$

The parameter ψ at two stages (named as ψ_1 and ψ_2) is found using curve fitting. A higher value of ψ represents a quicker decreasing rate. The shifting of the parameter ψ suggests that the lubrication condition might transition from EHL into thin film lubrication.

Figure 2 compares the trend of critical central film thickness and the parameter ψ as function of viscosity.
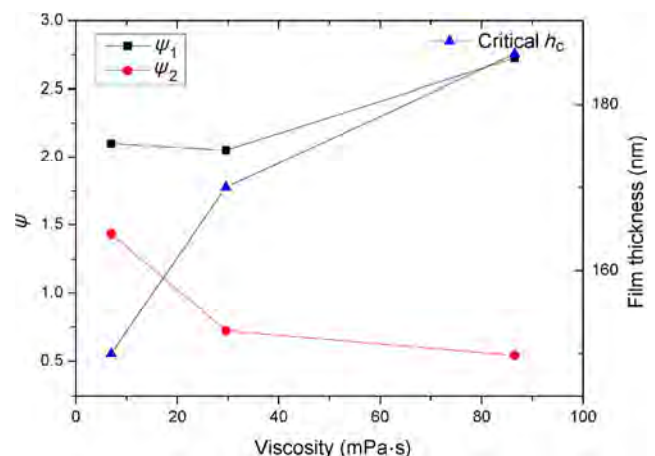

Fig. 2 Change of critical film thickness and the paramter ψ against viscosity for starved lubrication, pure rolling, p_H = 431 MPa, t_0 = 25 ℃, oil supply: 0.85 mL/s.

The critical film thickness shows a slight lowering, from 190 nm to 150 nm with decreasing viscosity. For one specific oil, the value of ψ_2 is smaller than that of ψ_1, which shows that the decreasing rate of film thickness against entrainment speed is slowed. Using PAO8 as an example, it can be seen from Fig. 2 that the value of ψ_2 is 0.54, one-fifth of the value of ψ_1. Furthermore, the changes of ψ_1 and ψ_2 show the opposite trend against increasing viscosity. The two stages might be influenced by different mechanisms. In stage I, the higher viscosity oil achieves a higher absolute value of ψ_1. The main factor should be the centrifugal effect [21]. The centrifugal force is a bulk force mainly determined by the mass and the rotating speed. The oil with higher viscosity gets a higher mass since the film thickness increases at a certain speed. This leads to a stronger centrifugal effect. The centrifugal force has the ability to weaken the oil replenishment and to accelerate the reduction of film thickness under starved lubrication as it can drive off the oil near the inlet zone and accelerate the side leakage. Therefore in stage I the change of film thickness is mainly determined by the lubricant bulk properties. On the contrary in stage II, the higher viscosity oil gets a lower value of ψ_2. This might be controlled by both the lubricant properties and the interfacial force between the lubricant molecules and the solid surface as the centrifugal effects are weakened for such thin film thickness.

Mid-plane film thickness profiles both parallel to and perpendicular to the entrainment speed direction are shown in Fig. 3. For the film thickness profiles parallel to the entrainment speed direction, the film shows to be flat in the center and the minimum film thickness appears near the outlet zone of the contact. These are important characteristics for EHL lubrication. In stage I of starvation, the film thickness decreases but still maintains the character of EHL, although the deviation of minimum film thickness and the central film thickness is getting smaller. In stage II of starvation, the reduction of film thickness near the outlet zone disappears. The whole profile shows to be flat. For the film thickness profiles perpendicular to the entrainment speed direction, the film thickness is convex in the center, and the film thickness at the edge of the contact zone decreases. As the film thickness is reduced, the film thickness profiles become flatter. It shows that
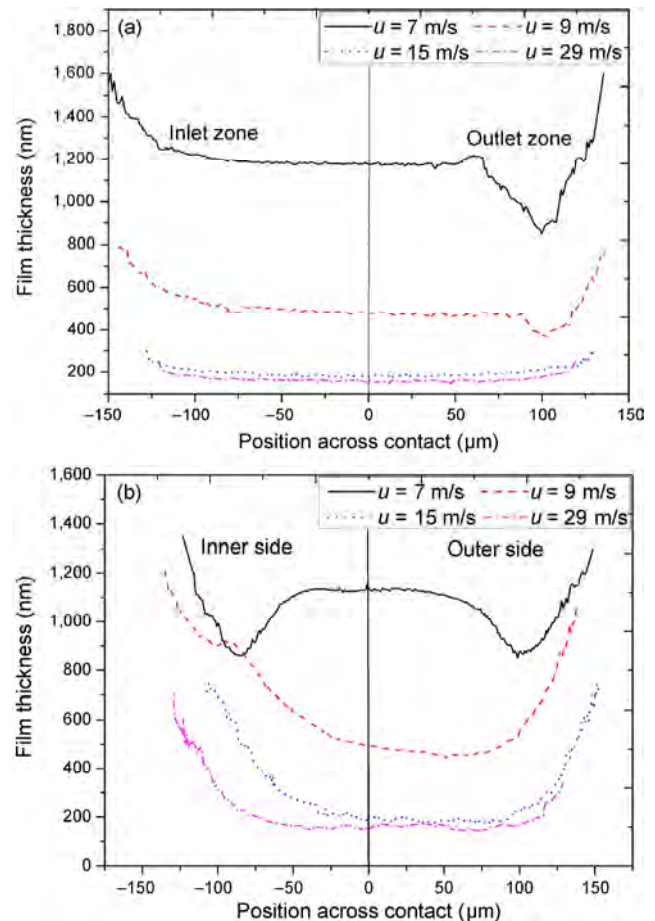

Fig. 3 Mid-plane film thickness profiles (a) parallel to and (b) perpendicular to the direction of entrainment speed under starved lubrication. The perpendicular axis is along the direction of centrifugal forces. Pure rolling, $p_H = 431$ MPa, $t_0 = 25$ °C, oil supply: 51 mL/min, PAO8.

the side leakage is weakened to an extent and the flow law may not fit this kind of condition.

At high speeds and under starved lubrication conditions the critical film thickness of approximately 170 nm is much higher than the typical transition film thickness of less than 100 nm at lower speeds, although it still shows the characteristics of thin film lubrication. Figure 4 shows the measured film thickness of various oil supplies under starved lubrication for PAO8. It can be seen that the starvation starts at lower entrainment speed for a lower oil supply. Furthermore, it shows two stages in the starvation region as the deviation between ψ_1 and ψ_2 still exists as shown in Fig. 5. The reduction of oil supply makes the critical film thickness of stage II slowly decrease. However, it does not change the opposite trend of ψ_1 and ψ_2
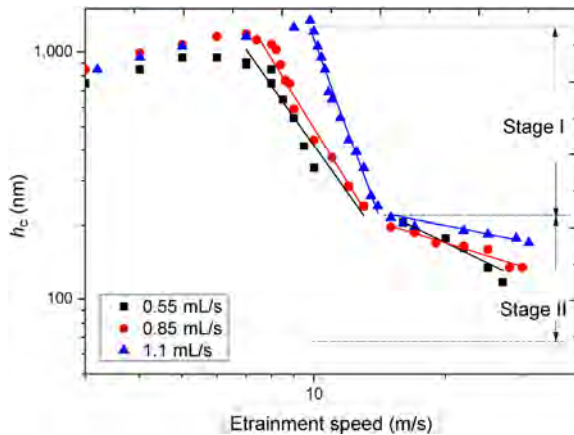
Fig. 4 Measurements of starved film thickness for three different oil supply rate, pure rolling, $p_H = 431$ MPa, $t_0 = 25$ °C, PAO8.

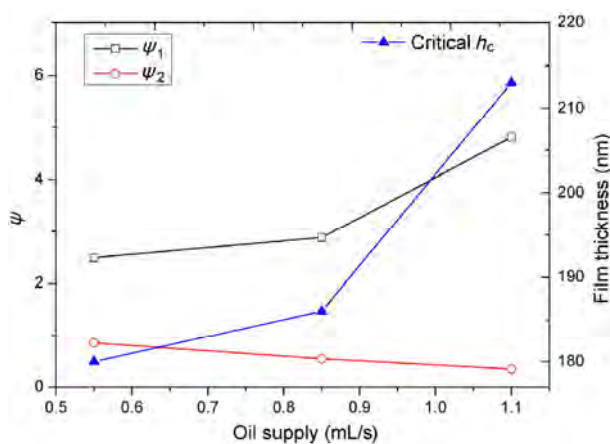**Fig. 5** Changes of the paramter ψ in stage I (ψ_1) and stage II (ψ_2) against oil supply rate, pure rolling, $p_H = 431$ MPa, $t_0 = 25$ °C, PAO8.

against entrainment speed, as the value of ψ_1 increases with oil supply while the value of ψ_2 decreases with oil supply. It shows that the properties in stage II, which are supposed to be in TFL, cannot be determined by oil supply.

3.2 The film forming behavior for limited oil supply at high speeds

In the above tests, the oil was supplied continuously for both fully flooded lubrication and starved lubrication. In this section, supply of oil was controlled and it was observed that film thickness gradually decreased against time from fully flooded lubrication to severe starvation after the oil supply was suspended as shown in Fig. 6 for oil of various viscosities at 30 m/s.

The film thickness is expected to decline all the time following the reduction of inlet replenishment. The fitting curves are drawn based on the following equation, first proposed by Chevalier et al. [18] and modified by Liang et al. [21] considering the replenishment and the centrifugal effects.

$$R(n_d) = \frac{1}{\sqrt[\gamma]{c_n n_d + 1 / r_0^{\gamma}}}$$
$$R(t) = \frac{1}{\sqrt[\gamma]{c_t t + 1 / r_0^{\gamma}}} \quad (3)$$

where $R = h_c / h_{cff}$, $c_n = (2\pi r / u)c_t$. n_d and t stand for the revolution of the disc and operating time. Parameter c_t represents the asymptotic film thickness decay rate and parameter γ physically means the side flow.

It appears that at a film thickness of approximately 100 nm, the declining rate of film thickness against time slows down. Therefore, the film thickness is subdivided into two stages as shown in Fig. 6. In stage I, the reduction of film thickness can be described by Eq. (3); while in stage II, the film thickness deviates from the fitting curves proposed by Eq. (3) and decreases exponentially with time. A uniform parameter λ_t is defined to describe this decreasing gradient of film thickness against time in stage II.

$$\lambda_t = \text{abs}\left[\log\left(\frac{h_1}{h_2}\right) / \log\left(\frac{t_1}{t_2}\right)\right] \quad (4)$$
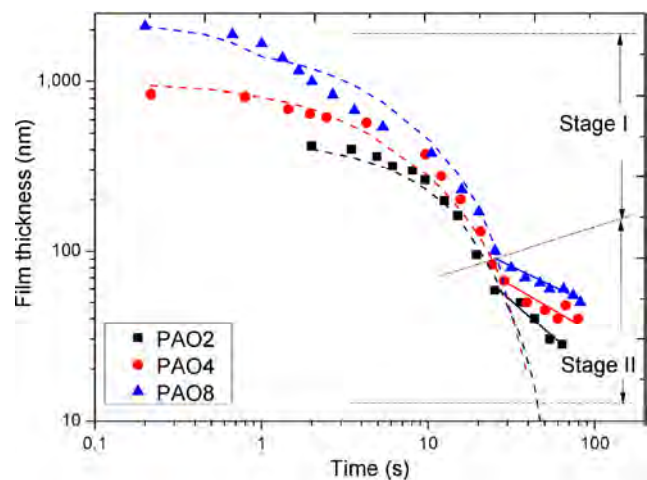

Fig. 6 Measurements of starved central film thickness against time after the oil supply is suspended for three different oil, pure rolling, $p_H = 431$ MPa, $t_0 = 25$ ℃.

It is noted that the oil with higher viscosity gets a higher value of critical film thickness and a smaller λ_t as shown in Fig. 7. The critical film thickness in this condition is less than 100 nm. The parameter λ_t increases with increasing viscosity, which is a trend similar to that of the parameter ψ_2 in the last section.

Figure 8 shows the film thickness declining with time after the oil is stopped for PAO2 with different speeds from 10 m/s to 30 m/s. The experimental results indicate that the film thicknesses diverge and get thicker from the general fluid theory when a critical film thickness is reached.
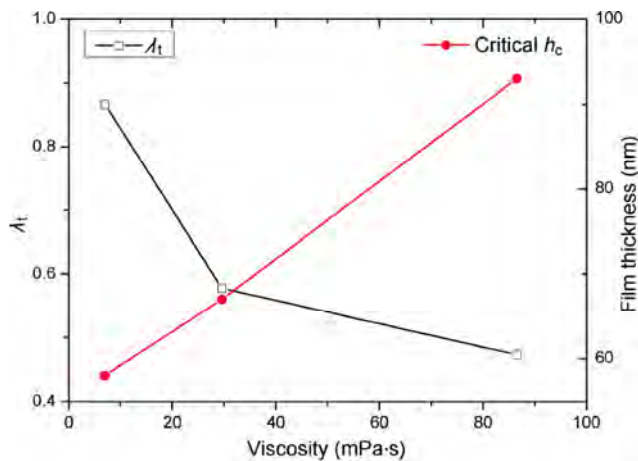
Fig. 7 Changes of critical filmthickness and the parameter λ_t against oil viscosity, pure rolling, $p_H = 431$ MPa, $t_0 = 25$ °C, PAO8.
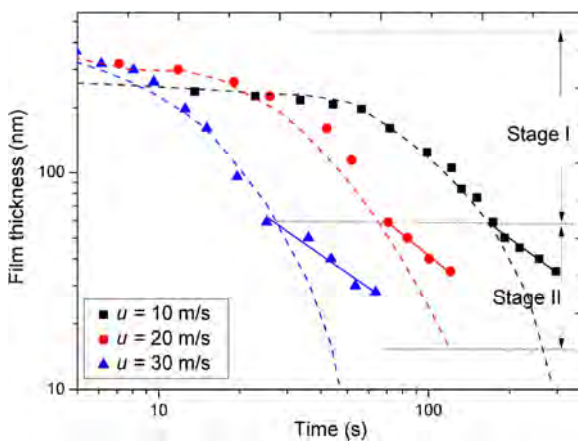

Fig. 8 Measurements of starved central film thickness against time after the oil supply is suspended for a range of speeds, pure rolling, $p_H = 431$ MPa, $t_0 = 25$ °C, PAO2.

4 Discussion

As a conclusion of the above tests, it is shown that the film thickness in starved lubrication can always be subdivided into two stages. In stage I, the film thickness decreases with entrainment speed or time following the starvation theory. The film thickness can be controlled by the hydrodynamic effects and the bulk properties of the oil. In stage II, the film thickness deviates from the classical theory, it decreases slower with entrainment speed or time. Both of these results indicate that the lubrication transits from EHL to thin film lubrication condition.

As a transition region between EHL and BL, both the dynamic film and the ordered lubricant film exist in the thin film lubrication condition. The ratio of ordered film layer to the whole film thickness rises largely enough as the film thickness decreases to nanoscale so that the influence of the ordered film layer can no longer be ignored.

It can be explained by the increasing effective viscosity mainly due to the formation of ordered molecule layers. The aligned layers are caused by both of the lubricant properties and the interfacial forces between the lubricant molecules and the solid surface.

There are two main forces affecting the lubricant molecules. One is the driven force, parallel to the entrainment speed. The shearing effects or high speed flow rate can drive the molecule to move in the same direction of flow. The other is vertical to the entrainment speed. It is the interfacial force between the lubricant molecules and solid surfaces that aligns the molecules to the solid surface. Under such confined actions, the lubricant molecules near the solid surface can be organized as solid-like which achieve a higher effective viscosity than the bulk viscosity.

The characteristics for thin film lubrication at high speeds are shown as follows.

It is possible that the high speed flow rate is the main driving force for aligning the molecules at high speeds. In EHL theory, the dynamic flow governs the characteristics of lubrication and film forming, so the adhesive film and the aligned molecular layer are relatively thin and can be ignored. In thin film lubrication, both the ordered layer and the dynamic

flow layer exist. The ordered degree of the ordered layer decreases gradually from the surface to the fluid film. The influence of the ordered layer is strong enough to change the properties of film forming. The critical film thickness for PAO8 oil at lower speeds under fully flooded lubrication is about 50 nm. The experimental results at pure rolling show that the high speed flowing rate might have the ability to drive molecules to arrange the direction and the ordered layer can influence the lubrication characteristics at a higher film thickness as the critical film thickness of TFL at high speeds is increased, for instance, 58 nm for PAO2 and 93 nm for PAO8 with a limited oil supply.

The critical film thickness and decreasing gradient are influenced by viscosity, which differs from that under EHL. According to general fluid theory, high viscosity may help prevent oil from replenishing, and then the film thickness decreasing gradient against speed or time would be enhanced. Besides, the high viscosity oil will undergo high centrifugal effects under the same speed, which also intensify the film thickness reduction under starved lubrication. However, in thin film lubrication, it shows the opposite trend. Oil with higher viscosity gets higher effective viscosity, decreases with speed or time more slowly on the contrary and keeps thicker film thickness. The flat film thickness profile suggests that the side leakage is weakened.

5 Conclusion

In this study, the measurement of decreasing film thickness under constant oil supply or constant speed is discussed. The results show the characteristics of thin film lubrication under severe starvation at high speeds when the film thickness is less than a critical film thickness. Driven by high speed flow, ordered layers are formed, which determine the lubrication behavior in thin film lubrication by increasing the effective viscosity. The study shows that in these conditions the critical film thickness is lower than that under lower speeds and in fully flooded condition. The viscosity influences the decreasing gradient of film thickness against entrainment speed and time.

Acknowledgments

References

[1] Luo J, Wen S. Mechanism and characters of thin film lubrication at nanometer scale. *Science in China, Series A-Mathematics, Physics, Astronomy* **39**(12): 1312–1322 (1996)

[2] Luo J, Wen S, Huang P. Thin film lubrication. Part I. Study on the transition between EHL and thin film lubrication using a relative optical interference intensity technique. *Wear* **194**(1): 107–115 (1996)

[3] Luo J, Liu S. The investigation of contact ratio in mixed lubrication. *Tribol Int* **39**(5): 409–416 (2006)

[4] Luo J, Huang P, Wen S, Li L K. Characteristics of liquid lubricant films at the nano-scale. *J Tribol* **121**(4): 872–878 (1999)

[5] Lugt P M, Morales-Espejel G E. A review of elasto-hydrodynamic lubrication theory. *Tribol Trans* **54**(3): 470–496 (2011)

[6] Spikes H A. Sixty years of EHL. *Lubr Sci* **18**(4): 265–291 (2006)

[7] Zhu D, Wang Q J. Elastohydrodynamic Lubrication: A gateway to interfacial mechanics—Review and prospect. *J Tribol* **133**(4): 041001 (2011)

[8] Hu Y, Ma T, Wang H. Energy dissipation in atomic-scale friction. *Friction* **1**(1): 24–40 (2013)

[9] Zhang J, Meng Y. Boundary lubrication by adsorption film. *Friction* **3**(2): 115–147 (2015)

[10] Hu Y Z, Granick S. Microscopic study of thin film lubrication and its contributions to macroscopic tribology. *Tribol Lett* **5**(1): 81–88 (1998)

[11] Zhang S, Liu Y, Luo J. In situ observation of the molecular ordering in the lubricating point contact area. *J Appl Phys* **116**(1): 014302 (2014)

[12] Itoh S, Ishii K, Fukuzawa K, Zhang H. Shear Thinning of nanometer-thick liquid lubricant films measured at high shear rates. *Tribol Lett* **53**(3): 555–567 (2014)

[13] Luo J, Shen M, Wen S. Tribological properties of nanoliquid film under an external electric field. *J Appl Phys* **96**(11): 6733–6738 (2004)

[14] Cann P M E, Damiens B, Lubrecht A A. The transition between fully flooded and starved regimes in EHL. *Tribol Int* **37**(10): 859–864 (2004)

[15] Liu J, Wen S. Fully flooded, starved and parched lubrication at a point contact system. *Wear* **159**(1): 135–140 (1992)

[16] Liang H, Guo D, Luo J. Experimental investigation of lubrication film starvation of polyalphaolefin oil at high speeds. *Tribol Lett* **56**(3): 491–500 (2014)

[17] Damiens B, Venner C H, Cann P M E, Lubrecht A A. Starved lubrication of elliptical EHD contacts. *J Tribol* **126**(1): 105–111 (2004)

[18] Chevalier F, Cann P, Colin F, Dalmaz G, Lubrecht A. Film thickness in starved EHL point contacts. *J Tribol* **120**(1): 126–133 (1998)

[19] Guangteng G, Spikes H. The role of surface tension and disjoining pressure in starved and parched lubrication. *Proc Inst Mech Eng Part J: J Eng Tribol* **210**(2): 113–124 (1996)

[20] Jacod B, Pubilier F, Cann P, Lubrecht A. An analysis of track replenishment mechanisms in the starved regime. *Tribology Series* **36**: 483–492 (1999)

[21] Liang H, Guo D, Ma L, Luo J. Experimental investigation of centrifugal effects on lubricant replenishment in the starved regime at high speeds. *Tribol Lett* **59**(1): 1–9 (2015)

[22] Ma L, Zhang C. Discussion on the technique of relative optical interference intensity for the measurement of lubricant film thickness. *Tribol Lett* **36**(3): 239–245 (2009)

Jianbin LUO. He received his BEng degree from Northeastern University in 1982, and got his MEng degree from Xi'an University of Architecture and Technology in 1988. In 1994, he received his PhD degree from Tsinghua University and then joined the faculty of Tsinghua University. Prof. Jianbin Luo is an academician of the Chinese Academy of Sciences and a Yangtze River Scholar Distinguished Professor of Tsinghua University, Beijing, China. He was awarded the STLE International Award (2013), the Chinese National Technology Progress Prize (2008), the Chinese National Natural Science Prize (2001), and the Chinese National Invention Prize (1996). Prof. Luo has been engaged in the research of thin film lubrication and tribology in nanomanufacturing. He was invited as a keynote or plenary speaker for 20 times on the international conferences.

Dan GUO. She received the M.S. degree in engineering mechanics in 1995 from Xi'an Jiaotong University and Ph.D. degree in engineering mechanics in 1999 from Tsinghua University. She joined the State Key Laboratory of Tribology at Tsinghua University from 1999. Her current position is a professor and the deputy director of the laboratory. Her research areas cover the mechanism of interaction among nanoparticles, lubrication and failure mechanism under rigorous conditions, and movement behavior of confined-microfluidic.

He LIANG. She received her Ph.D. degree in 2015 from State Key Lab of Tribology, Tsinghua University, China. The same year she joined the Tribology Group at Imperial College London as a postdoc. Her research areas involve the mechanism of lubrication behaviour in lubricated contacts and in rolling element bearings at high speeds.

Isosteric design of friction-reduction and anti-wear lubricant additives with less sulfur content

Xinlei GAO[1,*], **Denghui LIU**[1], **Ze SONG**[1], **Kang DAI**[2]

[1] *School of Chemical and Environmental Engineering, Wuhan Polytechnic University, Wuhan 430023, China*

[2] *College of Pharmacy, South-Central University for Nationalities, Wuhan 430074, China*

Abstract: To reduce harmful sulfur content in lubricant additives, making use of isosterism has been shown to be an effective strategy. When thiobenzothiazole compounds were used as templates, the exchange of sulfur atoms in the thiazole ring with oxygen atoms and NH groups produced twelve isosteres. Similarly, 2-benzothiazole-S-carboxylic acid esters were used as template molecules to produce six isosteres. About 30% of the isosteres exhibited a satisfactory deviation of ±5% relative to the template, ignoring the specific changes in the base oils, the differences in molecular structure, and the friction or wear properties. The template molecules and isosteres in triisodecyl trimellitate exhibited better tribological properties than in trimethylolpropane trioleate or bis(2-ethylhexyl) adipate. Comparative molecular field analysis (CoMFA)- and comparative molecular similarity index analysis (CoMSIA)-quantitative structure tribo-ability relationship (QSTR) models were employed to study the correlation of molecular structures between the base oils and additives. The models indicate that the higher the structural similarities of the base oils and additives are, the more synergetic the molecular force fields of the lubricating system are; the molecular force fields creating synergistic effects will improve tribological performance.

Keywords: isosterism; friction-reduction and anti-wear lubricant additives; comparative molecular field analysis; comparative molecular similarity index analysis; quantitative structure tribo-ability relationship; less sulfur content

1 Introduction

The largest user of lubricant additives is the automotive industry. Over the past ten years, the development of lubricant additives has been affected by new laws and regulations. In order to control pollution, European and American countries have enacted stringent new emission standards that require an extended life for exhaust systems, improved fuel efficiency, and the use of less toxic biodegradable lubricants with acceptable environmental compatibility. The new specified limits of sulfated ash, phosphorous, and sulfur in lubricants are lower than previously defined ones [1]. These limits now require adjusting and improving engine oil formulations, the gradual introduction of ash-less antioxidants, anti-wear additives, and enhancements in dispersant and viscosity indices. To effectively reduce environmental pollution, lubricants having high-performance friction-reduction and anti-wear additives with less sulfur content need to replace the widely used additives having high sulfur content.

Sulfur, which plays an important role, is difficult to replace in the development of new lubricants with adequate friction reduction and anti-wear properties [2–9]. A traditional research and development approach would have an enormous workload and high costs. There have been few successful systematic theoretical and experimental reports on new lubricant additives that employ little or no sulfur. Hence, to meet the environmental protection requirements, a new

---

* Corresponding author: Xinlei GAO, E-mail: gaoxl0131@163.com

isosterism concept is introduced in this paper [10–12] for the design of new lubricant additives with less sulfur, which is based on selected template molecules.

The concept of chemical isosteres [13, 14] was first discussed by Langmuir in 1919, who revealed that atoms, functional groups, and molecules with similar molecular electronic structures exhibit similar physical and chemical properties [15]. These similarities often occur for atoms that are in the same column in the periodic table—the column with atoms having the same number of outer electrons or having similar sizes and properties or behaviors. In 1925, Grimm formulated the hydride displacement law [16]. In 1932, Erlenmeyer proposed a broadening of the term isosterism by defining isosteres as elements, molecules, or ions that have the same number of valence electrons [16]. In 1951, Friedman introduced the term bioisosterism for the similar or antagonistic biological activity of structurally related compounds [13, 14, 16]. In 1979, Thornber broadened the term bioisosteres to include subunits, groups, or molecules that possess physicochemical properties with similar biological effects [13, 14, 16]. In structure optimization research, bioisosterism is actively used for structural modification of drugs to replace isosteres with one another in the variable part of the basic molecular structure. The isosteres refer to atoms, ions, and molecules with the same number of outer electrons, as well as groups with similar steric and electronic configurations. Isosteres have groups or substituents with similar physical and chemical properties, resulting in similar, related, or opposing biological activities.

Burger classified and subdivided bioisosteres into two broad categories: classic and non-classic [17]. Atoms, molecular subunits, or functional groups of the same valence and ring equivalents are defined as classic bioisosteres. These include monovalent, divalent, or trivalent atoms or groups, tetra-substituted atoms, and ring equivalents. Atoms or functional groups of similar volumes, electronegativities, and stereochemical characteristics are non-classic bioisosteres. These include cyclic vs. non-cyclic, functional groups, and retro-isosterism. Bioisosteric replacement should be rigorously preceded by careful analyses of the following parameters: (a) size, volume, and electronic distribution of the atoms, or degree of hybridization,

polarizability, bonding angles, and inductive and mesomeric effects; (b) lipidic and aqueous solubility, such as log$P$ and pKa; (c) chemical reactivity of the functional groups or bioisosteric structural subunits; and (d) conformational factors. Classic and non-classic bioisosteres possess variable parts of the basic structure of a drug, which can be modified to improve therapeutic effects and to reduce side effects. There is no regularity in pharmacological activity—bioisosterism is used to design new drugs, and the biological activity can be increased, weakened, or have an antagonistic effect. Bioisosterism is a useful way to discover new analogs of therapeutic innovations that are commercially attractive.

In this paper, we discuss isosterism as a strategy for molecular modification with the aim of synthesizing a new series of congener compounds for use as friction-reduction and anti-wear lubricant additives. We seek ways to substitute for sulfur present in high performance additives, and which have similar structure and function. In preliminary trials, thiobenzothiazole compounds and 2-benzothiazole-S-carboxylic acid esters were used as template molecules because they exhibit relatively good friction-reduction and anti-wear performance when using as lubricant additives [18–24, 27, 29]. Isosterism is a strategy for the rational design of new additive molecules, and can be applied via the molecular modification of template molecules. Because the sulfur atom (S), the oxygen (O), and the NH are classic isosteres with the same divalent group, the O atoms and NH groups can be used to replace the S atoms. Hence, a preliminary partial substitution of S in the lubricant additives was performed to prepare isosteric molecules, and the tribological performances were characterized.

Previously, the authors of this paper studied the relationship between molecular structure and tribological properties of lubricant additives and/or base oils, developed the concept of a "quantitative structure tribo-ability relationship" (QSTR) [23–29], and built back propagation neural network (BPNN)-QSTR model [23–25], infrared vibration-based descriptor (EVA)-QSTR model [26], Bayesian regularization neural network (BRNN)-QSTR model [27], comparative molecular field analysis (CoMFA)-QSTR model, and

comparative molecular similarity index analysis (CoMSIA)-QSTR model [28, 29]. In this paper, using isoterism as a strategy of molecular modification, similar structural characteristics are now being searched for, in order to build a new series of congener compounds for new lubricant additives. This is an important step in the development of specific molecular designs from early theoretical work.

In addition, the correlation of the structural similarities and tribological performance of the lubricant additive and base oil is discussed. CoMFA and CoMSIA methodologies will be employed to illustrate the interaction between the lubricant additive and base oil in detail.

2　Materials and methods

2.1　Preparation of lubricant additives with less sulfur content [30]

2.1.1　Isosteres based on thiobenzothiazole

Using thiobenzothiazole compounds (Fig. 1) as template molecules, isosteric exchanges were performed between bivalent groups, exchanging the S in the thiazole ring with an O in the compound shown in Fig. 2 and a NH group as shown in Fig. 3. This overall exchange, which is illustrated in Fig. 4, is referred to as Scheme 1.
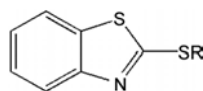
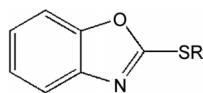**Fig. 1**　The structural formula of the compound.
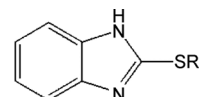

Fig. 2　The structural formula of the compound.

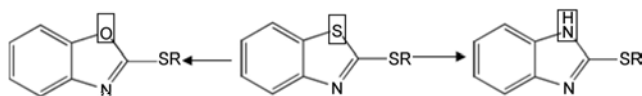**Fig. 3**　The structural formula of the compound.

Fig. 4　Scheme 1.

2.1.2　Preparation of thiobenzothiazole compounds and isosteres

The thiobenzothiazole compounds (Fig. 5) and twelve isosteres (Figs. 6 & 7) were synthesized based on the classic isoterism of bivalent groups.
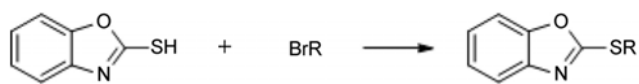

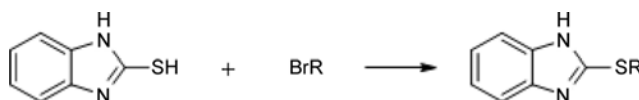**Fig. 5**　Scheme 2.

Fig. 6　Scheme 3.

Fig. 7　Scheme 4.

The template molecules and isosteres are shown in Table 1.

2.1.3　Isosteres based on 2-benzothiazole-S-carboxylic acid esters

As shown above, the replacement of S in the thiazole ring in Scheme 5 (Fig. 8) present in 2-benzothiazole-S-carboxylic acid esters shown in Fig. 9, with O was performed to synthesize 2-benzoxazole-S-carboxylic acid esters shown in Fig. 10.
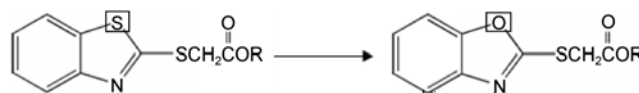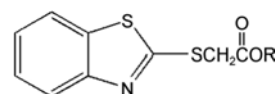

Fig. 8　Scheme 5.

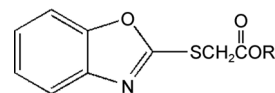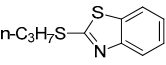**Fig. 9**　The structural formula of the compound.
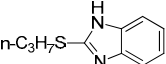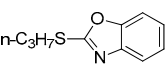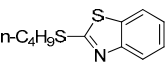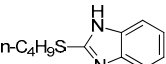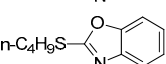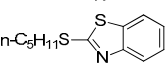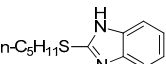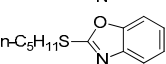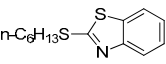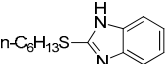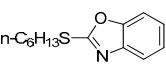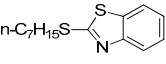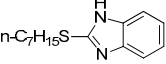
Fig. 10　The structural formula of the compound.

2.1.4　Preparation of 2-benzothiazole-S-carboxylic acid esters and isosteres

The synthesis route of 2-benzothiazole-S-carboxylic

Table 1 The tribological test results of the corresponding lubricant with thiobenzothiazole compounds or isosteres.

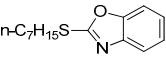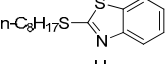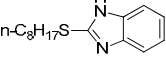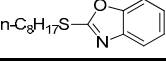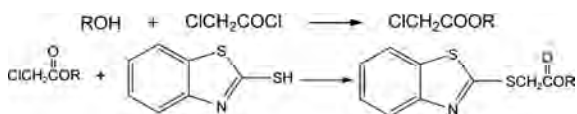|	Additive	Anti-wear in bis(2-ethylhexyl) adipate		Friction-reduction in bis(2-ethylhexyl) adipate		Anti-wear in triisodecyl trimellitate		Friction-reduction in triisodecyl trimellitate		Anti-wear in TMPTO		Friction-reduction in TMPTO	
Molecular property	Molecular structural formula	Width of the wear scar (mm)	Deviation (%)	Friction coefficient	Deviation (%)	Width of the wear scar (mm)	Deviation (%)	Friction coefficient	Deviation (%)	Width of the wear scar (mm)	Deviation (%)	Friction coefficient	Deviation (%)
Template	n-C$_3$H$_7$S– (benzothiazole, S)	0.801		0.1212		0.475		0.1124		0.855		0.1149	
Isostere	n-C$_3$H$_7$S– (benzimidazole, NH)	0.858	7.12	0.1239	2.23	0.618	30.11	0.1127	0.27	0.848	–0.82	0.1169	1.74
	n-C$_3$H$_7$S– (benzoxazole, O)	0.675	–15.73	0.1017	–16.09	0.478	0.63	0.1017	–9.52	0.763	–10.76	0.1084	–5.66
Template	n-C$_4$H$_9$S– (benzothiazole, S)	0.767		0.1202		0.515		0.1104		0.980		0.1055	
Isostere	n-C$_4$H$_9$S– (benzimidazole, NH)	0.840	9.52	0.1274	5.99	0.578	12.23	0.1022	–7.43	0.875	–10.71	0.1094	3.70
	n-C$_4$H$_9$S– (benzoxazole, O)	0.722	–5.87	0.1084	–9.82	0.512	–0.58	0.1084	–1.81	0.868	–11.43	0.1150	9.00
Template	n-C$_5$H$_{11}$S– (benzothiazole, S)	0.822		0.1229		0.568		0.1090		0.845		0.1150	
Isostere	n-C$_5$H$_{11}$S– (benzimidazole, NH)	0.817	–0.61	0.1178	–4.15	0.645	13.56	0.1043	–4.31	0.872	3.20	0.1114	–3.13
	n-C$_5$H$_{11}$S– (benzoxazole, O)	0.760	–7.54	0.1155	–6.02	0.511	–10.04	0.1161	6.51	0.953	12.78	0.1208	5.04
Template	n-C$_6$H$_{13}$S– (benzothiazole, S)	0.713		0.1160		0.550		0.1073		0.945		0.1122	
Isostere	n-C$_6$H$_{13}$S– (benzimidazole, NH)	0.737	3.37	0.1126	–2.93	0.623	13.27	0.1061	–1.12	0.845	–10.58	0.1110	–1.07
	n-C$_6$H$_{13}$S– (benzoxazole, O)	0.828	16.13	0.1079	–6.98	0.532	–3.27	0.1079	0.56	0.917	–2.96	0.1192	6.24
Template	n-C$_7$H$_{15}$S– (benzothiazole, S)	0.785		0.1227		0.515		0.1074		0.812		0.1139	
Isostere	n-C$_7$H$_{15}$S– (benzimidazole, NH)	0.762	–2.93	0.1188	–3.18	0.543	5.44	0.1063	–1.02	0.768	–5.42	0.1007	–11.59
	n-C$_7$H$_{15}$S– (benzoxazole, O)	0.785	0	0.1116	–9.05	0.603	17.09	0.1116	3.91	0.861	6.03	0.1149	0.88
Template	n-C$_8$H$_{17}$S– (benzothiazole, S)	0.785		0.1265		0.743		0.1163		0.753		0.1061	
Isostere	n-C$_8$H$_{17}$S– (benzimidazole, NH)	0.963	22.68	0.1300	2.77	0.585	–21.27	0.1028	–11.61	0.923	22.58	0.1138	7.26
	n-C$_8$H$_{17}$S– (benzoxazole, O)	0.802	2.17	0.1104	–12.73	0.503	–32.30	0.1104	–5.07	0.813	7.97	0.1179	11.12

acid esters is referred to as Scheme 6 and is given by Fig. 11.

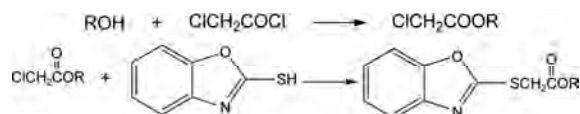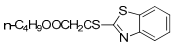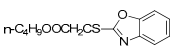Six isosteres were synthesized (Scheme 7 in Fig. 12), as shown in Table 2.

Fig. 11 Scheme 6.
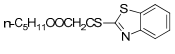

Fig. 12 Scheme 7.

Table 2 The tribological test results of the corresponding lubricant with 2-benzothiazole-S-carboxylic acid esters or isosteres.

Molecular property	Molecular structural formula	Anti-wear in bis(2-ethylhexyl) adipate		Friction-reduction in bis(2-ethylhexyl) adipate		Anti-wear in triisodecyl trimellitate		Friction-reduction in triisodecyl trimellitate		Anti-wear in TMPTO		Friction-reduction in TMPTO	
		Width of the wear scar (mm)	Deviation (%)	Friction coefficient	Deviation (%)	Width of the wear scar (mm)	Deviation (%)	Friction coefficient	Deviation (%)	Width of the wear scar (mm)	Deviation (%)	Friction coefficient	Deviation (%)
Template	n-C$_4$H$_9$OOCH$_2$CS– (S)	0.832		0.1230		0.425		0.0981		0.792		0.1098	
Isostere	n-C$_4$H$_9$OOCH$_2$CS– (O)	0.972	16.83	0.1333	8.37	0.472	11.06	0.0946	−3.57	0.862	8.84	0.1106	0.73
Template	n-C$_5$H$_{11}$OOCH$_2$CS– (S)	0.777		0.1205		0.572		0.1008		0.802		0.1080	
Isostere	n-C$_5$H$_{11}$OOCH$_2$CS– (O)	0.828	6.56	0.1205	0	0.475	−16.96	0.1057	4.86	0.952	18.70	0.1145	6.02
Template	n-C$_6$H$_{13}$OOCH$_2$CS– (S)	0.798		0.1186		0.517		0.1032		0.865		0.1114	
Isostere	n-C$_6$H$_{13}$OOCH$_2$CS– (O)	0.808	1.25	0.1193	0.59	0.470	−9.09	0.0994	−3.68	0.957	10.64	0.1147	2.96
Template	n-C$_7$H$_{15}$OOCH$_2$CS– (S)	0.980		0.1259		0.495		0.1026		0.993		0.1160	
Isostere	n-C$_7$H$_{15}$OOCH$_2$CS– (O)	0.825	−15.82	0.1203	−4.45	0.598	20.81	0.1076	4.87	0.947	−4.63	0.1158	−0.17
Template	n-C$_8$H$_{17}$OOCH$_2$CS– (S)	0.830		0.1170		0.483		0.1049		0.803		0.1068	
Isostere	n-C$_8$H$_{17}$OOCH$_2$CS– (O)	0.915	10.24	0.1260	7.69	0.495	2.48	0.1040	−0.86	0.812	1.12	0.1086	1.69
Template	n-C$_9$H$_{19}$OOCH$_2$CS– (S)	0.858		0.1226		0.462		0.1024		0.888		0.1134	
Isostere	n-C$_9$H$_{19}$OOCH$_2$CS– (O)	0.868	1.17	0.1254	2.28	0.568	22.94	0.1033	0.88	0.832	−6.31	0.1065	−6.08

2.2 Tribology tests

It is necessary to employ the synthetic ester as a lubricant base oil under extremely harsh conditions and to study the new lubricant additives for the synthetic ester. Therefore, trimethylolpropane trioleate (TMPTO), triisodecyl trimellitate, and bis(2-ethylhexyl) adipate were used as base oils. The molecular structural formulas of the base oils are shown in Fig. 13. Lubricants were formed when 1 wt.% of a template molecule or an isostere were separately dissolved in a base oil.

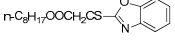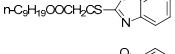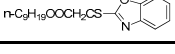A series of ball-disc contact friction tests were carried out using a microtribometer (UMT-3, CETR) to investigate the tribological characteristics of steel/steel rubbing pairs immersed in the corresponding lubricant. The experimental conditions were as follows: (1) a steel ball (52100, 4.45 mm in diameter) and the back of a NSK 51103 thrust ball bearing (steel 52100) as the sample; (2) a relatively low rotational velocity,
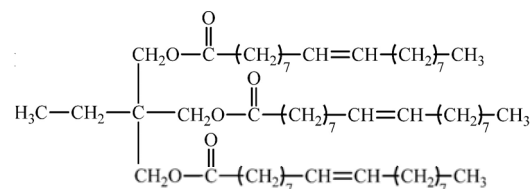
(a) TMPTO
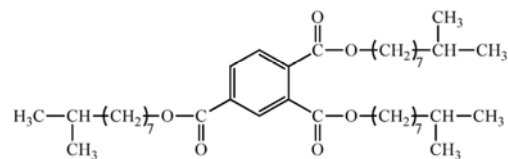
(b) Triisodecyl trimellitate
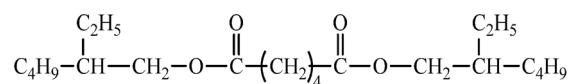
(c) Bis(2-ethylhexyl) adipate

Fig. 13 Molecular structural formula of base oil.

$v = 60.18$ mm/s; (3) a normal load, $L = 98$ N; and (4) time, $t = 60$ min [4, 6]. The diameter of the wear scale on the steel ball was measured using an optical microscope equipped with a scale. The friction coefficient was automatically recorded, and the average value of the friction coefficient was calculated by the system. Each of the lubricants was tested three times. The "diameter of wear scar" or the "friction coefficient" is the average value of the three tests.

In order to build a universal data set for future work, the tribological test method and conditions were kept in accordance with the previous tests mentioned in the published papers [16, 18, 20].

2.3 QSTR models with CoMFA and CoMSIA

2.3.1 *CoMFA-QSTR and CoMSIA-QSTR lubricant additive models for anti-wear*

Data for each anti-wear set of 18 organic compounds (lubricant additives, a column in Table 1) in the different base oils used along with their anti-wear data were included in the CoMFA or CoMSIA-QSTR models, respectively. To determine the anti-wear capability of each molecule, the wear scar widths were related through simple mathematical manipulation.

$$WS_{(98N)} = \frac{w \cdot MW \cdot Conc}{w_0} \tag{1}$$

In Eq. (1), WS represents the anti-wear scar scale, w is the measured size of the wear scar width in additive-containing lubricant, w_0 is the measured size of the wear scar width in pure base oil, MW is the molecular weight of the compound, and Conc is the percent concentration of the additive.

A total of 18 molecules were considered for this study, and CoMFA or CoMSIA models were developed for both the training ($n = 15$) and the test set molecules ($n = 3$). The test set was used to validate the developed models. The model was carried out in steric and electrostatic fields. The relationship between the structural parameters and the WS values was quantified by a partial least squares (PLS) algorithm. The regression coefficient R^2, the cross-validation coefficient $R^2_{(LOO)}$, and q^2 were also calculated [3–6, 22]. q^2 was computed according to the formula:

$$q^2 = 1 - \frac{\sum_i (\text{pred}_i - \text{obs}_i)^2}{\sum_i (\text{obs}_i - \overline{\text{obs}})^2} \tag{2}$$

2.3.2 *CoMFA-QSTR and CoMSIA-QSTR lubricant additive models for friction-reduction*

CoMFA and CoMSIA analysis for friction-reduction were carried out on each friction-reduction set of 18 organic compounds (lubricant additives, a column in Table 1) in the different base oils, respectively.

To determine the friction-reduction performance of each molecule, the friction coefficients were related through simple mathematical manipulation.

$$FS_{(98N)} = \frac{f \cdot MW \cdot Conc}{f_0} \tag{3}$$

In Eq. (3), FS represents the friction-reduction scale, f is the friction coefficient in the modified lubricant, f_0 is the friction coefficient in pure base oil, MW is the molecular weight of the compound, and Conc is the percent concentration of the additive.

The detailed steps of building the model were similar to the CoMFA-QSTR and CoMSIA-QSTR anti-wear models.

3 Results and discussion

3.1 Similarity assessment of isosteres

The tribology test results of the lubricants formed using the template molecules and their isosteres are shown in Tables 1 and 2 and also in Figs. 14–25. Changes in
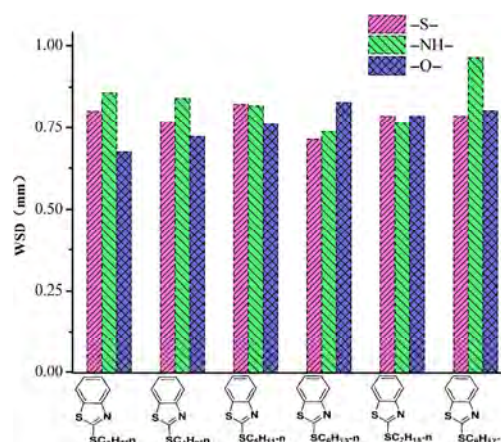
Fig. 14 The wear scar width of each steel ball when lubricating with thiobenzothiazole compounds and their isosteres in bis(2-ethylhexyl) adipate.
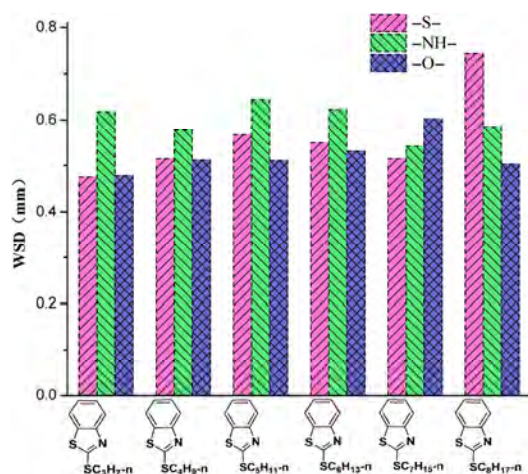
Fig. 15 The wear scar width of each steel ball when lubricating with thiobenzothiazole compounds and their isosteres in triisodecyl trimellitate.
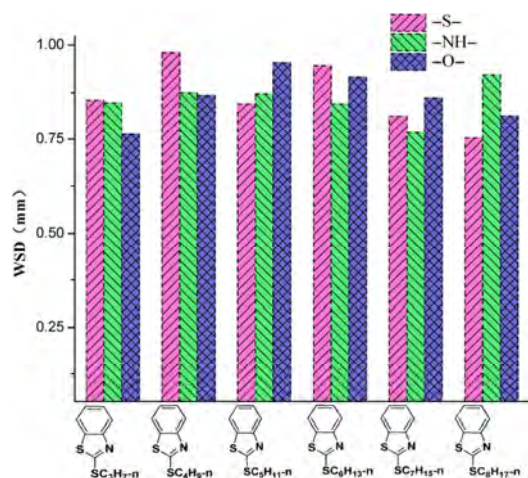
Fig. 16 The wear scar width of each steel ball when lubricating with thiobenzothiazole compounds and their isosteres in TMPTO.
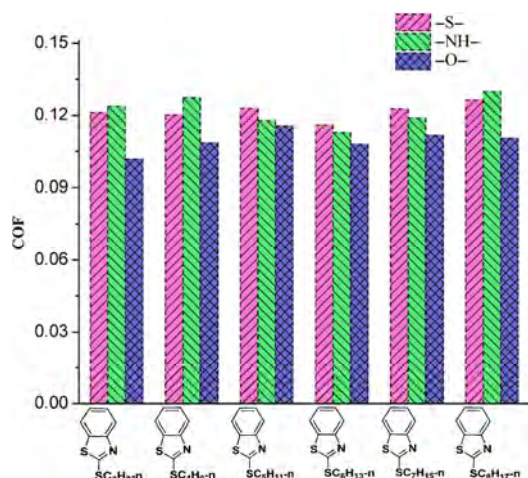
Fig. 17 The friction coefficient when lubricating with thiobenzothiazole compounds and their isosteres in bis(2-ethylhexyl) adipate.
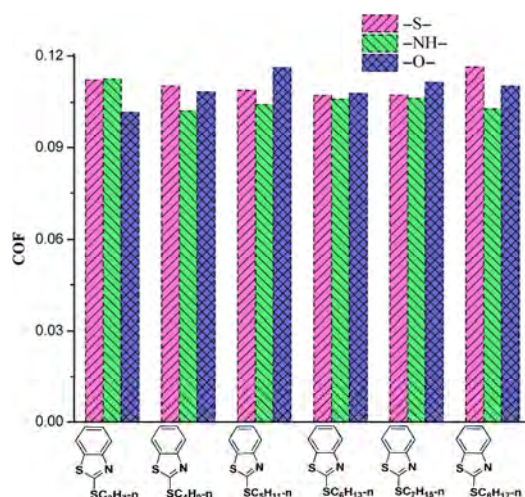
Fig. 18 The friction coefficient when lubricating with thiobenzothiazole compounds and their isosteres in triisodecyl trimellitate.
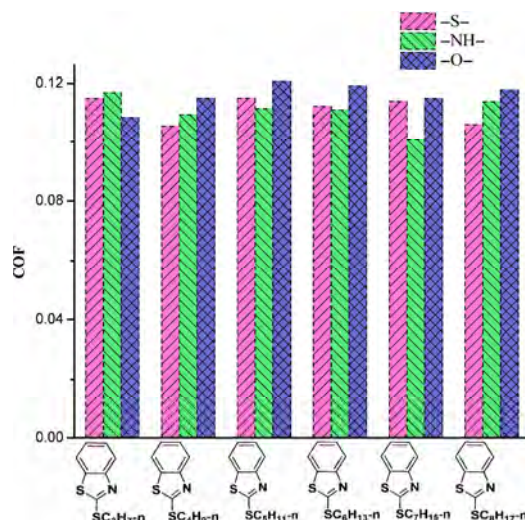
Fig. 19 The friction coefficient when lubricating with thiobenzothiazole compounds and their isosteres in TMPTO.

the tribological properties between the individual isosteres and the template molecule were calculated. A deviation refers to the difference between the actual data and the target values, and is given by

$$\text{Deviation} = \frac{X - A}{A} \qquad (4)$$

where A is the target value, and X is actual data.

3.2 Similarity assessment of isosteres based on thiobenzothiazole

There were six template molecules and twelve isosteres. Changes in the tribology between individual isosteres and their template molecules based on
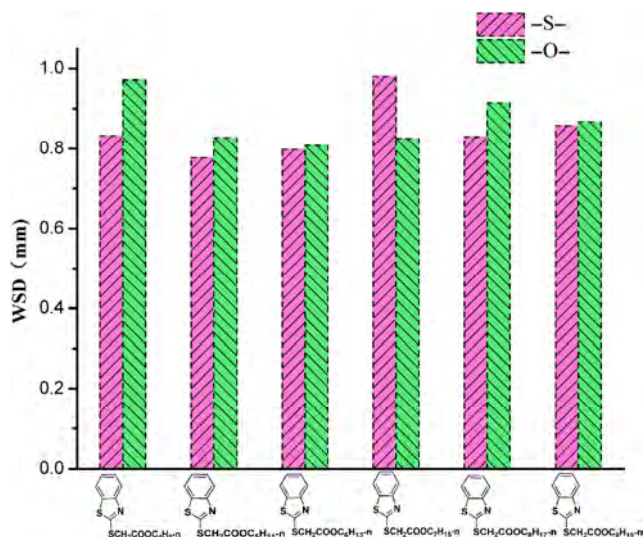
Fig. 20 The wear scar width of each steel ball when lubricating with 2-benzothiazole-S-carboxylic acid esters and their isosteres in bis(2-ethylhexyl) adipate.

Fig. 22 The wear scar width of each steel ball when lubricating with 2-benzothiazole-S-carboxylic acid esters and their isosteres in TMPTO.

Fig. 21 The wear scar width of each steel ball when lubricating with 2-benzothiazole-S-carboxylic acid esters and their isosteres in triisodecyl trimellitate.
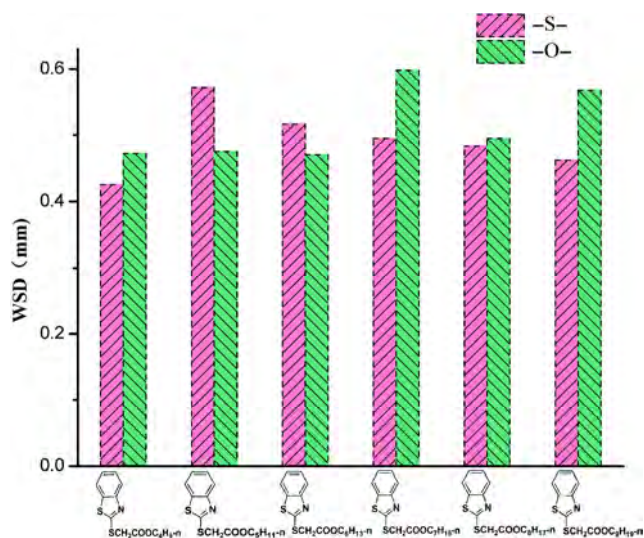
Fig. 23 The friction coefficient when lubricating with 2-benzothiazole-S-carboxylic acid esters and their isosteres in bis(2-ethylhexyl) adipate.

thiobenzothiazole compounds are shown in Table 3.

3.2.1 Anti-wear performance

Anti-wear performance of the lubricants formed with thiobenzothiazole compounds and their isosteres are shown in Table 1 and Figs. 14–16. Ignoring the specific changes in the base oils and the differences in molecular structure, there were 36 groups of isosteres for the anti-wear experiments. The results of the similarity assessment concerning isostere anti-wear
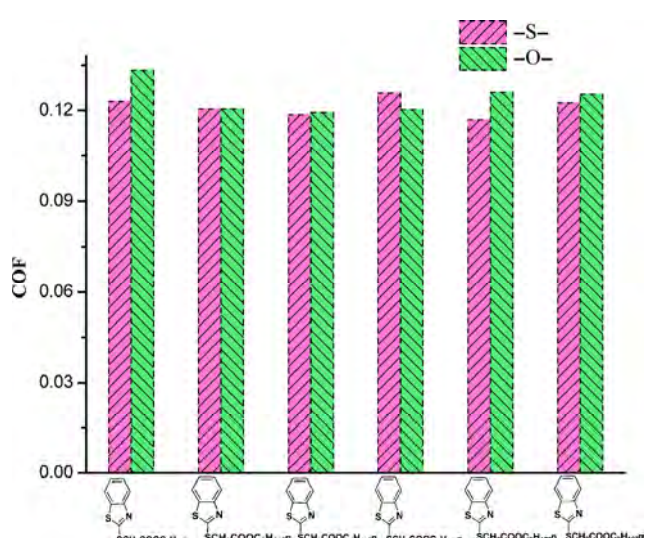
performance revealed that: (1) within a ±1% deviation, there are five compounds (13.89% of the isosteres); (2) within a ±5% deviation, there are 11 compounds (30.56% of the isosteres); (3) within a ±10% deviation, there are 19 compounds (52.78% of the isosteres); (4) there are eight compounds with absolute values of deviation greater than 15% (22.22% of the isosteres); finally (5) there are 18 compounds (50.00% of the isosteres), with an anti-wear performance that are consistent with or better than that of the template molecules.

Table 3 Similarity assessment of isosteres based on thiobenzothiazole compounds.

Deviation (%)	Anti-wear		Friction-reduction		Anti-wear or friction-reduction	
	Number of isosteres	Proportion (%)	Number of isosteres	Proportion (%)	Number of isosteres	Proportion (%)
±1	5	13.89	3	8.33	8	11.11
±5	11	30.56	17	47.22	28	38.89
±10	19	52.78	31	86.11	50	69.44
±15	28	77.78	35	97.22	63	87.50
>15 (the absolute value of deviation)	8	22.22	1	2.78	9	12.50
Isosteres (property consistent with or better than the templates)	18	50.00	21	58.33	39	54.17
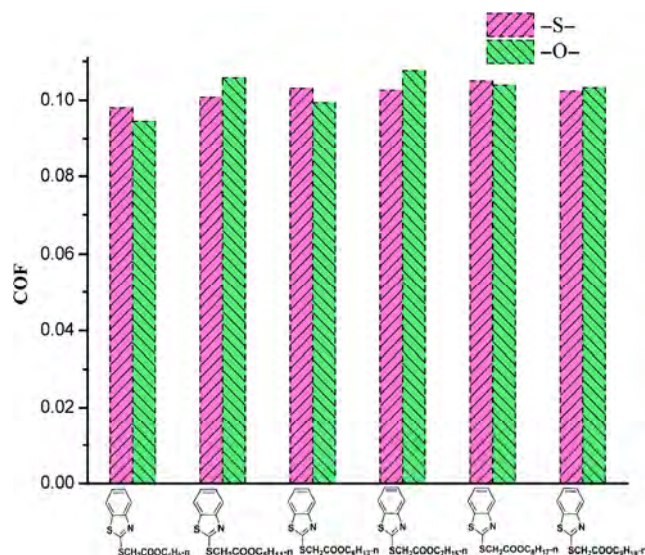
Fig. 24 The friction coefficient when lubricating with 2-benzothiazole-S-carboxylic acid esters and their isosteres in triisodecyl trimellitate.
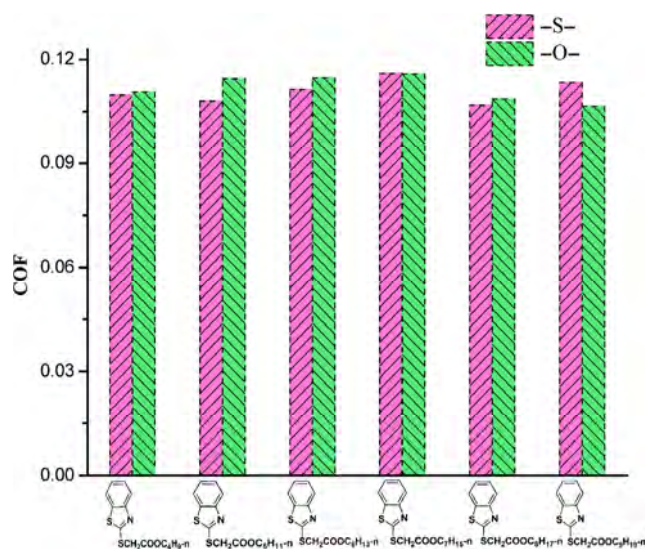
Fig. 25 The friction coefficient when lubricating with 2-benzothiazole-S-carboxylic acid esters and their isosteres in TMPTO.

Relative to the corresponding template molecule, three special isosteres appeared among the eight compounds with absolute values of deviation greater than 15% and with significantly improved anti-wear characteristics, as shown in Figs. 26(a)–(c).

(a) 32.30% improvement in anti-wear

(b) 21.27% improvement in anti-wear

(c) 15.73% improvement in anti-wear

Fig. 26 The structural formula of the compound.

To some extent, it can be said that the three isosteres were revealed via molecular modification. In contrast, among these eight compounds, some exhibited adverse anti-wear effects, as shown in Figs. 27(a)–(c).

(a) 30.11% reduction in anti-wear effect

(b) 22.68% reduction in anti-wear effect

(c) 22.58% reduction in anti-wear effect
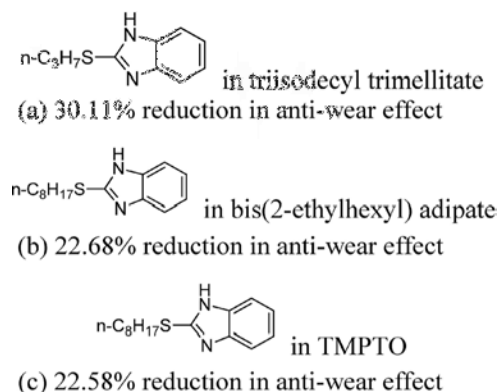
Fig. 27 The structural formula of the compound.

3.2.2 Friction-reduction performance

Friction-reduction performance of the lubricants formed with thiobenzothiazole compounds and their isosteres are shown in Table 1 and in Figs. 17–19. Ignoring the specific changes in the base oils and the differences in molecular structure, there were 36 groups of isosteres for the friction-reduction experiments. The results of the similarity assessment in regard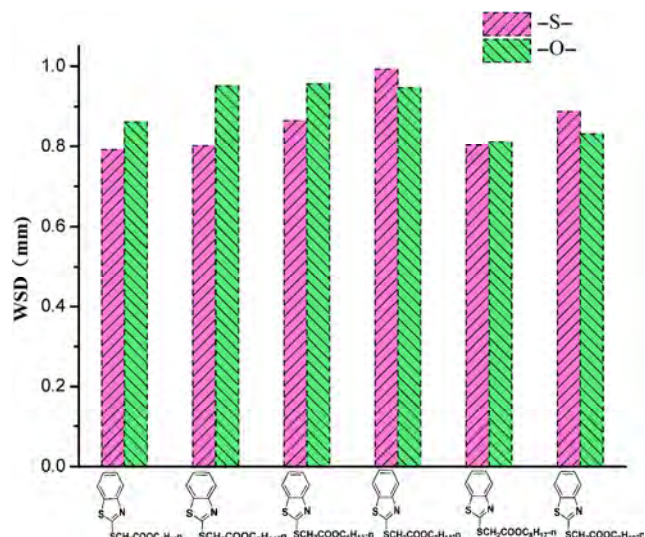s to isostere friction-reduction performance indicate that: (1) within a ±1% deviation, there are three compounds (8.33% of the isosteres); (2) within a ±5% deviation, there are 17 compounds (47.22% of the isosteres); (3) within a ±10% deviation, there are 31 compounds (86.11% of the isosteres); (4) there is only one compound with an absolute value of deviation greater than 15% (2.78% of the isosteres); finally (5) there are 21 compounds (58.33% of the isosteres) with a friction-reduction performance that are consistent with or better than that of the template molecules.

Relative to the corresponding template molecule, some isosteres had improved friction-reduction effects, as shown in Figs. 28(a)−(d).

(a) 16.09% improvement in friction reduction

(b) 12.73% improvement in friction reduction

(c) 11.61% improvement in friction reduction

(d) 11.59% improvement in friction reduction
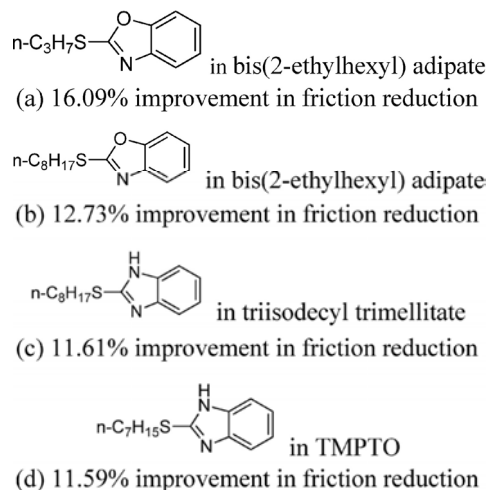
Fig. 28 The structural formula of the compound.

In contrast, the friction-reduction performance of the Fig. 29 isostere in TMPTO decreased by 11.12% relative to the corresponding template molecule in the same base oil.

Except for the Fig. 29 isostere, isosteres with absolute values of deviation greater than 10% exhibited much better friction-reduction than that of the template molecule in the corresponding base oil.
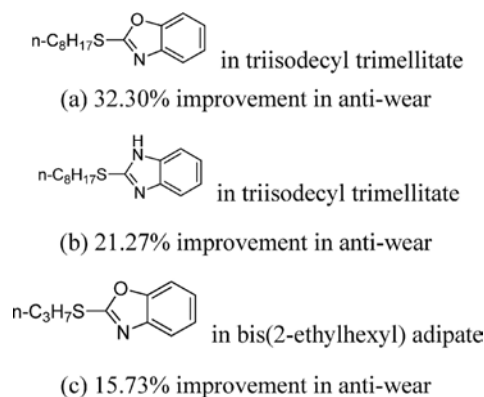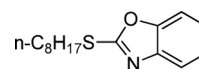

Fig. 29 The structural formula of the compound.

3.2.3 Tribological performance

Tribological performance of the lubricants formed with thiobenzothiazole compounds and their isosteres are shown in Table 1 and in Figs. 14–19. Ignoring the specific changes in the base oils, the differences in molecular structure, and friction or wear properties, there were 72 groups of isosteres in the tribology experiments. For the 72 groups of isosteres (ignoring the specific changes in the base oils, the differences in molecular structure, and without distinguishing specific tribological properties), in the similarity assessment of the tribological performance, the results indicate that: (1) within a ±1% deviation, there are eight groups (11.11% of the experiments); (2) within a ±5% deviation, there are 28 groups (38.89% of the experiments); (3) within a ±10% deviation, there are 50 groups (69.44% of the experiments); (4) there are nine groups with the absolute values of deviation greater than 15% (12.50% of the experiments); and (5) there are 39 experiment groups (54.17% of the experiments) with a friction-reduction or anti-wear performance that are consistent with or better than that of the template molecules.

In regards to both friction-reduction and anti-wear performance of the 36 isosteres, there are 12 isosteres (33.33% of all the isosteres) that exhibit consistent or better tribological performance than those of the template molecules.

Relative to the template molecule, both the friction-reduction and anti-wear performances of the isosteres significantly improved as shown in Figs. 30(a)−(e).

3.2.4 The best isosteres for the different lubricant base oils

In fact, there is no regularity in tribological performance; isosterism is employed to design new lubricant additives, and the tribo-ability can be increased, weakened, or yield an adverse effect. The best isosteres were chosen for the different lubricant base oils.

In bis(2-ethylhexyl) adipate, the Fig. 31 isostere is the best isostere additive. In tests, the width of the wear scar was 0.675 mm and the friction coefficient was 0.1017. In triisodecyl trimellitate, the same isostere

(a) 15.73% improved anti-wear effect and 16.09% improved friction-reduction effect

(b) 21.27% improved anti-wear effect and 11.61% improved friction-reduction effect

(c) 32.30% improved anti-wear effect and 5.07% improved friction-reduction effect

(d) 10.76% improved anti-wear effect and 5.66% improved friction-reduction effect

(e) 5.42% improved anti-wear effect and 11.59% improved friction-reduction effect

Fig. 30 The structural formula of the compound.

in Fig. 31 was found to be the best one. The results showed that the width of the wear scale was 0.478 mm and that the friction coefficient was 0.1017.
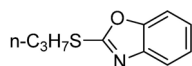
Fig. 31 The structural formula of the compound.

In TMPTO, the Figs. 31 and 32 isosteres both exhibited good tribological performances. With the former, the width of the wear scar was 0.763 mm and the friction coefficient was 0.1084. With the latter, the width of the wear scar was 0.768 mm and the friction coefficient was 0.1007.
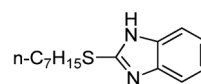
Fig. 32 The structural formula of the compound.

3.3 Similarity assessment of isosteres based on 2-benzothiazole-S-carboxylic acid esters

There were six template molecules and six isosteres. The deviations in tribological properties between the isosteres and the template molecules are shown in Table 4.

3.3.1 Anti-wear performance

Anti-wear performance of the lubricants formed with 2-benzothiazole-S-carboxylic acid esters and their isosteres are shown in Table 2 and Figs. 20–22. Ignoring the specific changes in the base oils and the differences in molecular structure, there were 18 groups of isosteres for the antiwear experiment.

The results of the similarity assessment in regards to isostere anti-wear performance showed that: (1) within a ±1% deviation, there is no compound (0% of the isosteres); (2) within a ±5% deviation, there are five compounds (27.78% of the isosteres); (3) within a ±10% deviation, there are nine compounds (50.00% of the isosteres); (4) there are six compounds with absolute values of deviation greater than 15% (33.33% of the isosteres); finally (5) there are 5 compounds (27.78% of the isosteres) with an anti-wear performance that was consistent with or better than that of the template molecules.

Relative to the corresponding template molecule, some special isosteres appeared among the six compounds with absolute values of deviation greater than 15% and with significantly changed anti-wear

Table 4 Similarity assessment of isosteres based on 2-benzothiazole-S-carboxylic acid esters.

Deviation (%)	Anti-wear		Friction-reduction		Anti-wear or friction-reduction	
	Number of isosteres	Proportion (%)	Number of isosteres	Proportion (%)	Number of isosteres	Proportion (%)
±1	0	0	6	33.33	6	16.67
±5	5	27.78	14	77.78	19	52.78
±10	9	50.00	18	100.00	27	75.00
±15	12	66.67	18	100.00	30	83.33
>15 (the absolute value of deviation)	6	33.33	0	0	6	16.67
Isosteres (property consistent with or better than the templates)	5	27.78	7	38.89	12	33.33

characteristics. These are shown in Figs. 33(a)–(e).

(a) 16.96% improvement in anti-wear effect

(b) 15.82% improvement in anti-wear effect

(c) 22.94% reduction in anti-wear effect

(d) 20.81% reduction in anti-wear effect

(e) 18.70% reduction in anti-wear effect
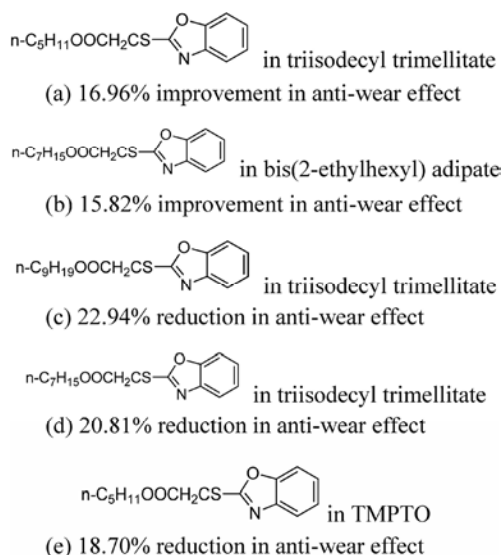
Fig. 33   The structural formula of the compound.

3.3.2   *Friction-reduction performance*

Friction-reduction performance of the lubricants formed with 2-benzothiazole-S-carboxylic acid esters and their isosteres are shown in Table 2 and Figs. 23–25. Ignoring the specific changes in the base oils, and the differences in molecular structure, there were 18 groups of isosteres for the friction-reduction experiments. The results of the similarity assessment in regards to isostere friction-reduction performance indicate that: (1) within a ±1% deviation, there are six compounds (33.33% of the isosteres); (2) within a ±5% deviation, there are 14 compounds (77.78% of the isosteres); (3) within a ±10% deviation, there are 18 compounds (100% of the isosteres); (4) there is no compound with an absolute value of deviation greater than 15% (0% of the isosteres); finally (5) there are seven compounds (38.89% of the isosteres) with a friction-reduction performance that was consistent with or better than that of the template molecules.

Relative to the corresponding template molecule, some isosteres had distinguishable changes in friction-reduction effects, as shown in Figs. 34(a)−(c).

3.3.3   *Tribological performance*

Tribological performance of the lubricants formed with 2-benzothiazole-S-carboxylic acid esters and their isosteres are shown in Table 2 and Figs. 20–25. Ignoring the specific changes in the base oils, the

(a) 6.08% improvement in friction-reduction effect

(b) 8.37% reduction in friction-reduction effect

(c) 7.69% reduction in friction-reduction effect
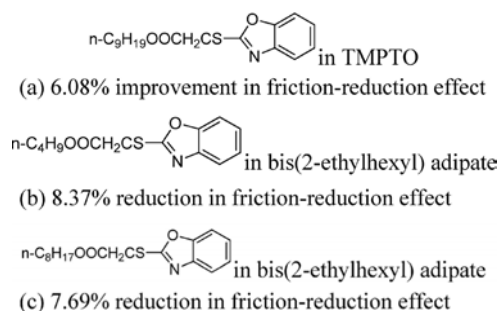
Fig. 34   The structural formula of the compound.

differences in molecular structures, and the friction or wear properties, there were 36 groups of experiments. For the 36 groups of isosteres (ignoring the difference of the specific experiments), in the similarity assessment of the tribological performance, the results are as follows: (1) within a ±1% of deviation, there are six groups (16.67% of the experiments); (2) within a ±5% deviation, there are 19 groups (52.78% of the experiments); (3) within a ±10% deviation, there are 27 groups (75.00% of the experiments); (4) there are six groups with absolute values of deviation greater than 15% (13.89% of the experiments); (5) there are 12 experiment groups (16.67% of the experiments) with a friction-reduction or anti-wear performance that was consistent with or better than that of the template molecules.

In regards to both friction-reduction and anti-wear performance, of the 18 isosteres in the tribological performance study, there are four isosteres (22.22% of all the isosteres), that exhibit consistent or better performance than that of the template molecules.

Relative to the template molecule, both friction-reduction and anti-wear performances largely improved as shown in Figs. 35(a)–(c).

(a) 15.82% increase in the anti-wear effect and a 4.45% increase in the friction-reduction effect.

(b) 9.09% increase in the anti-wear effect and a 3.68% increase in the friction-reduction effect.

(c) 6.31% increase in the anti-wear effect and a 6.08% increase in the friction-reduction effect.

Fig. 35   The structural formula of the compound.

3.3.4 *Best isosteres for the various lubricant base oils*

In bis(2-ethylhexyl) adipate, the Fig. 36 isostere is the optimal additive. The width of the wear scar was 0.808 mm and the friction coefficient was 0.1193. The friction coefficient was not the lowest because that of the template molecule was relatively high.
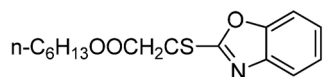
Fig. 36 The structural formula of the compound.

In triisodecyl trimellitate, the Fig. 37 isostere is the appropriate additive because the width of the wear scar was 0.472 mm and the friction coefficient was 0.0946. Although the anti-wear performance was not very good, the tribological properties were excellent because the template molecule performed adequately.
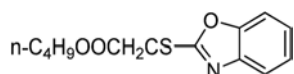
Fig. 37 The structural formula of the compound.

In TMPTO, the Fig. 38 isostere is the suitable additive. The width of the wear scar was 0.812 mm and the friction coefficient was 0.1086.
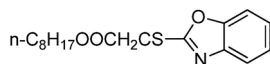
Fig. 38 The structural formula of the compound.

Although the resulting tribological properties of the screened isosteres in the corresponding lubricant base oils are not optimal, the purpose of the isostere molecular design was achieved, that is to say, the sulfur content was reduced and the resulting compounds displayed excellent comprehensive tribological properties within the same group.

3.4 Feasibility of isostere molecular design

3.4.1 *Thiobenzothiazole compounds*

Within a ±5% deviation for the anti-wear effect, there are 11 molecules (30.56% of the isosteres) while there are 17 isosteres (47.22% of the isosteres) within a ±5% deviation for the friction-reduction effect. Within a ±5% deviation for either the anti-wear effect or friction-reduction effect, there were 28 experiment groups

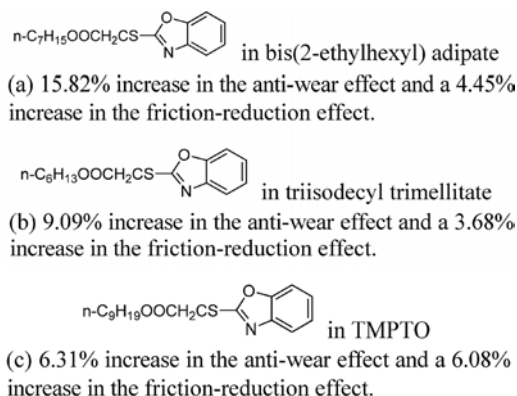(38.89% of all groups). If we assume that the good isosteres were those that are within a ±5% deviation, the lowest proportion of the data for the three groups is then 30.56%.

3.4.2 *2-benzothiazole-S-carboxylic acid esters*

Within a ±5% deviation for the anti-wear effect, there were five molecules (27.78% of the isosteres) while there were 14 isosteres (77.78% of the isosteres) within a ±5% deviation for the friction-reduction effect. Within a ±5% deviation for either the anti-wear effect or friction-reduction effect, there were 19 experiment groups (52.78% of all experiments). If we assume that the good isosteres are those that are within a ±5% deviation, the lowest proportion of the data for the three groups is then 27.78%.

Ignoring the specific molecular structure, for a deviation within a ±5% deviation, the ratio of the isosteres is about 30%. If a template molecule with better tribological properties is found, it could then be assumed that better isostere additive molecules will follow.

Isosteric design is a new development of the authors' previous QSTR work and it tries to use isosteres to mimic the template compound. Like the isosteric applications in the pharmaceutical field, the tribo-ability of the isosteres may be increased, weakened, or yield an adverse effect. This is the reason why wear scar widths and the friction coefficients that have been reported are relatively greater than those from the results obtained from traditional additives. For this works' research, however, and relative to the template molecules, about 30% of the isosteres exhibited satisfactory tribological performance (only ±5% deviations). In addition, some isosteres even improved both friction-reduction and anti-wear performances by a large amount. The absolute performance of the compounds currently obtained may not be satisfactory, but it is possible to achieve the excellent performance required after further optimization.

3.5 Effect of isostere follow-up related to the base oil

S, O, and NH group entities are considered classic cases of bivalent isosterism, and replacement could induce variations in terms of size, shape, electronic distribu-

tion, chemical reactivity, lipophilicity, and hydrogen bonding capacity. Molecular structure modifications induce changes in tribological activity and mechanisms.

In Tables 1 and 2, it is seen that both the template and isostere molecules in the triisodecyl trimellitate base oil have very good tribological properties. It is an aromatic ester, whereas TMPTO and bis(2-ethylhexyl) adipate are aliphatic esters. In addition, the additive molecules are aromatic heterocyclic compounds. Hence, when the base oil and organic additives molecules are similar in structure, the tribological performance is very good.

3.5.1 CoMFA-QSTR and CoMSIA-QSTR models

CoMFA and CoMSIA methodologies interpret the interaction between drug molecules and receptors, which depend on the difference in the molecular fields surrounding the compounds [31–35]. From this, in the previous research, it was assumed that the interaction between the lubricating medium and friction pairs had some correlation with the molecular fields from the lubricating medium. The friction pairs could "feel" the molecular field of the lubricant in order to achieve the expected tribological performance. With the assumption that the quantitative tribological relationship between lubricant molecules and friction pairs can be determined, the quantitative field parameters can be obtained and the regression analysis can be calculated when the lubricant molecules being compared are aligned in space and their molecular fields mapped to a 3D grid. The structures and the tribological data of different organic compounds, either as lubricant base oils or lubricant additives, were included in the CoMFA- and CoMSIA-QSTR models, respectively. The CoMFA-QSTR and CoMSIA-QSTR models suggest that changes in tribological activity strongly correlate with changes in the molecular force fields of the base oils or organic additives [28, 29].

In fact, the total molecular force field of the lubricant is determined by the interaction of the individual molecular force fields from the lubricant additives and base oils. For this study, the relationship between the tribological performance and the synergetic effect of the molecular force field between lubricant additive and base oil was further studied. CoMFA and CoMSIA prediction models of lubricant additive for the

tribological performance were set up, and base oil as reference would be embedded in the contour maps, respectively.

3.5.1.1 Synergetic effect of the molecular force field between the lubricant additive and base oil for anti-wear

Figures 39–41 presents the CoMSIA contour diagrams of the lubricant additive for wear with an embedded base oil (triisodecyl trimellitate, bis(2-ethylhexyl) adipate, or TMPTO) as reference for both steric and electrostatic fields, respectively. In Figs. 39–41, the contours in green indicate the portion of the molecule where steric bulk is favored for wear while the yellow contours represent the reduction in wear performance of the molecules, and the contours in blue show where positive charge is favored for wear while the red region suggest where negative charge is favored for wear.

In Fig. 39, the relatively greater volume distribution of triisodecyl trimellitate is concentrated in or around the yellow region, one electronegative oxygen atom appears in the blue positions, and one carbon atom with a partial positive charge emerges in a red position. Figure 39 illustrates that it has good consistency with the molecular force field of additives and base oil, and this is the reason why the template molecules and isosteres in triisodecyl trimellitate exhibit very good anti-wear properties.
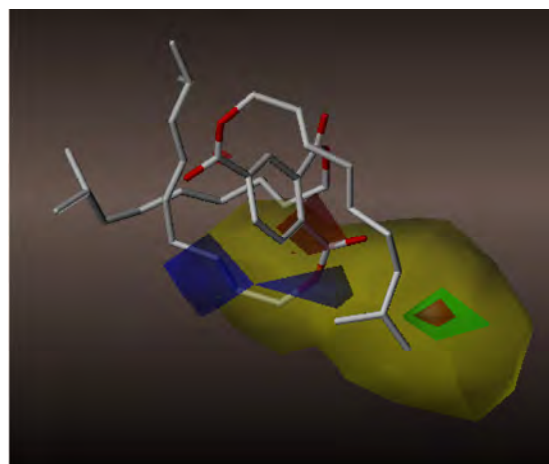

Fig. 39 CoMSIA contour diagram for wear with embedded triisodecyl trimellitate as reference for both steric and electrostatic fields. Green and yellow regions show where steric bulk is favored and disfavored, respectively. Blue region shows where positive charge is favored while red region shows where negative charge is favored.

Comparing Fig. 40 with Fig. 39, less steric bulk appears in the yellow positions, and one electronegative atom O is present in a red position. This indicates a poor coordination of the molecular field of the additives and base oil. In addition, this indicates that the anti-wear activity of the system is not suitable when employing bis(2-ethylhexyl) adipate as base oil.

Figure 41 shows that more steric bulk appears in or around the yellow positions, suggesting that the molecular structure will benefit the anti-wear activity due to the synergistic effect of the steric field of the additives and base oil. However, one electronegative oxygen atom and one ester group appear in the red positions, and one carbon atom with a partial positive charge emerges in a blue position. This means that

Fig. 40 CoMSIA contour diagram for wear with embedded bis(2-ethylhexyl) adipate as reference for both steric and electrostatic fields. Green and yellow regions show where steric bulk is favored and disfavored, respectively. Blue region shows where positive charge is favored while red region shows where negative charge is favored.

Fig. 41 CoMSIA contour diagram for wear with embedded TMPTO as reference for both steric and electrostatic fields. Green and yellow regions show where steric bulk is favored and disfavored, respectively. Blue region shows where positive charge is favored while red region shows where negative charge is favored.

the polar groups or atoms do not present themselves in the appropriate positions and that the anti-wear performance of the lubricant is relatively poor when using TMPTO as a base oil.

3.5.1.2 Synergetic effect of the molecular force field between the lubricant additive and base oil for friction-reduction

The contour diagrams of lubricant additive are provided for friction with embedded base oils triisodecyl trimellitate, bis(2-ethylhexyl) adipate, or TMPTO as reference in Figs. 42–44, respectively. The contours for the steric field are in Figs. 42 and.44, wherein the green color indicates the portion of the molecule where steric bulk is favored for friction and the yellow contours represent the reduction in friction performance of the molecules. The contours for both steric and electrostatic fields are shown in Fig. 43. Here, the contours in green indicate the portion of the molecule where steric bulk is favored for friction while the yellow contours represent the friction-reduction performance of the molecules，and the contours in blue show where a positive charge is favored for friction while the red region show where a negative charge is favored for friction. Figure 42 highlights the good synergistic effect of the steric field with lubricant additives and base oil. The friction-reduction activity of the lubricant is good when triisodecyl trimellitate was employed as the lubricating base oil. Comparing Fig. 44 with Fig. 42, relatively less steric bulk emerges in the yellow

Fig. 42 CoMSIA contour diagram for friction with embedded triisodecyl trimellitate as reference for steric field. Green and yellow regions show where steric bulk is favored and disfavored, respectively.
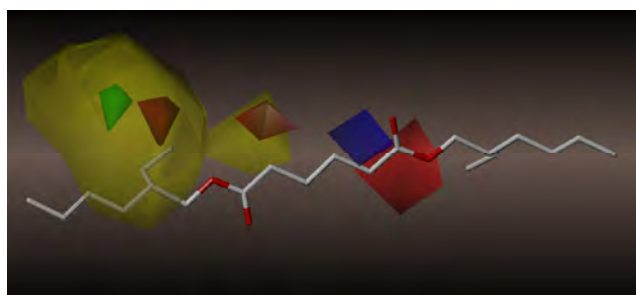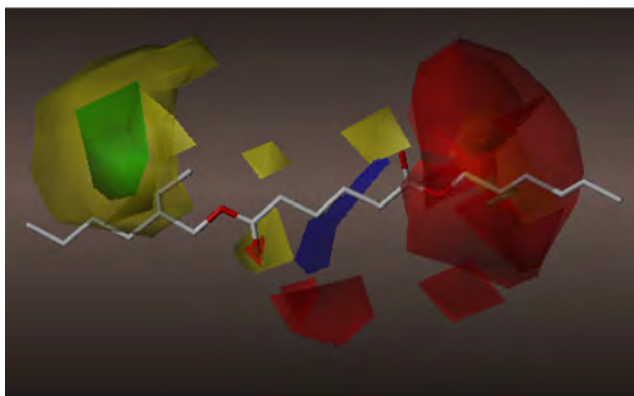
Fig. 43 CoMFA contour diagram for friction with embedded bis(2-ethylhexyl) adipate as reference for both steric and electrostatic fields. Green and yellow regions show where steric bulk is favored and disfavored, respectively. Blue region shows where positive charge is favored while red region shows where negative charge is favored.
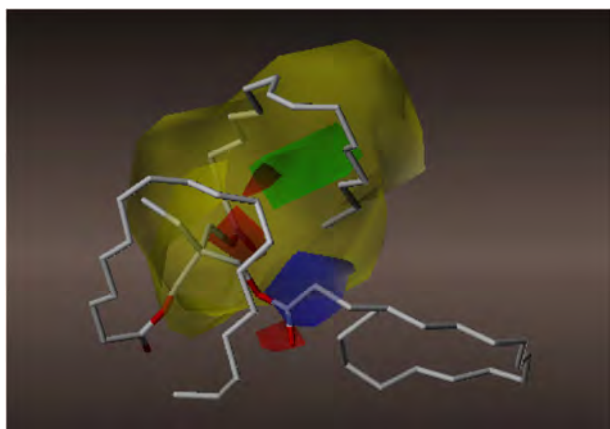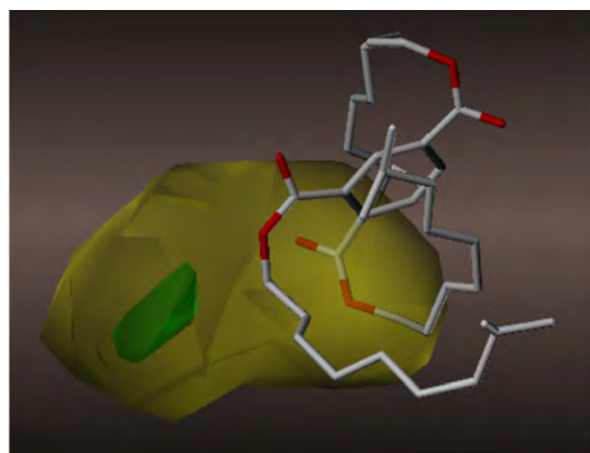

Fig. 44 CoMSIA contour diagram for friction with embedded TMPTO as reference for steric field. Green and yellow regions show where steric bulk is favored and disfavored, respectively.

positions, indicating that the friction-reduction performance of the lubricant (TMPTO as base oil) is not good enough. In Fig. 43, less steric bulk appears in the yellow positions and one electronegative oxygen atom and one ester group appear in or near red positions. This implies that the molecular force fields between the lubricant additive and base oil contradict each other and that the friction-reduction performance of the lubricant is relatively poor when using bis(2-ethylhexyl) adipate as the base oil.

The analysis results of the six figures are consistent with the anti-wear or friction-reduction experimental

results. The models suggest that the tribological properties are related to the synergetic effect of the molecular force fields of the organic additives and base oils. Comparing the three base oils, triisodecyl trimellitate has greater structural similarities to organic additives molecules than TMPTO and bis(2-ethylhexyl) adipate. This is because triisodecyl trimellitate is an aromatic ester while TMPTO and bis(2-ethylhexyl) adipate are aliphatic esters and because the additive molecules are aromatic heterocyclic compounds. In the experimental results, it can be seen that both the template and isostere molecules in the triisodecyl trimellitate base oil have very good tribological properties. Hence, when the base oil and organic additives molecules are similar in structure, a good synergetic effect of the molecular force field results. Thus, it can be assumed that for higher structural similarities, the molecular force fields are more synergic and that the corresponding lubricants will synergistically improve the tribological properties. The CoMFA and CoMSIA studies also imply that the models would be helpful in discovering appropriate lubricant base oils for the specified additives.

3.5.2 BPNN-QSTR, EVA-QSTR and BRNN-QSTR models

We also found during the BPNN-QSTR studies that some processes, such as the diffusion of additive molecules in base oil, have important effects on lubrication under low loads (e.g., 98 N) [23–25]. This is due to the relatively thick base oil layer between the friction pair. Moreover, higher structural similarities of the additive and base oil molecules also lead to easier diffusion. Structural similarity is therefore a positive enhancement for tribological performance.

For the EVA-QSTR work, the results show that when liquid paraffin was employed as the base oil, the effect of heteroatom replacement in the aromatic ring on EVA spectra was very small, as was also their modifying contribution to the tribological performance [26]. Moreover, because the EVA descriptor is used to calculate rotational energy levels of a three-dimensional (3-D) conformation, the aromatic ring can be regarded as a rigid system with restricted bond rotation motion. However, the test results in this work demonstrated

that when an ester was used as the base oil, heteroatom replacements in the aromatic ring have a relatively large effect on the tribological properties. The reason may lie in the differing tribological mechanisms between polar additives that are dissolved in non-polar liquid paraffin as opposed to being dissolved in polar esters. There are no changes in charge, polarity, or electrostatic fields in a non-polar base oil, whereas changes in a polar base oil can affect the interaction with polar additives and polar base oil. Changes in an aromatic heterocyclic ring can affect the tribological properties of an ester base oil. Therefore, in future modeling studies, it will be necessary to choose reasonable parameters corresponding to different base oils. For example, for a strong electrostatic field correlation between base oils and organic additives, relevant quantum descriptors in regards to charge and electric field distributions should be introduced. In fact, EVA is used to predict rotational infrared (IR) spectra. The EVA descriptor only yields changes in chemical bonding only for a 3-D conformation. In addition, while it can give a more accurate description of the fine features in the IR wavelength range it does not produce electric charge descriptions.

In the BPNN-QSTR or BRNN-QSTR model, some influential descriptors representing polarity characteristics of the molecules are introduced [27]. The dipole moment represents the molecular polarity whereas the quadrupole and octopole moments not only represent the orientation of polar molecules, but also how the molecules are related to charge in space. Spatial distributions of charge and electric fields have large surface effects on tribological processes. In future work, tribological features of different models for the same group of organic additive molecules in different base oils will be compared by the authors. Of particular importance are the intermolecular interactions between the base oil and the additives.

Moreover, tribology processes depend on the surface chemical reactions occurring under rubbing conditions and loading. Regrettably, previous isosteres study rarely involved surfaces, but our preliminary results show that it really works in the tribological research. Certainly, in the next optimization process, the surface reactions will be considered.

4 Conclusions

Based on the known chemical structures of lubricant additives, the design and synthesis of new structural analogs, or structure-related compounds, containing less sulfur have been identified with similar or improved tribological characteristics. Isosterism is an effective strategy for designing lubricant additives *via* molecular modification. Molecular modification also allows for the identification of template molecules that exhibit effective tribological characteristics, which minimizes synthetic efforts and, consequently, maximizes the potential successes for lubricant additives with reduced environmental risks.

By using the principle of isosterism, it is feasible to continue synthesizing compounds that exhibit optimal tribological performances. In future work by the authors, the sulfur atoms in the template molecule will be completely replaced and the sulfur-free friction-reduction and anti-wear lubricant additives will be evaluated. Because of the simple, effective, and intuitive features of isosterism, it is anticipated that it will be more widely used in tribology.

Acknowledgments

References

[1] Spikes H. Low- and zero-sulphated ash, phosphorus and sulphur anti-wear additives for engine oils. *Lubrication Science* **20**(2): 103–136 (2008)

[2] Froeschmann R, Spruegel F. Sulfur and phosphorus bearing lubricant. U.S. Patent 3 840 463, Oct. 1974

[3] Gao F, Kotvis P V, Tysoe W T. The surface and tribological chemistry of chlorine- and sulfur-containing lubricant additives. *Tribology International* **37**(2): 87–92 (2004)

[4] Zinke H, Lorenz J. Lubricant compositions containing sulfur-containing esters of phosphoric acid. U.S. Patent 4 197 209, Apr. 1980

[5] Evans R D, More K L, Darragh C V, Nixonetal H P. Transmission electron microscopy of boundary-lubricated bearing surfaces. Part II: Mineral oil lubricant with sulfur- and phosphorus-containing gear oil additives. *Tribology Transactions* **48**(3): 299–307 (2005)

[6] Coyle C L, Greaney M A, Stiefel E I, Francis J N, Beltzeretal M. Molybdenum sulfur antiwear and antioxidant lube additives. U.S. Patent 4 995 996, Feb. 1991

[7] DiBiase S A, Pialet J W. Sulfur-containing lubricant and functional fluid compositions. U.S. Patent 4 800 031, Jan. 1989

[8] Love D, Schlicht R C, Biasotti J B. Lubricant additive. U.S. Patent 4 765 918, Aug. 1988

[9] Malec R E. Lubricant composition of improved friction reducing properties. U.S. Patent 4 201 684, May. 1980

[10] Thornber C W. Isosterism and molecular modification in drug design. *Chemical Society Reviews* 8(4): 563–580 (1979)

[11] Willett P, Barnard J M, Downs G M. Chemical similarity searching. *Journal of Chemical Information and Computer Sciences* **38**(6): 983–996 (1998)

[12] Nikolova N, Jaworska J. Approaches to Measure Chemical Similarity–A review. *Qsar & Combinatorial Science* **22**(22): 1006–1026 (2004)

[13] Lima L M, Barreiro E J. Bioisosterism: a useful strategy for molecular modification and drug design. *Current Medicinal Chemistry* **12**(1): 23–49 (2005)

[14] Patani G A, La Voi E J. Bioisosterism: A rational approach in drug design. *Chemical Reviews* **96**(8): 3147–3176 (1996)

[15] Meanwell N A. Synopsis of some recent tactical application of bioisosteres in drug design. *Journal of Medicinal Chemistry* **54**(8): 2529–2591 (2011)

[16] Brown N. *Bioisosteres in Medicinal Chemistry. Methods & Principles in Medicinal Chemistry.* Weinheim (GER): Wiley-VCH, 2012

[17] Burger A. Isosterism and bioisosterism in drug design. In *Progress in Drug Research.* Basel (CH): Birkhauser, 1991: 287–371.

[18] Bhattacharya A, Singh T, Verma V K, Nakayama K. The role of certain substituted 2-amino-benzothiazolylbenzoylthio-carbamides as additives in extreme pressure lubrication of steel bearing balls. *Wear* **136**(2): 345–357 (1990)

[19] Wan Y, Pu Q, Xue Q, Su Z. Antiwear and extreme pressure

characteristics of 2-mercaptobenzothiazole derivative as the potential lubricating oil additive. *Wear* **192**(1): 74–77 (1996)

[20] Zhang J, Liu W, Xue Q. Tribological properties of the film formed by 2-(n-dodecyldithio)-benzothiazole as additive in liquid paraffin. *Wear* **236**(1): 34–38 (1999)

[21] Wu H, Fan K, Li J, Ren T, Ji K. Anti-wear performance and chemical property of films of nitrogen-containing heterocyclic lubricating oil additive. *Acta Phys–Chim Sin* **23**(06): 911–915 (2007)

[22] Li Z, Li X, Zhang Y, Ren T, Zhao Y, Zeng X. Tribological study of a highly hydrolytically stable phenylboronic acid ester containing benzothiazolyl in mineral oil. *Applied Surface Science* **308**: 91–99 (2014)

[23] Dai K, Gao X. Estimating Antiwear properties of lubricant additives using a quantitative structure tribo-ability relationship model with back propagation neural network. *Wear* **306**(1–2): 242–247 (2013)

[24] Gao X, Wang Z, Zhang H, Dai K, Wang T. Quantitative Structure Tribo-ability relationship model for ester lubricant base oils. *Journal of Tribology* **137**(2): 021801-1–021801-7 (2015)

[25] Gao X, Wang R, Wang Z, Dai K. BPNN-QSTR Friction model for organic compounds as potential lubricant base oils. *Journal of Tribology* **138**(3): 031801–031801-8 (2016)

[26] Gao X, Wang Z, Zhang H, Dai, K. Three dimensional quanti-tative tribo-ability relationship model. *Journal of Tribology* **137**(2): 021802-1–021802-8 (2015)

[27] Gao X, Dai K, Wang R, Wang Z, Wang T, He J. Establishing quantitative structure tribo-ability relationship model using Bayesian regularization neural network. *Friction* **4**(2): 105–115 (2016)

[28] Gao X, Liu D, Wang Z, Dai K. Quantitative structure tribo-ability relationship for organic compounds as lubricant base oils using CoMFA and CoMSIA. *Journal of Tribology* **138**(3): 031802-031802-7 (2016)

[29] Liu D, Yang Q, Wang Y, Wang R, Dai K, He J. CoMFA-QSTR and CoMSIA-QSTR models about N-containing Heterocyclic derivatives as lubricant additives about anti-wear property. *Tribology* **36**(4): 421–429 (2016)

[30] Liu D. The study on the synthesis and tribological properties of green antiwear lubricant additives. Master dissertation. Wuhan (China): Wuhan Polytechnic University, 2016

[31] Cramer R D III, Patterson D E, Bunce J D. Recent advances in comparative molecular field analysis (CoMFA). *Prog Clin Biol* **291**: 161–165 (1989)

[32] Cramer R D. III, Patterson D E, Bunce J D. Comparative molecular field analysis (CoMFA). 1. Effect of shape on

binding of steroids to carrier proteins. *J Chem Soc* **110**(18): 5959–5967 (1988)

[33] Kubinyi H, Folkers G, Martin Y C. *3D QSAR in Drug Design, Recent Advances.* Berlin (GER): Springer Netherlands, 1998.

[34] Klebe G, Abraham U, Mietzner T. Molecular similarity indices in a comparative analysis (CoMSIA) of drug molecules tocorrelate and predict their biological activity. *J Med Chem* **37**(24): 4130–4146 (1994)

[35] Klebe G, Abraham U. Comparative molecular similarity index analysis (CoMSIA) to study hydrogen-bonding properties and to score combinatorial libraries. *J Comput-Aided Mol Des* **13**: 1–10 (1999)

Xinlei GAO. She received her M.S. degree in 1996 from Huazhong Normal University in organic chemistry, and graduated from Wuhan Research Institute of Materials Protection in mechanical design and theory with Ph.D. degree in 2006. Currently she is a full professor at Wuhan Polytechnic University, member of Chinese Tribology Association. She is interested in tribology chemistry, chemical computing, and designation of lubricant.

Combined effect of the use of carbon fiber and seawater and the molecular structure on the tribological behavior of polymer materials

Zhiqiang WANG[1,2,*], **Jing NI**[1], **Dianrong GAO**[3]

[1] *School of Mechanical Engineering, Hangzhou Dianzi University, Hangzhou 310018, China*

[2] *State Key Laboratory of Fluid Power and Mechatronic Systems, Zhejiang University, Hangzhou 310058, China*

[3] *College of Mechanical Engineering, Yanshan University, Qinhuangdao 066004, China*

Abstract: The combined effect of the use of carbon fiber and seawater and the molecular structure on the tribological behavior of various polymer materials under natural seawater lubrication was investigated. After the investigation, the wear morphology of the contact surface was observed by a laser scanning confocal microscope, and the texture of the wear scars and tracks were presented in 3D profiles. Moreover, the mechanism of mixed lubrication and wear resistance was analyzed. The results demonstrated that the friction coefficient of carbon fiber-reinforced polyetheretherketone (CFRPEEK) is the lowest and fluctuates at approximately 0.11. Moreover, the seven polymer materials in ascending order of friction coefficients are CFRPEEK, carbon fiber-reinforced polyamide-imide, polytetrafluoroethylene, polyoxymethylene, polyetheretherketone (PEEK), acrylonitrile butadiene styrene resin, and glass fiber–epoxy resin. More critically, the simultaneous incorporation of deposition, polymeric scrap, hydrophilic groups, and seawater resulted in a decrease in the friction and wear of polymer materials under seawater lubrication. This observation implies that a synergistic friction-reducing and wear-resistant effect exists between carbon fiber, seawater, and the molecular structure of PEEK. As a result, a highly effective polymer material was discovered, CFRPEEK, which has the lowest friction coefficient of 0.11 and lowest wear rate of 2×10^{-5} mm³·(N·m)⁻¹ among the polymer materials; this validates the selection of dual friction pairs for seawater hydraulic components.

Keywords: friction coefficient; wear; molecular structure; polymer materials; seawater lubrication

1 Introduction

With industrialization and population growth, the problems of resource shortage and environment pollution have intensified. Marine exploitation is the primary means of expanding human living space and facilitating the further development. Oceans, covering more than 71% of the earth's surface, form an abundant water resource. Natural water has become the most popular hydraulic transmission system medium in place of oil. However, the physical and chemical properties of seawater, such as low lubricity and high

causticity, result in numerous challenges. Consequently, research into the tribological performance of friction pairs in seawater environment is critical for seawater hydraulic components.

Compared with metal, polymer materials exhibit higher performance in terms of self-lubrication, friction properties, and wear and corrosion resistance [1–3]. These advantages render them more adaptable to underwater environment. Therefore, a number of international scholars conducted numerous studies on the friction and wear characteristics of polymer materials. Chen et al. [4] prepared carbon fiber and

---

* Corresponding author: Zhiqiang WANG, E-mail: wangzq@hdu.edu.cn

polyimide composites simultaneously reinforced with polytetrafluoroethylene (PTFE) and determined that the incorporation of polyimide (PI) and carbon fiber (CF) contributes toward significantly enhancing the wear resistance of PTFE. Dubey et al. [5] reported the effects of nanosized PTFE particles as a solid lubricant. The results demonstrated that PTFE particles significantly enhance the weld load, as well as antiwear and friction reduction properties. Ye et al. [6] used interrupted microscopy measurements to investigate the evolution of transfer film development for an ultra-low-wear PTFE nanocomposite.

Hedayati et al. [7] observed that semicrystalline pure polyetheretherketone (PEEK) coating exhibited higher hardness and lower adhesion strength, coefficient of friction, and wear rate than the amorphous one. Chen et al. [8] investigated the friction and wear behaviors of PEEK/PEI/PES alloys under dry sliding contact condition and reported that wear resistance of the alloys were considerably higher than those of pure polyetherimide (PEI) and polyarylethersulfone (PES). Tang et al. [9] researched on the tribological characteristics of carbon fiber-reinforced polyetheretherketone (CFRPEEK) sliding on Si_3N_4 lubricated with water and determined that the sliding velocity has a higher effect on friction than pressure does. Rasheva et al. [10] reported that fiber orientation influences the mechanical performance and tribological properties of short-carbon fiber-reinforced PEEK materials. Chen et al. [11] investigated the tribological behaviors of CFRPEEK and observed that the incorporation of CF significantly enhances the wear resistance of PEEK under seawater lubrication.

Pihtili [12] prepared glass fiber–epoxy resin (GFER) composites and determined that the weight loss of the woven GFER composite increased with increasing load and speed. Basavarajappa and Ellangovan [13] suggested that 5% silicon carbide and 5% graphite filled the glass–epoxy composites exhibited remarkably high wear resistance. Siddhartha and Gupta [14] observed chopped glass fiber-reinforced composites to exhibit higher performance than bidirectional glass fiber-reinforced composites under abrasive wear situations. Suresha et al. [15] reported that silicon carbide-filled glass-epoxy (G-E) composite exhibits higher resistance to slide wear compared to plain G-E composites.

Difallah et al. [16] investigated the mechanical and tribological response of acrylonitrile butadiene styrene (ABS) polymer matrix filled with graphite powder and determined that the addition of graphite in ABS matrix lowers friction coefficient and wear. Huseyin et al. [17] researched on the tribological performance of industrial PAI in a cooling environment without air cooling and observed that the coefficient of friction marginally decreased and wear rates increased with increase in load and sliding speed.

Mergler et al. [18] reported that the friction coefficient of polyoxymethylene (POM) sliding against stainless steel starts at a relatively low level of approximately 0.2 and increases to higher values after 20 h of sliding owing to material transfer. Cho et al. [19] investigated the effect of surface texturing on the friction of POM and determined that the lowest friction coefficient was obtained with a 10% texturing density. Chaudri et al. [20] investigated the frictional performance of PBT + PTFE pin sliding against POM; the results indicated that the decrease in friction at higher loads is due to softening of the PBT pin by frictional heating.

Although the tribological behavior of polymer materials was investigated, the studies mainly focused on dry friction and pure water lubrication. These studies are focused on material modification of fillers; however, the combined effects of seawater and molecular structure of matrix and carbon fiber are seldom discussed. In the field of metal matrix composites, Bajwa et al. [21–23] investigated the wear and corrosion resistance properties of Ni-base composite and the microstructure of electrodeposited coatings under water lubrication and nano-enhanced lubrication. They reported that the nickel composite of nanosized alumina exhibits the maximum corrosion resistance.

In the present study, tribological experiments of 316L against PTFE, PEEK, CFRPEEK, GFER, ABS resin, carbon fiber-reinforced polyamide-imide (CFRPAI), and POM under natural seawater lubrication were conducted by using an MMU-5G ring-on-disk friction and wear tester. In this study, the wear morphology and texture of the wear scars and tracks on the contact surfaces were investigated, and the mechanisms of mixed lubrication and wear resistance were analyzed.

2 Experimental details

2.1 Preparation of seawater and materials

In this study, natural seawater sourced from China's Bohai Bay was prepared [24]. The pH and salinity of the seawater are 7.2 and 2.983%, respectively. The test materials included PTFE, PEEK, GFER, ABS resin, CFRPAI, POM, and CFRPEEK. The main performance parameters are presented in Table 1. All the specimens were washed in an ultrasonic ethanol bath for 15 min and then air-dried to ensure the cleanliness of material's surface.

2.2 Test specimens

The dimensions of the upper specimen ring and bottom specimen disk were Φ26 mm (outer diameter) × Φ20 mm (inner diameter) and Φ43 mm (diameter) × 3 mm (height), respectively. The upper specimen ring and bottom specimen disk were fabricated from stainless steel 316L (the composition is presented in Table 2) and polymer, respectively. Stainless steel 316L was selected as the upper specimen ring in the present research as it is likely that tribological materials

are suitable for the marine environment. Stainless steel 316L has remarkably high wear and corrosion resistance [25, 26] and is widely used to fabricate the friction components of seawater pumps and motors [27, 28]. The properties of stainless steel 316L is presented in Table 3.

2.3 Friction and wear tests

The experiment used ring-disk sliding contact to investigate the friction and wear properties of each friction pair, as illustrated in Fig. 1. The upper specimen rotated around its own central axis under the set load and speed, while the bottom specimen was held stationary. The specimens were set in the box, which was filled completely with seawater in order to realize the continuous sliding of the friction pairs' contact surfaces in seawater. The load is adjusted through manipulating the supply pressure of the hydraulic cylinder, and the rotational speed is adjusted through the frequency speed regulation system. The seawater temperature was measured by a temperature sensor installed beneath the contact surface of the bottom specimen.

Table 1 Properties of polymer materials.

Polymer materials	Density (g/cm³)	Water absorption after 24 h immersion in water at 23 °C (%)	Heat distortion temperature (°C)	Coefficient of thermal expansion (10⁻⁵/°C)	Tensile strength at 23 °C (MPa)	Bending strength at 23 °C (MPa)	Compressive strength (MPa)
PTFE	2.2	0.01	120	10.3	28	18	11
PEEK	1.3	0.5	163	4.7	100	163	118
GFER	1.8	0.04	260	0.4	210	397	310
ABS resin	1.04	0.2	180	2.88	55	80	65
CFRPAI	1.42	0.33	250	2.5	152	235	221
POM	1.41	0.22	124	0.23	98	283	110
CFRPEEK	1.4	0.06	315	1.5	220	298	240

Table 2 Chemical composition of 316L and 9Cr18Mo.

Stainless steel	Composition (wt%)							
	C	Si	Mn	P	S	Ni	Cr	Mo
316L	0.03	1	2	0.035	0.03	10–14	16–18.5	2-3

Table 3 Main performance parameters of 316L.

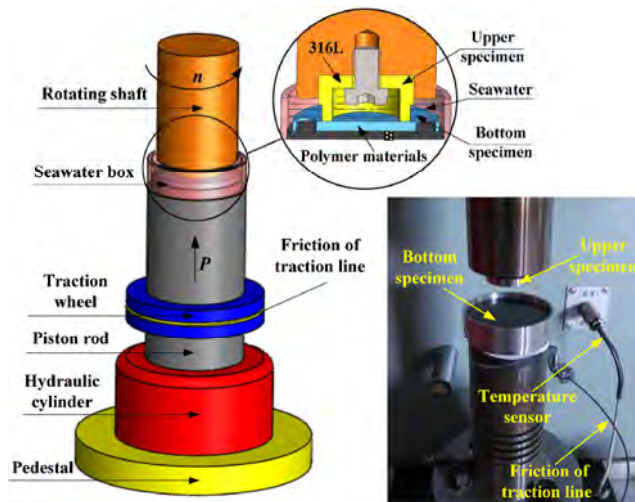| Stainless steel	Density (g/cm³)	Modulus of elasticity (GPa)	Brinell hardness	Elongation (%)	Thermal conductance (W/(m·k))	Coefficient of thermal expansion (10⁻⁶/°C)	Tensile strength (MPa)	Yield strength (MPa)
316L	8.03	206	230	30	16.3	16	620	310

Fig. 1 Installation drawing of ring-on-disc configuration.

The experiments were performed with a rotational speed of 100 r/min (0.12 m/s), load of 100 N, and period of 2 h and used seawater as the lubricant to simulate the actual working environment of the main dual friction pairs in the low-speed and high-torque hydraulic motor. All test parameters are displayed on the computer screen, and the computer recorded the curve of friction factor–time and temperature–time.

Subsequent to the friction and wear test, the depth of the wear track on the bottom specimen was measured using a digital thickness gauge (YG141D) to an accuracy of 0.01 mm. The corresponding wear volume loss ΔV of the specimen was obtained by measuring the wear scar depth. Finally, the specific wear rate ω (mm³/(N·m)) was calculated from the volume loss by using the following equation:

$$\omega = \frac{\Delta V}{2\pi RntF} \qquad (1)$$

where ΔV is the wear volume loss (mm³), R is the mean radius of the upper specimens ring (m), n is the rotational velocity (r/min), t is the wear time (min), and F is the load (N).

2.4 Observation of morphologies of worn surfaces

The worn morphologies of the bottom specimens were observed using a laser scanning confocal microscope to understand the wear mechanism of PTFE, PEEK, GFER, ABS resin, CFRPAI, POM, and CFRPEEK under seawater lubrication. The texture of the wear scars

and tracks were presented in 3D profiles to study its functional mechanisms further. The 3D profiles present the morphology of the contact surface, and the variations in surface topography were represented using various colors.

3 Results

3.1 Analysis of friction and wear of polymer materials

Figures 2 and 3 illustrate the variation of the friction coefficient of 316L against several polymers, with the test time. All the upper specimens were of 316L, while bottom specimens were of PTFE, PEEK, GFER, ABS resin, CFRPAI, POM, and CFRPEEK. The upper specimens rotated at 100 r/min speed and under 100 N load, while the bottom specimens were held stationary.

As illustrated in Fig. 2, the friction coefficient of 316L–PTFE increased rapidly from 0.1 to 0.17 in 10 min and then stabilized at approximately 0.17. After 80 min, it fluctuated around 0.15. The friction
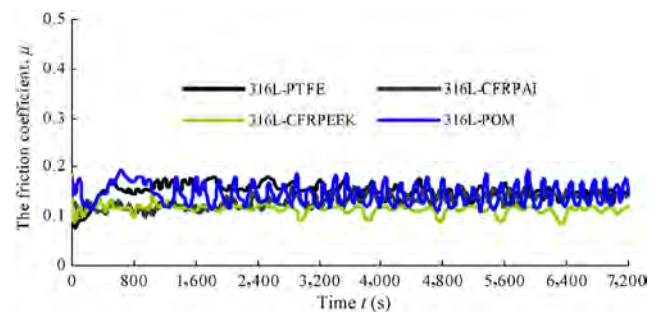

Fig. 2 Variation of the friction coefficient of 316L against PTFE, CFRPAI, CFRPEEK, and POM.
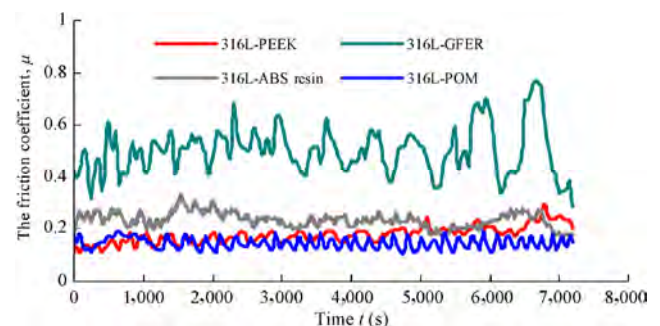

Fig. 3 Variation of the friction coefficient of 316L against PEEK, GFER, ABS resin, and POM.

coefficient of 316L–PTFE is consistently higher than that of 316L–CFRPAI and 316L–CFRPEEK. The friction coefficient of 316L–POM fluctuated between 0.12 and 0.18, which is marginally larger than that of 316L–PTFE. Meanwhile, the friction coefficients of 316L–CFRPAI and 316L–CFRPEEK fluctuated at approximately 0.1 over 25 min. The two friction coefficients did not exhibit a running-in period. Then, the friction coefficient of 316L–CFRPAI gradually increased to become higher than that of the pair whose bottom specimen was CFRPEEK, while the coefficient of 316L–CFRPEEK fluctuated at approximately 0.11. This is because of the molecular structure of PEEK, which has a higher proportion of hydrophilic groups than PAI. With the increase of the test time, the hydrophilic groups cause more water molecules to occupy the clearance. The flowing water better adapts to the action of external shearing force.

As Fig. 3 illustrates, the friction coefficient of 316L–GFER fluctuated from 0.3 to 0.6 before 80 min and abruptly began to fluctuate from 0.3 to 0.9 when the friction coefficient of 316L–ABS resin fluctuated at approximately 0.25. The friction coefficient of 316L–PEEK increased gradually from 0.1 to 0.2 before 80 min and abruptly began fluctuating at approximately 0.3. The friction coefficient of 316L–POM fluctuated from 0.12 to 0.18, which is marginally lower than that of 316L–PEEK. Moreover, the fluctuation of the 316L–POM friction coefficient is the most regular and lowest in the four groups.

By analyzing the variation of the friction coefficient of the 316L pairs against the various polymer materials, the comparison of the various dual friction pairs were obtained as follows: 316L–CFRPEEK < 316L–CFRPAI < 316L–PTFE < 316L–POM < 316L–PEEK < 316L–ABS resin < 316L–GFER. Thus, it is determined that the friction coefficient of 316L–CFRPEEK is the lowest.

The specific wear rates of the seven types of polymers were calculated using Eq. (1), as illustrated in Fig. 4, to investigate the wear extent of the specimens.

Amongst all the specimens, CFRPEEK exhibited the lowest wear rate of 2×10^{-5} mm$^3 \cdot$(N·m)$^{-1}$, while PTFE exhibited the highest wear rate of 75.5×10^{-5} mm$^3 \cdot$(N·m)$^{-1}$. Moreover, the wear rate of CFRPEEK is approximately 2.65% that of PTFE.

The sequence of specific wear rate for the seven
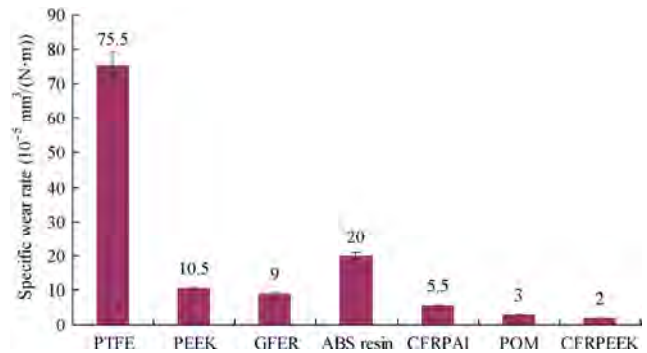
Fig. 4 The specific wear rates of the polymer materials.

polymer materials is: CFRPEEK < POM < CFRPAI < GFER < PEEK < ABS resin < PTFE. This indicates that CFRPEEK exhibits reasonable wear resistance in the process of friction and wear in seawater.

3.2 Analysis of worn surfaces of polymer materials

Figure 5 presents the worn surface micrographs of the various polymer materials. For comparison, the original surface morphologies are also provided. When compared with Fig. 5(a), Fig. 5(b) reveals that the worn surface of PTFE did not apparently exhibit scratch marks. However, particles of stainless steel 316L were observed on the worn surface, indicating that more extensive adhesive wear had occurred on the dual pair 316L–PTFE as a result of the wear test. Similar discovery was also reported in Refs. [29, 30]. Figure 5(d) illustrates that numerous small scratches appeared on the PEEK surface owing to wear, and the original morphology had disappeared. The Original GFER surface was grinded off and numerous small scratches on the worn surface (Fig. 5(f)). Moreover, the GFER surface was set with brown and white elements. The brown elements were dust particles from the worn GFER material, while the white elements were a few dust particles from the 316L. This observation indicates that the smearing and scratching phenomenon of adhesive wear exists on the surface of 316L–GFER as reported by Agrawal [31].

By comparing the original (Fig. 5(g)) with the worn ABS resin surface (Fig. 5(h)), it was determined that the surface had become smooth after the 316L–ABS resin wear test; however, numerous wide scratches were visible on the worn surface. White elements appeared on the ABS resin surface, which indicates
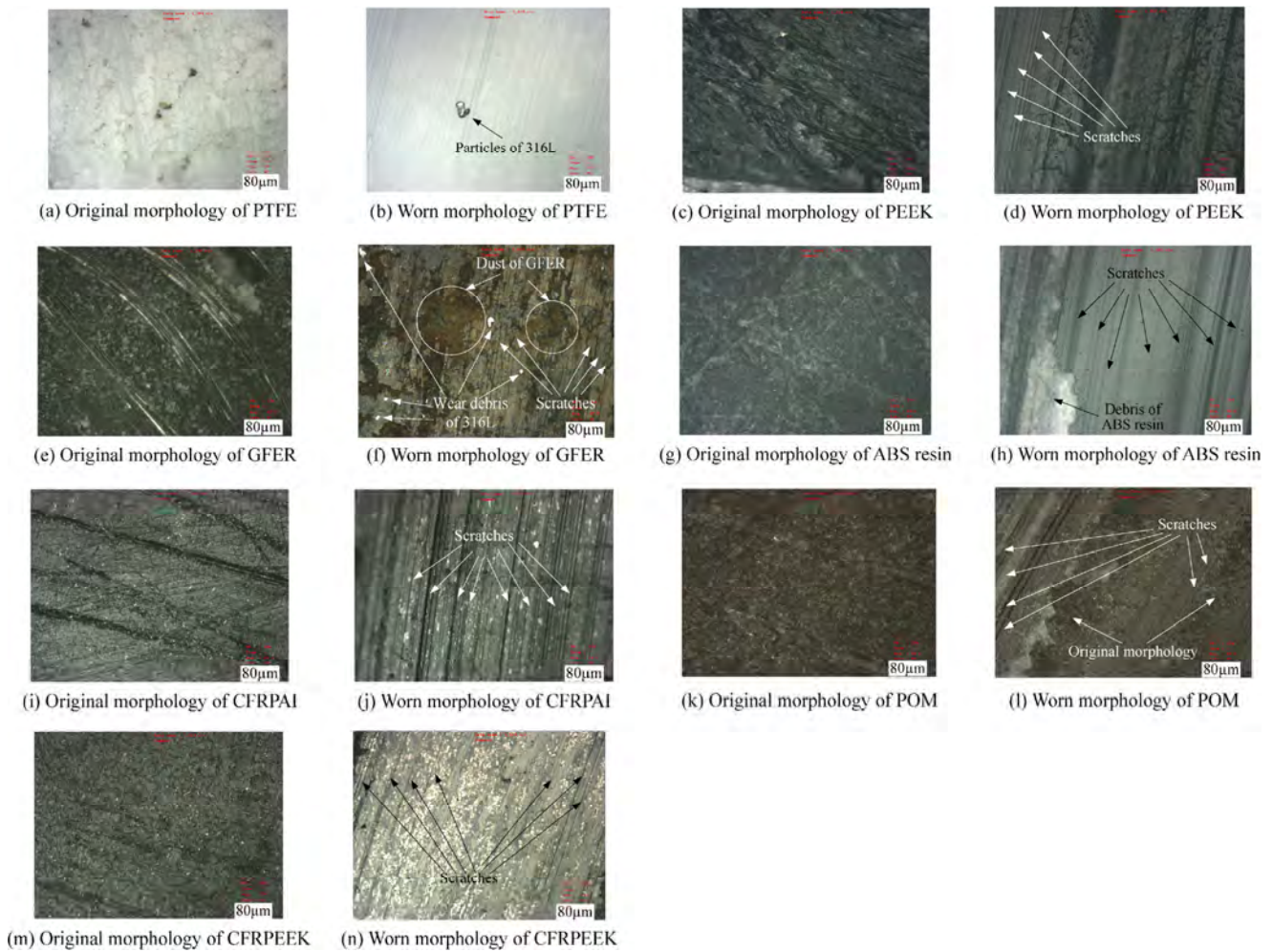
Fig. 5   Original and worn surface morphologies of the various polymer materials.

that falling debris was embedded into the contact surface. This phenomenon is similar to that reported in Ref. [32]. Numerous small scratches appeared on the CFRPAI surface, as illustrated in Fig. 5(j), which reveals that scuffing phenomenon had occurred. Meanwhile, the POM surface indicates the occurrence of the scratch phenomenon in adhesive wear (Fig. 5(l)). The surface wear is not uniform, and the scratches display unequal widths. A part of the original morphology continues to be visible. In addition, the surface morphology of CFRPEEK observed in Figs. 5(m) and 5(n) exhibits a more uniformly worn surface and to a marginal extent exhibits scratch phenomenon with thinner scratches.

A laser microscope was used to scan the 3D morphology of the worn surfaces to analyze the friction and wear features of 316L against the various polymer materials and study their mechanism further. The result is presented in Fig. 6.

Evidence of the plough-and-scratch phenomenon appears on the various types of polymer materials after wear, as illustrated in Fig. 6. Wear characteristics vary with the materials. The PTFE surface material is straightforwardly torn apart and forms the "prod" in the wear process owing to low strength and hardness of pure PTFE, as illustrated in Fig. 6(a). These prods repeatedly scrape the PTFE matrix, and this wear process increases the contact surface temperature. Then, plastic deformation appeared on the PTFE surface material and softened the matrix further, resulting in more extensive wear. The observation is consistent with those of few other researchers [33, 34]. Figure 6(b) illustrates that apparent grinded groove and "prods" appeared on the wear surface, which indicates that
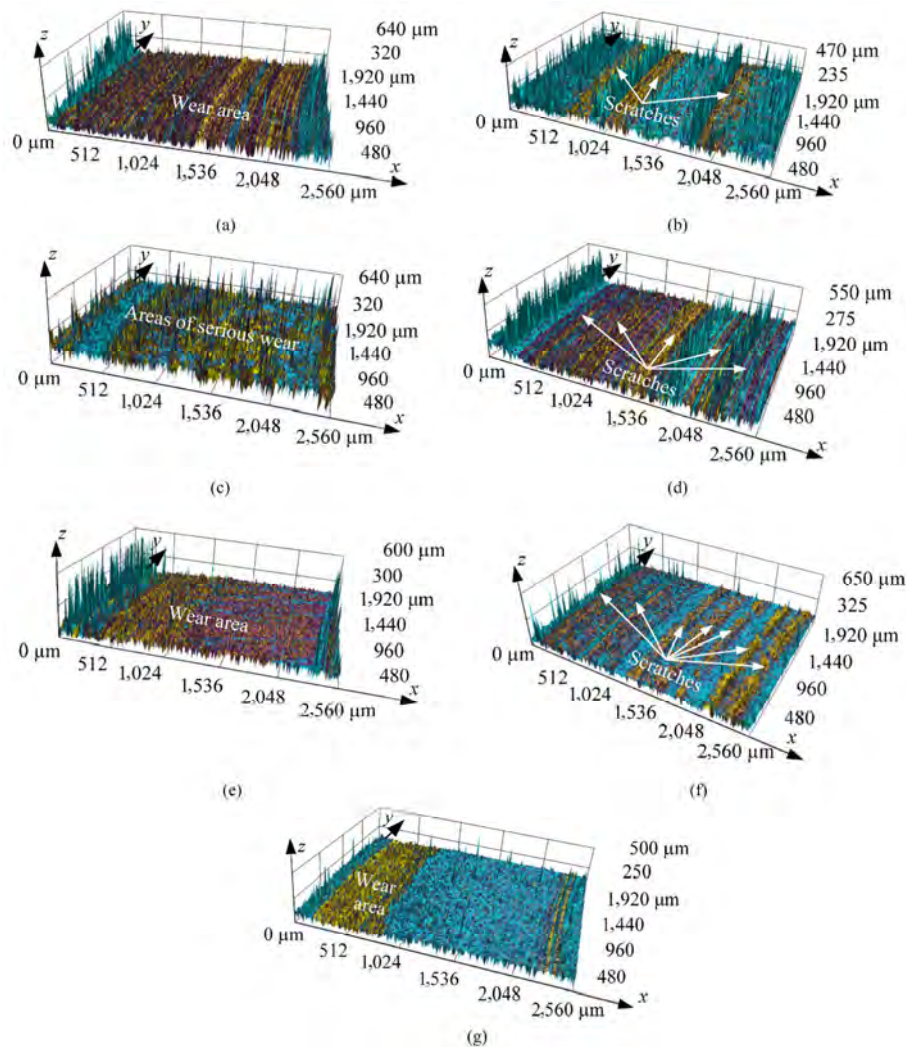
Fig. 6 3-D profiles of wear scars on the (a) PTFE, (b) PEEK, (c) GFER, (d) ABS resin, (e) CFRPAI, (f) POM, and (g) CFRPEEK surfaces after friction experiment lubricated by seawater.

the wear resistance of PEEK is not adequate.

When the bottom specimen is GFER, substantial "needles" appeared on the wear surface (Fig. 6(c)) because the bulges of the contact surface are cut off and the matrix wear debris and small particles are embedded into the surface during the process of wear. Numerous scratches and small grooves appeared on the contact surface (Fig. 6(d)); a number of "needles", which are caused by the wear particles, are visible. The CFRPAI wear surface is smoother than that of several of the abovementioned the above several specimens (Fig. 6(e)). Although there are "needles" and scratches, the scratches are fewer and smaller. Figure 6(f) illustrates that no apparent "needles" appeared on the POM wear surface; however, a number

of wider scratches appeared on the surface.

A small-sized furrow or "needle" is visible on the 3D morphology of the worn surface (Fig. 6(g)) when the bottom specimen is CFRPEEK. A mark of light wear is visible in the linear or lamellate wear area on the contact surface in the direction of friction. Moreover, the worn surface is smooth without extensive scratches or grooves. This observation indicates that CFRPEEK has reasonable wear resistance, anti-attrition, anti-drag, and self-lubrication properties. A similar discovery was also reported in Refs. [11, 35, 36].

3.3 Analysis of wear mechanism in polymer materials

The analysis of the wear morphology reveals that the

wear mechanisms of the selected polymer materials mainly include tiny plough, grinding, and plastic deformation, and the two or more phenomena may occur simultaneously. Therefore, the wear mechanisms of the seven types of polymers are varied.

More extensive adhesive wear had occurred on the surface of PTFE after the wear test. Numerous small scratches and an apparent grinded groove appeared on the wear surface of PEEK, which indicates that the plough and grinding phenomenon occurred. Moreover, evidence of the smearing and scratching phenomenon of adhesive wear is visible on the GFER surface. The smearing phenomenon appears to have occurred on the worn surface, and numerous wide scratches and small grooves were visible. Although the scuffing phenomenon appears to have occurred on the worn surface of CFRPAI, the scratches are fewer and smaller. Evidence of the scratch phenomenon in adhesive wear also appears on the surface of POM, and the wear surface is not uniform. However, the CFRPEEK surface displays a more uniform worn surface and evidence of occurrence of scratch phenomenon to a marginal extent.

In addition, it can be observed in Fig. 6 depicting the 3D wear that mechanical scratches were present on the contact surfaces of the polymer materials. Minute bulges on the rough surface of stainless 316L resemble relatively softer polymer materials, like machine surface of softer polymer materials micro cut by tools continuously. Moreover, floating debris that is suspended in the water box also results in the polymer materials of the bottom specimens in the experiment being cut during the process of friction and wear.

4 Discussion

4.1 Mixed lubricating effect

In this study, the investigation of the tribological behavior of polymer materials is mainly for determining the appropriate counter materials for the port–plate pair of the low-speed high-torque water hydraulic motor. Therefore, the experimental model is similar to the port–plate and the rotor end surface in the low-

speed high-torque water hydraulic motor. According to our previous study [37], the residual pressing force of the port plate pair is marginal. Under low load, it is convenient to form and maintain a seawater film between the stainless steel 316L and polymer materials. As illustrated in Fig. 7, the clearance between the sliding surfaces at the beginning is filled with adequate water. As the test progresses, the contact surfaces gain more severe damage because the seawater film breaks down. Thus, debris is crushed or broken and peeled off from the polymer materials matrix. Then, the sliding surfaces of the friction pair are immersed in a mixed solution of seawater and debris, as illustrated in Fig. 8. The debris of the polymer materials and seawater play a positive role, exhibiting a self-lubricating action and water lubrication in the process of friction and wear.

In addition, seawater exhibits higher performance. In the opinion of Chen [8, 38], seawater exerts a better influence on the sliding surfaces as result of the deposition of Ca^{2+} and Mg^{2+} in the forms of $CaCO_3$ and $Mg(OH)_2$, respectively, onto the surface. The lubricating fluid, including deposition, polymeric scrap, and seawater are the mixed suspension liquid, which exhibits superior lubrication as well as prevents direct contact between the frictional surfaces. It ultimately causes the decrease in friction and wear.
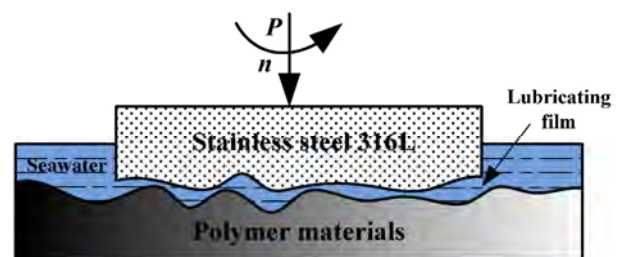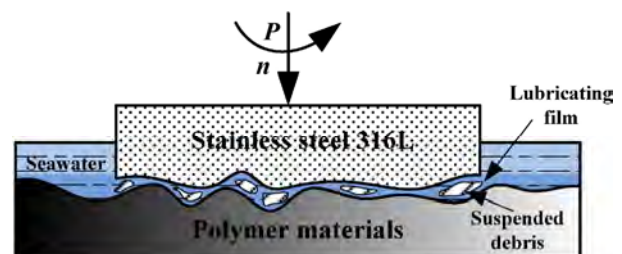

Fig. 7 Model of the beneficial effect of seawater.

Fig. 8 Model of the beneficial effect of debris and seawater.

4.2   Molecular structure effect of polymer materials

Another feasible reason lies in the fact that the molecular structure of polymer materials promotes hydrodynamic lubrication [39], which further enhances the lubricating effect of the friction pair. Figure 8 illustrates the molecular structure of the various polymer materials. As illustrated in the figures, PEEK, GFER, PAI, and POM contained carbonyl groups (C=O) and ether linkage (−O−), which are combined with water molecules by hydrogen bond [40]. Therefore, water molecules aggregated on the surface under the influence of these hydrophilic groups of PEEK, GFER, PAI, and POM, forming a more stable lubrication film. Meanwhile, Figs. 9(a) and 9(d) do not reveal polar hydrophilic groups in the PTFE and ABS resin molecular structures.
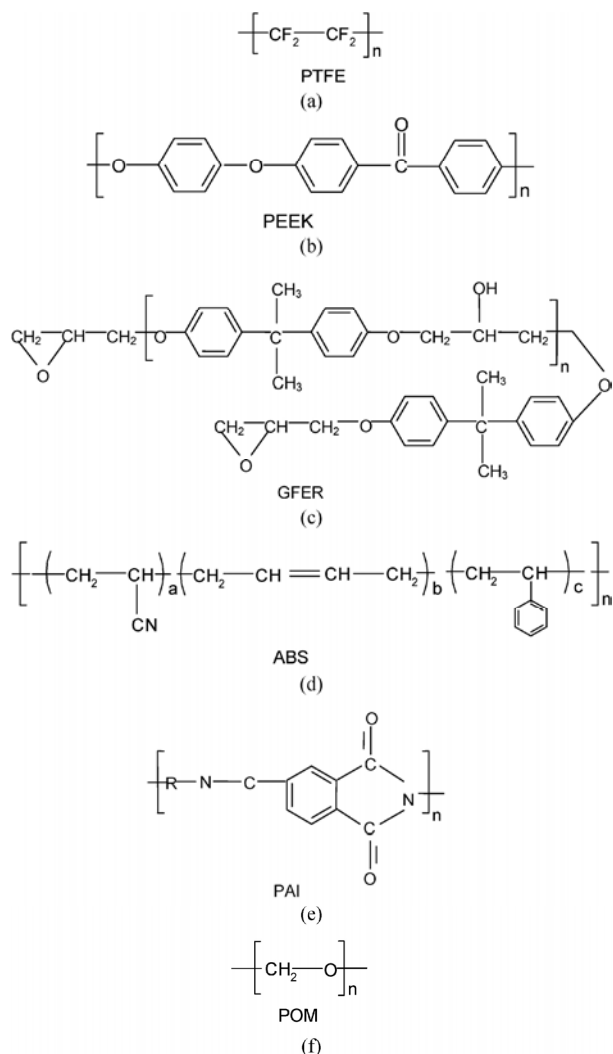
Fig. 9   Molecular structure of (a) PTFE, (b) PEEK, (c) GFER, (d) ABS resin, (e) PAI, and (f) POM.

Therefore, the wear resistance of PTFE and ABS resin is lower than that of PEEK, GFER, PAI, and POM. It is consistent with the calculation results of specific wear rates, as illustrated in Fig. 4.

4.3   The carbon fiber effect

Experimental results demonstrate that polymer materials based on carbon fiber exhibit highly effective friction and wear characteristics under seawater lubrication. With the increment of wear time, the more severe wear of CFRPEEK and CFRPAI is adequately restricted because, according to the reports of Chen [4, 41], the exposed carbon fiber carried the main load. Moreover, CFRPEEK has lower friction coefficient and more effective wear resistance than CFRPAI owing to the molecular structure of PEEK, which has a larger number of hydrophilic groups than PAI. The use of carbon fiber and seawater and the molecular structure produce a synergistic effect on the enhancement of the wear resistance of the polymer materials, which substantiates the apparent decrease in friction and wear of CFRPEEK.

5   Conclusions

Friction and wear experiments of the dual friction pairs in the study are conducted under seawater lubrication. From the results of the experiments, the following conclusions are drawn:

1. The friction and wear test results demonstrate that CFRPEEK has the lowest friction coefficient of 0.11 among the seven types of polymers. Moreover, it exhibits the lowest wear rate of 2×10^{-5} mm$^3 \cdot$(N·m)$^{-1}$ followed by POM, CFRPAI, GFER, PEEK, ABS resin, and PTFE. The wear rate of CFRPEEK is approximately 2.65% that of PTFE.

2. The lubricating fluid in the process of friction and wear, including deposition and polymeric scrap and seawater, is a mixed suspending liquid, which exhibits superior lubrication as well as prevents direct contact between the frictional surfaces. Therefore, it ultimately causes the decrease in friction and wear.

3. The water molecules are aggregated on the surface by the hydrophilic groups of PEEK, GFER, PAI, and POM, forming a more stable lubrication film. On the contrary, the wear resistance of PTFE and ABS resin is lower than that of PEEK, GFER, PAI, and POM

owing to the absence of polar hydrophilic groups in the molecular structure of PTFE and ABS resin.

4. CFRPEEK exhibits effective friction and wear characteristics as well as self-lubricating properties in seawater, as compared to the rest of the polymer materials. This result is attributed to the use of carbon fiber and seawater and the molecular structure of PEEK, which produces a synergistic effect to enhance the friction and wear characteristics of polymer materials.

Acknowledgements

References

[1] Chauhan S R, Kumar A, Singh I. Sliding friction and wear behaviour of vinylester and its composites under dry and water lubricated sliding conditions. *Mater Des* **31**(6): 2745–2751 (2010)

[2] Xie G Y, Sui G X, Yang R. Effects of potassium titanate whiskers and carbon fibers on the wear behavior of polyetheretherketone composite under water lubricated condition. *Compos Sci Technol* **71**(6): 828–835 (2011)

[3] Wang J Z, Yan F Y, Xue Q J. Tribological behavior of PTFE sliding against steel in sea water. *Wear* **267**(9−10): 1634–1641 (2009)

[4] Chen B B, Wang J Z, Yan F Y. Synergism of carbon fiber and polyimide in polytetrafluoroethylene-based composites: Friction and wear behavior under sea water lubrication. *Mater Des* **36**: 366–371(2012)

[5] Dubey M K, Bijwe J, Ramakumar S. PTFE based nano-lubricants. *Wear* **306**(1−2): 80–88 (2013)

[6] Ye J, Khare H S, Burris D L. Transfer film evolution and its role in promoting ultra-low wear of a PTFE nanocomposite. *Wear* **297**(1−2): 1095–1102 (2013)

[7] Hedayati M, Salehi M, Bagheri R. Tribological and mechanical properties of amorphous and semi-crystalline PEEK/SiO$_2$ nanocomposite coatings deposited on the plain carbon steel by electrostatic powder spray technique. *Prog Org Coat* **74**(1): 50–58 (2012)

[8] Chen J B, Guo Q, Zhang S, Wang X M, Shao X L. Research on friction and wear behaviors of PEEK/PEI/PES plastics alloys under sliding contact condition. *Proc Eng* **36**(6): 285–291 (2012)

[9] Tang Q G, Chen J T, Liu L P. Tribological behaviours of carbon fibre reinforced PEEK sliding on silicon nitride lubricated with water. *Wear* **269**(7): 541–546 (2010)

[10] Rasheva Z, Zhang G, Burkhart T. A correlation between the tribological and mechanical properties of short carbon fibers reinforced PEEK materials with different fiber orientations. *Tribol Int* **43**(8): 1430–1437 (2010)

[11] Chen B B, Wang J Z, Yan F Y. Comparative investigation on the tribological behaviors of CF/PEEK composites under sea water lubrication. *Tribol Int* **52**(3): 170–177 (2012)

[12] Pihtili H. An experimental investigation of wear of glass fibre-epoxy resin and glass Fibre-polyester resin composite materials. *Eur Polym J* **45**(1): 149–154 (2009)

[13] Basavarajappa S, Ellangovan S. Dry sliding wear characteristics of glass-epoxy composite filled with silicon carbide and graphite particles. *Wear* **296**(1−2): 491–496 (2012)

[14] Siddhartha, Gupta K. Mechanical and abrasive wear characterization of bidirectional and chopped e-glass fiber reinforced composite materials. *Mater Des* **35**(35): 467–479 (2012)

[15] Suresha B, Chandramohan G, Rao P R S, Sampathkumaran P, Seetharamu S, Venkateswarlu V. Friction and slide wear characteristics of glass-epoxy and glass-epoxy filled with SiCp composites. *Indian J Eng Mater S* **13**(6): 535–541 (2006)

[16] Difallah B B, Kharrt M, Dammak M, Monteil G. Mechanical and tribological response of ABS polymer matrix filled with graphite power. *Mater Des* **34**: 782–787 (2012)

[17] Huseyin U, Mehmet K, Abdullah M. Tribological performance of industrial polyamide-imide and its composite under different cooling conditions. *J Polym Eng* **32**(3):201–206(2012)

[18] Mergler Y J, Schaake R P, Huis in't Veld A J. Material transfer of POM in sliding contact. *Wear* **256**(3): 294–301 (2014)

[19] Cho M H, Park S. Micro CNC surface texturing on polyoxymethylene (POM) and its tribological performance in lubricated sliding. *Tribol Int* **44**(7–8): 859–867 (2011)

[20] Chaudri A M, Suvanto M, Pakkanen T T. Non-lubricated friction of polybutylene terephthalate (PBT) sliding against polyoxymethylene (POM). *Wear* **342**: 189–197 (2015)

[21] Bajwa R S, Khan Z, Bakolas V, Braun W. Water-lubricated Ni-based composite (Ni–Al2O3, Ni–SiC and Ni–ZrO2) thin film coatings for industrial applications. *Acta Metall Sin* **29**: 8–16 (2016)

[22] Bajwa R, Khan Z, Nazir H, Vivek C, Saeed A. Wear and friction properties of electrodeposited Ni-based coatings subject to nano-enhanced lubricant and composite coating. *Acta Metall Sin* **29**: 902–910 (2016)

[23] Bajwa R S, Khan Z, Bakolas V, Braun W. Effect of bath ionic strength on adhesion and tribological properties of pure nickel and Ni-based nanocomposite coatings. *J Adhes Sci Technol* **30**: 653–665 (2016)

[24] GB 17378.4-2007. *The Specifications for Marine Monitoring-Part 4: Seawater Analysis*. Beijing: Standards Press of China, 2008.

[25] Henry P, Takadoum J, Bercot P. Tribocorrosion of 316L stainless steel and TA$_6$V$_4$ alloy in H$_2$SO$_4$ media. *Corros Sci* **51**(6): 1308–1314 (2009)

[26] Sun Y. Corrosion behaviour of low temperature plasm carburised 316L stainless steel in chloride containing solutions. *Corros Sci* **52**(8): 2661–2670 (2010)

[27] Lu Y, Zhao Y Y, Bu G X, Shu P C. The integration of water vane pump and hydraulic vane motor for a small desalination system. *Desalination* **276**(1−3): 60–65 (2011)

[28] Yu GZ, Nie SL, Liu HJ, Yin FL. Repair and experimental study on the key frictional pairs of DANFOSS water pump. *Hydromechatronics Eng* **40**(19): 72–76 (2012)

[29] Wang H Y, Yan L, Gao D, Liu D J, Wang C, Sun L Y, Zhu Y J. Tribological properties of superamphiphobic PPS/PTFE composite coating in the oilfield produced water. *Wear* **319**(1−2): 62–68 (2014)

[30] Wang J Z, Yan F Y, Xue Q J. Tribological behavior of PTFE sliding against steel in sea water. *Wear* **267**(9−10): 1634–1641 (2014)

[31] Agrawal S, Singh K K, Sarkar P K. A comparative study of wear and friction characteristics of glass fibrereinforced epoxy resin, sliding under dry, oil-lubricated and inert gas environments. *Tribol Int* **96**: 217–224 (2016)

[32] Tu CJ, Chen Z H, Chen D, Yan H G, He F Y. Tribological behavior and wear mechanism of resin-matrix contact strip against copper with electrical current. *Trans Nonferrous Met Soc China* **18**(5): 1157–1163 (2008)

[33] Fan B L, Zu D L, Yang U L. Tribological properties of hybrid Kevlar/PTFE fabric reinforced phenolic composite filled with nano-alumina. *Int Conf Mech Autom Control Eng* **2010**: 457–460 (2010)

[34] Unal H, Kurtulus E, Mimaroglu A, Aydin M. Tribological performance of PTFE bronze filled composites under wide range of application conditions. *J Reinf Plast Comp* **29**(14): 2184–2191 (2010)

[35] Xie G Y, Sui G X, Yang R. Effects of potassium titanate whiskers and carbon fibers on the wear behavior of polyetheretherketone composite under water lubricated condition. *Compos Sci Technol* **71**(6): 828–835 (2011)

[36] Wang J X, Gu M Y, Yang R. Wear properties and mechanisms of nylon and carbon-fiber-reinforced nylon in dry and wet conditions. *J Appl Polym Sci* **93**(2): 789–795 (2004)

[37] Wang Z Q, Gao D R. Thrust collar parameter optimization of water hydraulic motor based on orthogonal test. *Chin Mech Eng* **24**(24): 3360–3365 (2013)

[38] Chen B B, Wang J Z, Yan F Y. Frication and wear behaviors of several polymers sliding against GCr15 and 316 steel under the lubrication of sea water. *Tribol Lett* **42**(1): 17–25 (2011)

[39] Klein J. Hydration lubrication. *Friction* **1**(1): 1–23 (2013)

[40] Coles J M, Chang D P, Zauscher S. Molecular mechanisms of aqueous boundary lubrication by mucinous glycoproteins. *Curr Opin Colloid Interf Sci* **15**(6): 406–416 (2010)

[41] Chen B B, Wang J Z, Liu N, Yan F Y. Synergism of several carbon series additions on the microstructures and tribological behaviors of polyimide-based composites under sea water lubrication. *Mater Des* **63**(7): 325–332 (2014)

Zhiqiang WANG. He received his PhD degree from Yanshan University, China, in 2014. He joined School of Mechanical Engineering at Hangzhou Dianzi University from 2014. His current position is a lecturer of the school. His research interests include lubrication mechanism and friction and wear of seawater hydraulic motor. He has participated in numerous research projects like "the National Natural Science Foundation of China", "the National Natural Science Foundation of Zhejiang Province", "the Foundation of State Key Laboratory of Fluid Power and Mechatronic Systems", and a few cooperative businesses projects. He has published more than sixteen papers in international and Chinese journals during the past three years.

Jing NI. He received his PhD degree in 2006 from Zhejiang University. He joined School of Mechanical Engineering at Hangzhou Dianzi University from 2006. His current position is a professor and the deputy director of the School. His work has focused primarily on machine tool and surface engineering. He successively presided over and participated in numerous research projects such as "the National Natural Science Foundation of China", "the National Natural Science Foundation of Zhejiang Province", and a few cooperative businesses projects. He has published more than 30 papers in Chinese academic journals, international journals, as well as international conferences. Moreover, he has been authorized fifteen national invention patents.

Dianrong GAO. He received his PhD degree in 2001 from Yanshan University. His current position is a professor of Yanshan University. During this period, he was invited to visit Louisiana State University as a senior visiting scholar in 2003. Then, he was invited to visit Abdus Salam International Centre for Theoretical Physics (ICTP) as a senior visiting scholar in 2014. He is a member of Chinese Mechanical Engineering Society, Chinese Society of Theoretical and Applied Mechanics, and Fluid Power Transmission and Control of China. His research areas of interest include CFD, PIV and new types of fluid components and devices, and anti-wear and self lubrication. He successively presided and participated in numerous research projects like the National Basic Research Program of China (973), the National Natural Science Foundation of China, and few cooperative businesses projects. He has published more than 130 papers on Chinese academic journals, international journals, as well as international conferences. Moreover, he has been authorized twenty national invention patents.

Study on the influence of standoff distance on substrate damage under an abrasive water jet process by molecular dynamics simulation

Ruling CHEN[1,§,*], **Di ZHANG**[1,2,§], **Yihua WU**[2]

[1] *College of Mechanical Engineering, Donghua University, Shanghai 201620, China*

[2] *Nano-Science and Technology Research Center, Shanghai University, Shanghai 200444, China*

[§] *These authors contributed equally to this paper*

Abstract: The process of a cluster-containing water jet impinging on a monocrystalline silicon substrate was studied by molecular dynamics simulation. The results show that as the standoff distance increases, the jet will gradually diverge. As a result, the solidified water film between the cluster and the substrate becomes "thicker" and "looser". The "thicker" and "looser" water film will then consume more input energy to achieve complete solidification, resulting in the stress region and the high-pressure region of the silicon substrate under small standoff distances to be significantly larger than those under large standoff distances. Therefore, the degree of damage sustained by the substrate will first experience a small change and then decrease quickly as the standoff distance increases. In summary, the occurrence and maintenance of complete solidification of the confined water film between the cluster and the substrate plays a decisive role in the level of damage formation on the silicon substrate. These findings are helpful for exploring the mechanism of an abrasive water jet.

Keywords: standoff distance; crystalline silicon substrate; abrasive water jet; molecular dynamics simulation

1 Introduction

Abrasive water jet (AWJ) operation is described as the impact or collision process of the mixture of the water column and abrasives or clusters. AWJs are widely used in the machining filed, in processes such as abrasive water jet cutting, water jet cleaning, and abrasive water jet polishing (AWJP) [1–3]. Since being developed by Fähnle et al. in 1998 [3], AWJP was proposed to have a wide range of adaptability for machining surfaces, such as spheres, aspheres, and other free-form surfaces [4, 5], in order to obtain a nano-scale smooth surface.

It is widely understood that standoff distance is one of the most important operating parameters of AWJ processes. Generally, the depth of cut will almost linearly decrease as the standoff distance increases during AWJ operation [6, 7]. In addition, the optimum standoff will occur for material-removal processes, or surface damage of impacted substrates [8, 9].

Based on the experimental phenomena mentioned above, the studies on the influence of standoff distance on substrate damage were conducted by Kordonski et al. They found that because of a combination of the absence of lateral limit by nozzle, surface tension variances, and aerodynamic disturbances, the degree of jet divergence increases progressively with the standoff distance [10]. This can make the energy density decrease and eventually lead to a lower jet penetration depth [11]. Thus, magnetorheological jet polishing (MJP), which was developed on basis of AWJ to realize the inhibition of jet divergence,

---

* Corresponding author: Ruling CHEN, E-mail: chen_ruling@163.com

could preserve the stability of the material removal process, even if the standoff distance changes obviously [12].

Using computational fluid dynamics (CFD) simulation, Liu et al. verified that the velocities of the jet would rapidly decay as the standoff distance increases at the "initial region" during an AWJ process [13]. The low velocity will lead to a low degree of substrate damage [14]. In addition, Anglani et al. determined through CFD analysis that the shear stress on the impacted flat surface significantly increases as the standoff distance decreases [8]. In addition, He et al. showed that there is an optimum standoff distance for which the impact pressure reaches a maximum value [9] that is proportional to the substrate damage [14].

Thus far, most studies that focus on the effect of standoff distance on damage formation are performed based on a macroscopic view. However, as a result of evolving technology, the final machining accuracy for jet machining or polishing has become achievable at a nano-scale. And the details of AWJ machining process are still difficult to obtain through experimentation or CFD simulations, especially at nanometer or atomic scales. Therefore, there is a gap in knowledge between macroscopic phenomena and nano-mechanism regarding the effect of standoff distance on damage formation. At present, molecular dynamics simulation (MD or MDS) has been applied to investigate impact processes and solid-liquid two-phase flows. Therefore, it is possible to provide a feasible scheme to close this gap.

Over the past three decades, extensive molecular dynamics simulations have been conducted to study the damage of substrates under the impact of clusters. The "piling-up" shock phenomenon that occurs during the process of Ar cluster impacting with a sodium chloride surface was investigated by Cleveland and Landman [15]. The relationship between the depth of the crater and the incident energy of the cluster was also studied by some researchers through MD simulation, based on the ion bombardment process [16–18]. Aoki and Matsuo performed simulations of Ar cluster impacting on sine-curved Si surfaces and found that the impact process of the cluster varied depending on the surface structure around the impact point [19]. Han and Gan studied the surface planarization of the rough

silicon surface under the impact of multiple nanoparticles [20]. Chen et al. studied the surface damage of the silicon surface covered by a water film [21] or silicon dioxide film [22] under silica cluster by MD simulations.

With respect to the process of solid-liquid two-phase flows, the impact and friction model [23] and the slip phenomenon [24] of Ar-Cu mixed-phase nanofluid between two Cu plates were investigated through MD simulation by Lv and Aminfar, respectively. In addition, Algara-Siller et al. studied the structural properties of water in confined spaces using MD [25]. Bourg and Steefel studied the solidification phenomenon and diffusion process of confined water by performing an MD simulation of water-filled silica nanopores [26]. These studies are helpful for studying the physical properties of water beneath an abrasive in the AWJ process.

In summary, most of the simulation reports on cluster-surface interactions were performed without the use of a water jet (namely the dry impact individually of the cluster). Meanwhile, few simulations were performed using solid-liquid two-phase flows under the conditions of a water jet. A molecular dynamics study of the collision process of an abrasive water jet on a substrate is supposed to provide an atomistic insight into the dynamics of AWJ processes. However, detailed reports on the atomic-scale mechanism that explain the influence of standoff distance on the damage of the substrate during AWJ process are very few in number.

In this study, the mechanism of the collision process between the silicon substrate and the water jet, which contains an amorphous silica cluster under different standoff distances, was studied by molecular dynamics simulation at the nano-scale. In addition, the influence of standoff distance on the damage of the silicon substrate would be analyzed through the variance of a five-fold coordination number of silicon atoms.

2 Simulation methodology

2.1 Simulation model

Figure 1 illustrates the simulation model of the impact of a jet, which is composed of a water column and a
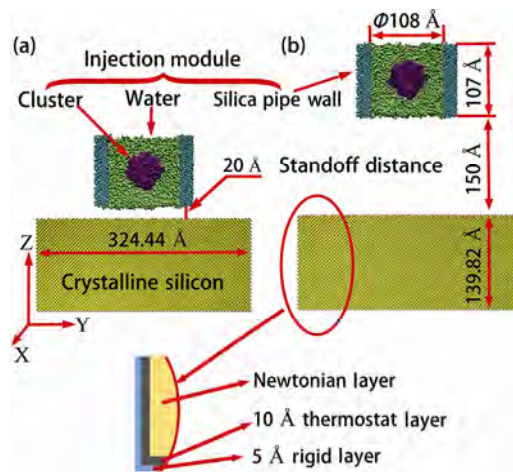
Fig. 1　Simulation model of an AWJ. (a) Standoff distance = 20 Å; (b) standoff distance = 150 Å.

cluster, toward a crystal silicon (*c*-Si) substrate. The Si (001) substrate contains approximately 499,200 atoms within a space of 215.84 Å×324.44 Å×139.82 Å. The outer layers (~5 Å thickness) of the substrate were fixed in space with the exception of the top contact surface. In addition, the thermostat layer (~10 Å thickness) was used to simulate the heat conduction in a reasonable way.

The injection module was composed of a silica cluster, a silica pipe wall, and a water column with a cavity. Firstly, the amorphous silica cluster and silica bulk were prepared by quenching melted beta-cristobalite from 5,000 K and 7,000 K to 293 K at a cooling rate of 10^{14} K/s, respectively [27]. The silica cluster consists of 5,184 atoms with a diameter of approximately 54 Å. Secondly, the atoms of a pipe diameter of 108 Å were removed from the center of the amorphous silica bulk, and then the amorphous silica pipe wall was prepared. The cluster surface and the inner surface of the silica pipe wall were composed of silicon atoms, bridging oxygen (BO) atoms bonded to two silicon atoms, and non-bridging oxygen (NBO) atoms bonded to one silicon atom. All NBO atoms were saturated with hydrogen atoms [28]. Thirdly, the silica cluster was placed in the cavity of the water column, whose diameter and length are 108 Å and 107 Å, respectively. Finally, the jet was placed into the pipe of the silica wall.

The interatomic interaction among the silica cluster and the silicon substrate system was modeled by a Stillinger-Weber-like potential [29], and the cutoff

distance of the interaction was 4.0 Å. The water was described by the TIP4P model [30]. The reaction field method was applied for the coulomb interactions between water molecules with a cutoff radius of 7.9 Å. The interactions between water and silicon substrate were described by an empirical Lennard-Jones potential model. The potential parameters were used and tabulated in Ref. [31], which provide further technical details. The cutoff distance for this Lennard-Jones interaction was 8.47 Å. Water molecules interacted with the silica atoms of the cluster and the pipe wall using the potential modeled according to Ref. [28], which consisted of Lennard-Jones and Coulomb interactions. And the pair interactions were truncated at a cutoff radius of 9 Å.

At the beginning of the simulation, the injection module was located at a standoff distance above the substrate surface. The simulation system was initiated with a temperature of 293 K. After a relaxation of 7,000 fs and a time step of 1 fs, the jet will impact the silicon substrate from the silica pipe with an initial impact velocity of 4,313 m/s under different standoff distances. Therefore, the impinging kinetic energy of the cluster under the simulation condition is almost same as that under the AWJ experimental condition [32]. In this study, the impact processes of the jet with different standoff distances of 20 Å, 30 Å, 40 Å, 50 Å, 75 Å, 100 Å, 125 Å and 150 Å were named Pos20, Pos30, Pos40, Pos50, Pos75, Pos100, Pos125 and Pos150, respectively. In order to study damage formation on the silicon substrate, the duration of the impact of the jet lasted for 8,000–15,000 fs. The larger the standoff distance, the longer the duration time. During the entire impact process, the atoms of the silica pipe wall were fixed. The temperature of the thermostat atoms of the silicon substrate was kept at 293 K by using Gaussian constraint thermostat method [33].

2.2　The calculation of local temperature and pressure

To calculate the local pressure and temperature of the ensemble, the section of the x-direction from 102 Å (Xmin) to 114 Å (Xmax) was chosen, as shown in Fig. 2. The silicon substrate and water film were divided by the grid of 12 Å × 12 Å × 12 Å and 12Å × 5 Å × 3.5 Å, respectively. In order to reduce the statistical error, each grid is partially overlapped, as shown in Fig. 2(a).
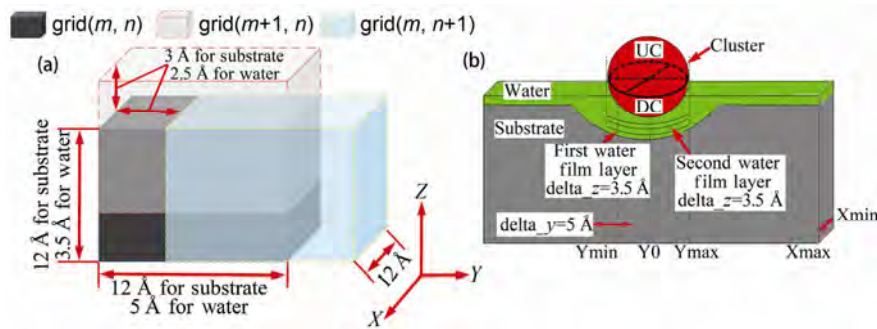
Fig. 2 (a) Calculation mode of local temperature and pressure of substrate or water film. (b) Calculation mode of density of water film layer and cluster force.

For the silicon substrate and the water film, each grid is separated in the *y* or *z* direction by 3 Å and 2.5 Å, respectively.

2.3 The calculation of water film layer density

In order to further study the variation in the density of the water film, the water on the substrate surface in the section is divided into several layers, as shown in Fig. 2(b). The *y* direction of each layer ranges from 135–190 Å. Starting from the silicon substrate surface, every delta_*z* = 3.5 Å is referred to as a layer. Then, each layer was divided into a number of grids by delta_*y* = 5 Å in the *y*-direction. Finally, the water density of each layer is obtained by averaging the water density of all grids in this layer.

2.4 The calculation of cluster force

The force between the cluster and the silicon substrate is defined as $\overrightarrow{F_{\text{C-S}}}$. In addition, the cluster was further divided into two hemispheres by the plane that passes through the cluster centroid and is parallel to the XOY plane, denoted as upper-cluster (UC) and down-cluster (DC), as shown in Fig. 2(b). Then, $\overrightarrow{F_{\text{UC-W}}}$ and $\overrightarrow{F_{\text{DC-W}}}$ represent the force from the water molecules on the UC and DC atoms, respectively. Obviously, a resultant force on the cluster F is the sum of $\overrightarrow{F_{\text{C-S}}}$, $\overrightarrow{F_{\text{UC-W}}}$ and $\overrightarrow{F_{\text{DC-W}}}$. In this study, the forces in the *z*-direction are our focus points.

3 Simulation results

As shown in Fig. 3, the deformation area will appear near the impact zone when the abrasive water jet impinged on the substrate. Meanwhile, the crystalline silicon will begin to amorphize in the deformation area due to large temperature and pressure gradients. That means that the single-crystal silicon atoms with a four-fold coordination number (CN4 atom) were converted into the atoms with three- and five-fold coordination number, respectively. They were referred to as the CN3 and CN5 atoms, respectively. According to previous studies [21, 34], it was found that the volume of the damaged region corresponds to the volume of the deformation region when the number of CN5 atoms reaches a maximum. Therefore, the variance in the number of CN5 atoms is selected as a quantitative criterion for judging the degree of damage incurred by the crystalline silicon. The higher the maxima of the number of CN5 atom (CN5max), the larger damage region.

Figure 4 shows that CN5max varies inconspicuously when the standoff distance ranges from 20–40 Å. When the standoff distance is more than 40 Å, CN5max decreases rapidly as the standoff distance increases. This is consistent with the variance in the damage severity of the substrate according to Fig. 3.

The above simulation shows that there is a critical value of the standoff distance (about 40 Å). When the standoff distance does not exceed the critical value, the substrate damage will inconspicuously change. Once the critical value is exceeded, the substrate damage will rapidly decrease. This phenomenon is consistent with the experimental conclusion that an optimal standoff distance exists in the AWJ experiment [8].
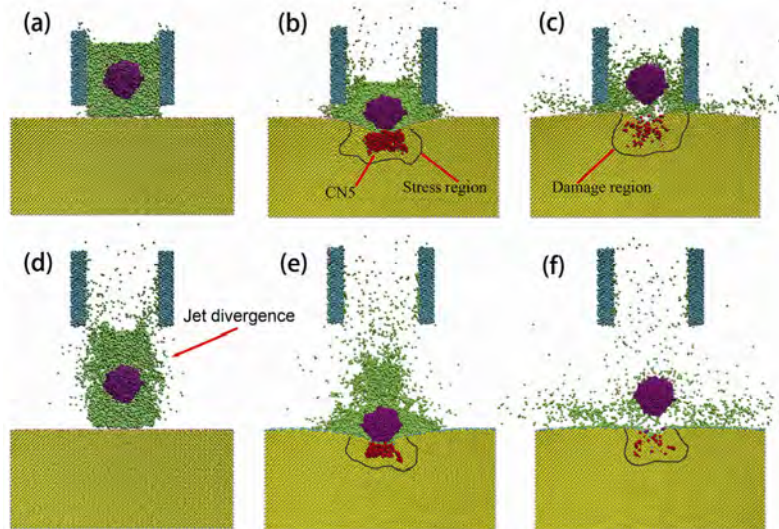
Fig. 3 Side cross-section view of the impact zone at different moments. Red particles represent CN5 atoms. (a), (b), (c) are the snapshots of 750 fs, 1,950 fs, and 6,000 fs at Pos20, respectively. (d), (e), (f) are the snapshots of 3,750 fs, 4,900 fs, and 8,000 fs at Pos150, respectively. (a) and (d) represent the moment when the jet first contacts the substrate; (b) and (e) represent the moment of the maximum of the number of CN5 atom; (c) and (f) represent the end of the impact process.
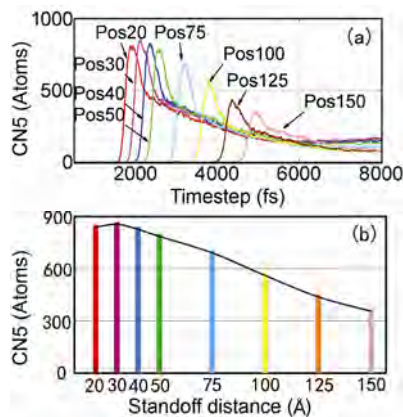

Fig. 4 (a) The CN5 variation curve with time during jet impingement on substrate with different standoff distances. In order to make figures clear, the data after 8,000 fs was not shown; (b) the CN5max variation curve with different standoff distances.

4 Analyses and discussions

The relationship between the standoff distance and the substrate damage was studied by analyzing the variance of CN5 number as follows. The jet process was divided into four stages.

4.1 The stage of solidification formation of the water film (Stage_I)

At the beginning of the simulation, the jet moves from the nozzle to the substrate at an initial velocity of 4,313 m/s. Then, the jet front will contact with the substrate first.

When the jet front reaches the substrate, it will form a water film on the substrate surface due to the impediment from substrate. With the impact proceeding, the density of this water film will exceed the value of density (1.0 g/cm^3) of water under the normal condition (Fig. 5), and continue to be higher. We refer to this process as "the water film solidifying phenomenon". At the same time, the cluster gradually approaches the solidified water film. Thus, the interaction between the cluster and the water film will begin to gradually appear (Fig. 6(a) at 750 fs, Fig. 6(b) at 3,750 fs). The period from the initial time of the simulation to the appearance of the interaction between the cluster and water film is called the stage of solidification formation of the water film (Stage_I).

On the other hand, when the water film is solidified, the local temperature and pressure of the substrate in the impact zone begin to increase as the impact energy of the jet increases (Fig. 7). Moreover, the impact energy of the substrate only stems from the action of the water because there is no interaction between the cluster and water film at this stage (Fig. 6).

For small standoff distances (from Pos20 to Pos40),

the shape and velocity distribution of the jet front does not change much compared to the starting time at the moment when the jet front contacts the substrate. On the contrary, when the standoff distance is over 40 Å, the shape (Figs. 3(a) and 3(d)) and velocity distribution of the jet front (Fig. 8) will be different from the starting time because of the weakness of the restriction of the nozzle. This phenomenon is called jet divergence. Obviously, the larger the standoff distance, the more serious the jet divergence will be.
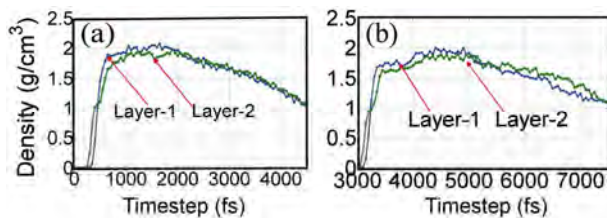

Fig. 5 The average density variation curve with time of the water film layer on the substrate surface: (a) Pos20; (b) Pos150.
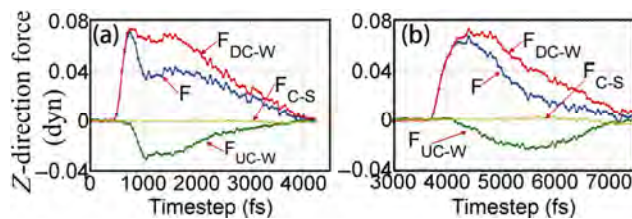

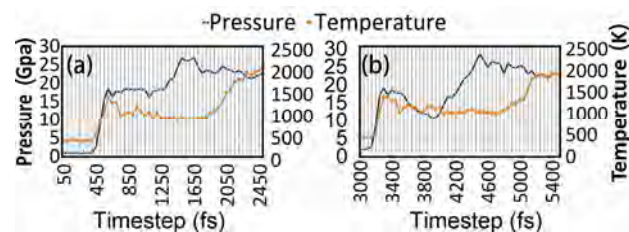**Fig. 6** Z-direction forces variation curve with time on cluster: (a) Pos20; (b) Pos150.

Fig. 7 The maximum pressure variation curve of the impact zone of the silicon substrate: (a) Pos20; (b) Pos150.
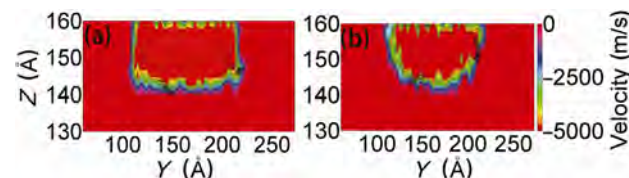

Fig. 8 The velocity distribution of the water in the z-axis direction when the jet first contacts with the substrate. (a) Pos20 at 750 fs; (b) Pos150 at 3,750 fs.

On the one hand, jet divergence has no effect on the velocity of the cluster, but will elongate the thickness of the water film, which is defined as the distance between the cluster and the silicon substrate. As shown in Fig. 9, this is not favorable to water film solidification. Therefore, the density of the solidified water film at Pos150 (1.6–1.75 g/cm^3) is significantly lower than that at Pos20 (1.75–1.9 g/cm^3) at the end of this stage. Meanwhile, the thickness of the solidifying water film (20 Å) in Pos150 is larger than Pos20 (17 Å), as shown in Figs. 9–11. In other words, the water film of Pos150, is relatively "loose" and "thick", compared to Pos20. This will result in a decrease in the energy transfer efficiency of the solidified water film, which is not favorable to the increase in the local pressure and temperature of the substrate due to the decreasing of input energy absorbed by the substrate.

On the other hand, because of the jet divergence, the time required for the solidification of the water film is prolonged. This means that the local pressure of the impact zone has more time to diffuse in the substrate, which is also not favorable to the increase in local pressure.

Because of the two reasons mentioned above, the local pressure of the impact zone of the substrate at Pos150 will increase firstly and then decrease (Fig. 7). The stress region (whose pressure is over 9 GPa on basis of the transformation pressure from Si-I to Si-II [35]) of Pos150 is larger than that of Pos20 at the end of the stage. However, the maximum pressure and high-pressure region (whose pressure is over 15 GPa) of the substrate at Pos150 are less than these at Pos20 (Figs. 12(a) and 13(a)). The high-pressure region was defined as the region of the local pressure over 15 Gpa because the distribution area of CN5 is in good
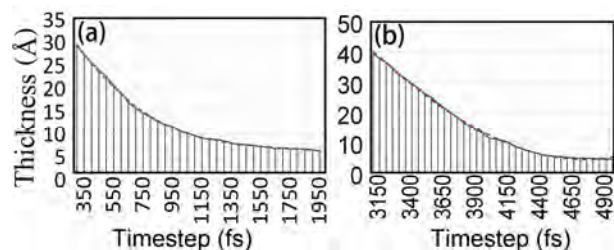
Fig. 9 The thickness variation curve with time of the water film confined between the cluster and the silicon substrate: (a) Pos20; (b) Pos150.
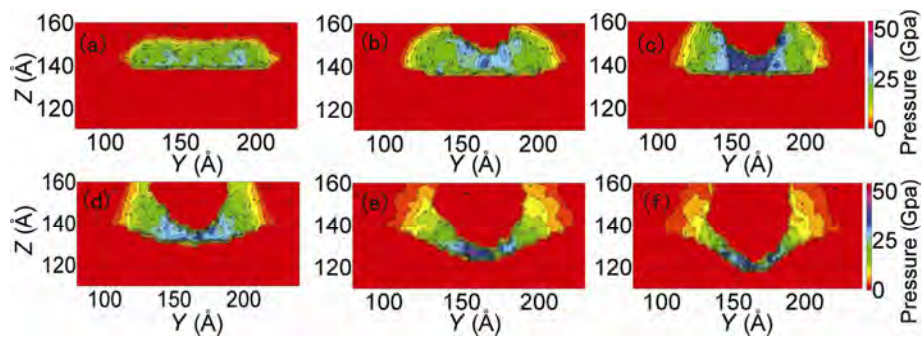
Fig. 10 Pressure distribution of water film confined at different moments under Pos20. Stage_I, Stage_II, and Stage_III range from 0–750 fs, 750–1,050 fs, and 1,050–1,950 fs, respectively. (a) 750 fs; (b) 900 fs; (c) 1,050 fs; (d) 1,300 fs; (e) 1,600 fs; (f) 1,950 fs.
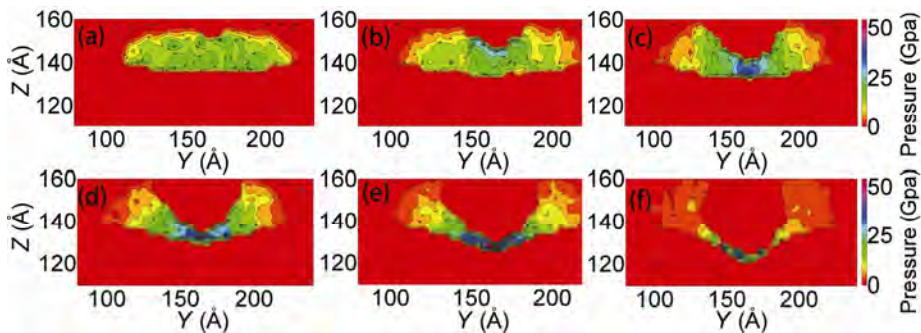
Fig. 11 Pressure distribution of water film confined at different moments under Pos150. Stage_I, Stage_II, and Stage_III range from 0–3,750 fs, 3,750–4,100 fs, and 4,100–4,900 fs, respectively. (a) 3,750 fs; (b) 3,900 fs; (c) 4,100 fs; (d) 4,300 fs; (e) 4,500 fs; (f) 4,900 fs.
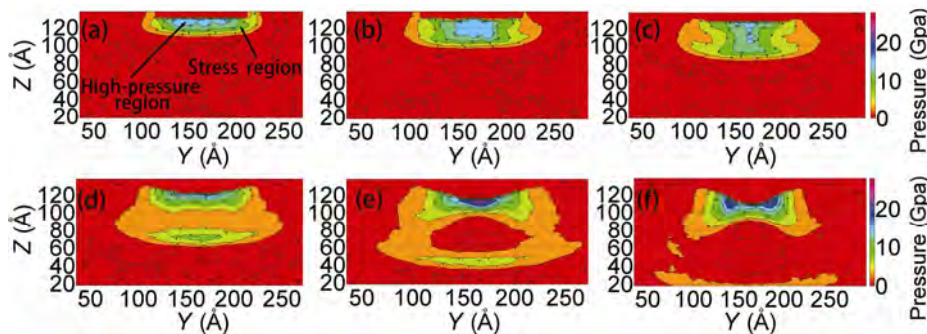
Fig. 12 Pressure distribution of silicon substrate at different moments under Pos20. (a) 750 fs; (b) 900 fs; (c) 1050 fs; (d) 1,300 fs; (e) 1,600 fs; (f) 1,950 fs.
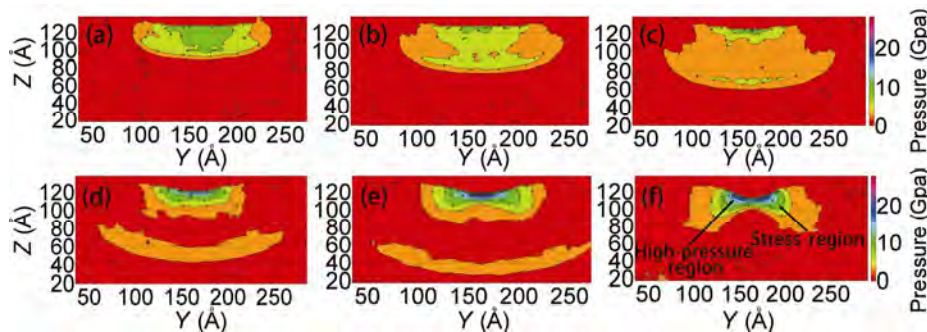
Fig. 13 Pressure distribution of silicon substrate at different moments under Pos150. (a) 3,750 fs; (b) 3,900 fs; (c) 4,100 fs; (d) 4,300 fs; (e) 4,500 fs; (f) 4,900 fs.

agreement with that of over 15 GPa pressure regions at the moment of CN5max (Figs. 2(b), 3(b), 12(f), and 13(f)). In this stage, the CN5 atom was not noticed in the impact zone of the substrate, as shown in Fig. 4.

4.2 The stage of complete solidification of the water film (Stage_II)

When the cluster begins to contact the solidified water film and then compress it, the force of the cluster in the z-direction (F_z) increases quickly from zero as the cluster moves downward (Fig. 6). Meanwhile, the thickness of solidified water film decreases (Fig. 9). Therefore, the density and the local pressure of the solidified water film increase further (Figs. 5, 10, and 11). When F_z reaches its maximum (F_{zmax}), the density and the local pressure reach their maximum values as well (Fig. 5), which means that the water film achieves a full degree of solidification. The period spreading from the appearance of F to the moment of F_{zmax} is called the stage of complete solidification of water film (Stage_II).

It is shown in Fig. 6 that there is no direct contact between the cluster and the substrate, and that the water film plays an intermediate role in the energy transfer from the cluster to the silicon substrate. That is to say, on the one hand, the water film solidification absorbs a part of the impact energy of the cluster; on the other hand, the remaining impact energy is transferred by the solidified water film to the silicon substrate. The high-pressure area of water film at Pos20 is evenly distributed in a larger hemispherical area below the cluster (Figs. 10(a)–10(c)) to incur the impact load of the jet. Therefore, the stress region at Pos20 at this stage rapidly increases because the impact energy of the cluster is evenly distributed over a larger area of the substrate. However, the high-pressure region of the substrate is slightly decreased (Figs. 12(a)–12(c)).

In contrast with Pos20, the high-pressure area of the water film at Pos150 starts concentrating to a relatively small area just below the cluster, which is "thick" and "loose" (Figs. 11(a)–11(c)). Therefore, the majority of the input energy of the cluster is used to achieve complete solidification of the water film, and a very small part is transferred into the silicon substrate through the water film in this stage. Therefore, the

maximum pressure and the stress region of the substrate reduce gradually. In addition, the high-pressure region diminishes or disappears (Figs. 13(a)–13(c)).

Therefore, the maximum pressure and the high-pressure region of the silicon substrate in Pos20 continues to be larger than those in Pos150. Moreover, the stress region of the former is also significantly larger than that of the latter.

4.3 The stage of maintaining complete solidification of the water film (Stage_III)

The cluster continues to move down after the water film is completely solidified. The period from the moment of F_{zmax} to the moment of CN5max is called the stage of maintaining complete solidification of the water film (Stage_III), because the density of the solidification film experiences only a small change during this stage (Fig. 5).

At this stage, the input energy of the cluster and the water is mainly divided into two parts: (1) one part overcomes the resistance of the solidification water film in order to reduce the thickness of the solidification film (E1); (2) another part transfers into the silicon substrate by the solidifying water film (E2).

For the standoff distance at Pos20, E1 is larger than E2 (E1>E2) during the early period of this stage. Therefore, the area where the solidifying water film is sustaining the load of the jet is relatively large (Figs. 10(c) and 10(d)). In addition, the stress wave will split at the stress region of the substrate because E2 is not sufficient. Therefore, the stress region of the substrate will decrease significantly. However, the high-pressure region of the substrate gradually increases, and the maximum pressure of the substrate cannot increase (Figs. 12(c) and 12(d)).

With the continuous embedding of the cluster, the area where the solidifying water film is sustaining the load of the jet becomes more and more concentrated under the cluster (Figs. 10(d) and 10(e)). This causes E1 to gradually become equal to E2, even smaller than E2. Therefore, the stress region of the silicon substrate slowly increases again in the period of E1 $\leqslant$ E2 (as Figs. 12(d) and 12(e)), but the high-pressure region and the maximum pressure significantly increased.

For Pos150, the area where the solidifying water

film sustains the load of the jet has concentrated under the cluster during the early period of this stage (Figs. 11(c)−11(e)). Therefore, it directly enters the period of E1≤E2. As a result, the local pressure of the stress region of substrate increases rapidly and the high-pressure region appears again and gradually increases (Figs. 13(c)−13(e)). However, the stress region and high-pressure region at Pos150 are still significantly lower than those at pos20 when the CN5 atom appears.

When the maximum pressure of the substrate exceeds the threshold value for the transition between the CN4 atom and the CN5 atom, CN5 atoms will appear and the cluster does not continue to be embedded in the substrate. As shown in Fig. 9, Pos20 and Pos150 are stable at approximately 7 Å and 4.5–5 Å, respectively. This means that E1 is much smaller than E2 during this period (E1<<E2). It is noticed that the maximum pressure of the substrate will slightly reduce first, and will then experience only a minor change whether the standoff distance is Pos20 or Pos150. In addition, the areas of the stress region and high-pressure region increase very slowly after CN5 appears (Figs. 12(e), 12(f), 13(e), and 13(f)).

Under continuous impact energy, the number of CN5 atoms rapidly increases to a maximum at 1,950 fs (Pos20) and 4,900 fs (Pos150), respectively. Therefore, the period from when the CN5 atom appears to the moment when the maximum number of CN5 atoms is obtained in Pos20 is as same as that in Pos150 (Fig. 4(a)).

Meanwhile, there is no obvious difference in the local pressure and temperature maximum of the impact zone between Pos20 and Pos150 at the moment of CN5max.

Therefore, CN5max of Pos20 is significantly larger than that of Pos150 because the areas of the stress region and high-pressure region of the former are greater than those of the latter.

4.4 The stage of degradation of the complete solidified water film (Stage_IV)

As the velocities of the cluster and the water behind the cluster further decrease, the density of the solidifying water film begins to decrease (Fig. 5). This process is known as the degradation phenomenon of

the solidified water film (Stage_IV). This will result in a decrease in the transfer-efficiency of the water film, which leads to a reduction in the energy absorbed by the silicon substrate. As a result, the local pressure of the substrate in the impact zone will decrease. In addition, the local temperature of the substrate will rise due to the gradual weakening of the restriction from the densifying water film. Therefore, the number of CN5 atom decreases rapidly (Fig. 4). Finally, the substrate enters a state of slow relaxation with the rebounding of the jet. The substrate damage gradually formed and held stable, along with the mutual transformation between CN5, CN3, and CN4.

4.5 Discussions

The formation of damage is in accordance with the variance in the number of CN5 atoms in the impact zone of the silicon substrate during the water jet process. The factors that influence the formation of the damage are listed as follows: (1) the stress and high-pressure regions at the moment of CN5max; (2) the maximum of local pressure and local temperature at the moment of CN5max; (3) the duration from the moment of the appearance of CN5 atom to the moment of CN5max. However, no significant difference was observed for the latter two factors under different standoff distances with the same impact velocity. Therefore, the influence of standoff distance on the degree of damage incurred by the substrate is mostly contributed by the first factor.

As shown in Fig. 14, the solidification of the jet front will occur under the impact of the water jet during the water film solidification stage. However, as the standoff distance increases, the water jet will diverge gradually. Therefore, the solidifying water film formed by a small distance is relatively "dense" and "thin", while the solidifying water film formed by large distance is relative "loose" and "thick". As a consequence, the jet front will spend more time solidifying at large distances, which results in a longer diffusion time for the stress region of the substrate. Therefore, at the end of this stage, the area of the stress region at small distance is smaller than that at large distance, but the area of the high-pressure region of the former is larger than that of the latter.

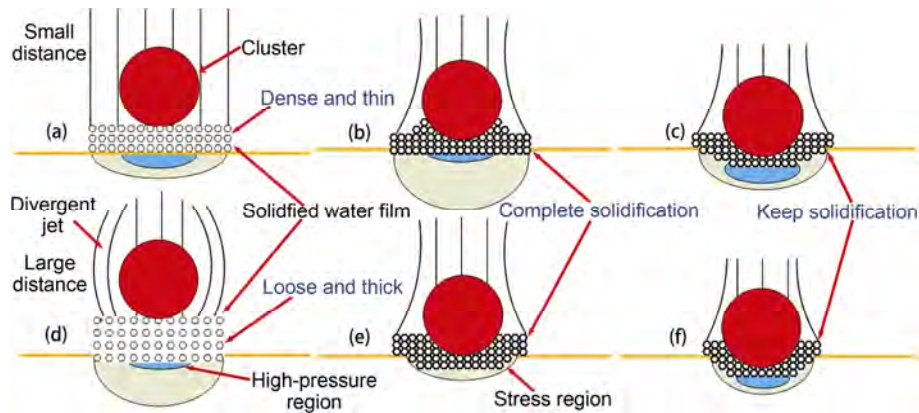The cluster begins to compress the water film during

Fig. 14 Sketch of the process of AWJ impingement on substrate. (a), (b), and (c) are at small standoff distance; (d), (e), and (f) are at large standoff distance. (a), (d) represent the moment that the water film starts to solidify; (b), (e) represent the moment of the water film complete solidification; (c), (f) represent the moment that substrate reaches maximum damage.

the stage of complete solidification of the water film. Firstly, most of the input energy of the cluster is used for realizing the complete solidification of the water film. Secondly, the remains are transferred to the silicon substrate by the solidification film. As the standoff distance increases, the energy absorbed by the substrate becomes smaller and smaller. For small standoff distances, the impact energy of the cluster could be absorbed by a larger area of the substrate because the solidifying water film is denser. This can make the stress region increase rapidly, but is not enough to maintain the high-pressure region. Therefore, the high-pressure region decreases. For large standoff distances, both stress region and high-pressure region reduced significantly. And the high-pressure will even disappear. Therefore, at the end of this stage, both the area of stress region and high-pressure region at small distances are significantly larger than those at large distances.

At the stage of maintaining complete solidification of water film, the relationship between E1 and E2 usually goes through three periods: E1>E2, E1≤E2 and E1<< E2.

In the period of E1>E2 and E1≤E2, the cluster is continuously embedded in the water film. For a small standoff distance, the stress region will first decrease clearly and then increase slowly again because of the occurrence of the split of the stress wave. Meanwhile, the high-pressure region of substrate will increase further. For a large standoff distance, both the stress region and high-pressure region will increase clearly

again. However, at the end of E1≤E2 period, the stress region and the high-pressure region at large distances are still significantly less than that at small distances.

In the period of E1<<E2, the cluster cannot be embedded in the solidified water film. In addition, CN5 atoms begin to appear and increase rapidly until its maximum. In this period, both the stress region and high-pressure region do not change substantially, as the input energy is consumed by the generation of the substrate CN5.

There was no significant difference in the duration of E1<<E2 period between different distances. In addition, there is no obvious difference in the local pressure and temperature maximum of the impact zone between different distances at the moment of CN5max.

Therefore, it is the differences in the stress region and the high-pressure region that result in the reduction of the CN5 production rate at increasing distances. This eventually causes the CN5max of the small distance significantly greater than that at large distances.

5 Conclusions

In summary, the process of an abrasive water jet impinging on monocrystalline silicon substrate under different standoff distances was studied by molecular dynamics simulation. The influence of standoff distance on the damage of the crystal silicon substrate was

studied by analyzing the variation of the CN5 atoms of the silicon substrate. The impact process before the CN5 atoms reach their maximum number is divided into three stages: solidification formation of water film, complete solidification of water film, and maintaining complete solidification of water film.

During the solidification formation stage, due to jet divergence, the solidified water film is relatively "thinner" and "denser" under the smaller standoff distance, and the forming time is short. On the contrary, under the larger standoff distance, the solidified water film is relatively "thicker" and "looser" with a longer formation time. Therefore, the stress region under the smaller distance is less than that of the larger distance. However, the high-pressure region of the former is larger than that of the latter.

At the stage of complete solidification, the "thicker" and "looser" water film will consume more input energy of the cluster to realize complete solidification. Therefore, the high-pressure region of small standoff distance continues to be larger than that of the large standoff distance, although both high-pressure regions are reduced at this stage. More importantly, the stress region of the former also begins to be significantly larger than the latter.

In the stage where complete solidification is maintained, the high-pressure region and the stress region of small distance are still far larger than those of large distance. These differences finally lead to CN5max and the damage degree of the substrate will first exhibit a small change and then decrease quickly with the increase in standoff distance. This phenomenon is consistent with the existence of an optimal standoff distance in the AWJ experiment.

In a word, at a nano-scale, jet divergence will affect the process of solidification of the water film between the cluster and the substrate under different standoff distances. This will change the energy transfer efficiency from the input jet to the impacted substrate. Therefore, the occurrence and maintenance of the complete solidification plays a decisive role in the damage formation of the silicon substrate. These findings are expected to be helpful for thoroughly understanding the material removal mechanism during AWJ or MJP process.

Acknowledgements

References

[1] Hashish M. Visualization of the abrasive-waterjet cutting process. *Exp Mech* **28**(2): 159–169 (1988)

[2] Guha A, Barron R M, Balachandar R. An experimental and numerical study of water jet cleaning process. *J Mater Process Technol* **211**(4): 610–618 (2010)

[3] Fähnle O W, Brug H V, Frankena H J. Fluid jet polishing of optical surface. *Appl Opt* **37**: 6771–6773 (1998)

[4] Horiuchi O, Ikeno J, Shibutani H, Suzuki H, Mizukami Y. Nano-abrasion machining of brittle materials and its application to corrective figuring. *Precision Engineering* **31**: 47–54 (2007)

[5] Loc P H. Investigation of optimal air-driving fluid jet polishing parameters for the surface finish of N-BK7 optical glass. *J Manuf Sci Eng* **135**(1): 228–229 (2013)

[6] Srinivasu D S, Axinte D A, Shipway P H, Folkes J. Influence of kinematic operating parameters on kerf geometry in abrasive waterjet machining of silicon carbide ceramics. *Int J Mach Tool Manu* **49**(14): 1077–1088 (2009)

[7] Hashish M, Plessis M P D. Prediction equations relating high velocity jet cutting performance to stand off distance and multipasses. *J Manuf Sci Eng* **101**(3): 311–318 (1979)

[8] Anglani F, Barry J, Dekkers W, Khare S. CFD modelling of a water-jet cleaning process for concentrated solar thermal

(CST) systems. In *Proceedings of third Southern African Solar Energy Conference*, University of Pretoria, South Africa, 2015: 389–394

[9] He Z G, Li G S, Wang H Z. Shen Z G, Tian S C, Lu P Q, Guo B. Numerical simulation of the abrasive supercritical carbon dioxide jet: The flow field and the influencing factors. *J Hydrodyn* **28**(2): 238–246 (2016)

[10] Kordonski W, Shorey A B. New magnetically assisted finishing method: material removal with magnetorheological fluid jet. *Proc SPIE* **5180**: 107–114 (2004)

[11] Karakurt I, Aydin G, Aydiner K. An Experimental Study on the Depth of Cut of Granite in Abrasive Waterjet Cutting. *Mater Manuf Process* **27**(5): 538–544 (2012)

[12] Zhang X C, Dai Y F, Li S Y, Peng X Q. Effect on material removal of magnetorheological jet polishing by several parameters. *Opt Precision Eng* **14**(6): 1004–1008 (2006)

[13] Liu H, Wang J, Kelson N, Brown R J. A study of abrasive waterjet characteristics by CFD simulation. *J Mater Process Technol* **153**(1): 488–493 (2004)

[14] Momber A W, Kovacevic R. *Principles of Abrasive Water Jet Machining*. London (UK): Springer London, 1998

[15] Cleveland C L, Landman U. Dynamics of cluster-surface collisions. *Science* **257**(5068): 355–361 (1992)

[16] Henkel M, Urbassek H M. Ta cluster bombardment of graphite: molecular dynamics study of penetration and damage. *Nucl Instrum Methods Phys Res* **145**(4): 503–508 (1998)

[17] Insepov Z, Manory Z, Matsuo J, Yamada I. Proposal for a hardness measurement technique without indentor by gas-cluster-beam bombardment. *Phys Rev B* **61**(13): 8744–8752 (2000)

[18] Yamaguchi Y, Gspann J. Large-scale molecular dynamics simulations of cluster impact and erosion processes on a diamond surface. Phys Rev B 66(15): 155408 (2002)

[19] Aokia T, Matsuo J. Surface structure dependence of impact processes of gas cluster ions. *Nucl Instrum Methods Phys Res* **216:** 185–190 (2004)

[20] Han X, Gan Y X. Analysis the complex interaction among flexible nanoparticles and materials surface in the mechanical polishing process. *Appl Surf Sci* **257**(8): 3363–3373 (2011)

[21] Chen R L, Liang M, Luo J B, Lei H, Hu X. Comparison of surface damage under the dry and wet impact: Molecular dynamics simulation. *Appl Surf Sci* **258**(5): 1756–1761 (2011)

[22] Chen R L, Wu Y H, Lei H, Jiang R R, Liang M. Study of material removal processes of the crystal silicon substrate

covered by an oxide film under a silica cluster impact: Molecular dynamics simulation. *Appl Surf Sci* **305**(16): 609–616 (2014)

[23] Lv J, Bai M, Cui W, Li X. The molecular dynamic simulation on impact and friction characters of nanofluids with many nanoparticles system. *Nanoscale Res Lett* **6**(1): 1–8 (2011)

[24] Aminfar H, Razmara N, Mohammadpourfard M. On flow characteristics of liquid-solid mixed-phase nanofluid inside nanochannels. *J Appl Math Mech* **35**(12): 1541–1554 (2014)

[25] Algara-Siller G, Lehtinen O, Wang F C, Nair R R, Kaiser U, Wu H A, Geim A K, Grigorieva I V. Square ice in graphene nanocapillaries. *Nature* **519**(7544): 443–5 (2014)

[26] Bourg I C, Steefel C I. Molecular dynamics simulations of water structure and diffusion in silica nanopores. *J Phys Chem C* **116**(21): 11556–11564 (2012)

[27] Vollmayr K, Kob W, Binder K. Cooling-rate effects in amorphous silica: a computer- simulation study. *Phys Rev B* **54**(22): 15808–15827 (1996)

[28] Rovere M, Ricci M A, Vellati D, Bruni F. A molecular dynamics simulation of water confined in a cylindrical SiO2 pore. *J Chem Phys* **108**(23): 9859–9867 (1998)

[29] Watanabe T, Fujiwara H, Noguchi H, Hoshino T, Ohdomari I. Novel interatomic potential energy function for Si, O mixed systems. *Jpn J Appl Phys* **38**(38): 366–369 (1999)

[30] Jorgensen W J, Chandrasekhar J, Madura J D, Impey R W, Klein M L. Comparison of simple potential functions for simulating liquid water. *J Chem Phys* **79**(2): 926–935 (1983)

[31] Tang C Y, Zhang L C. A molecular dynamics analysis of the mechanical effect of water on the deformation of silicon monocrystals subjected to nano-indentation. *Nanotechnology* **16**(1): 15–20 (2005)

[32] Xu J, Luo J B, Lu X C, Wang L L, Pan G S, Wen S Z. Atomic scale deformation in the solid surface induced by nanoparticle impacts. *Nanotechnology* **16**(6): 859–864 (2005)

[33] Evans D J, Hoover W G, Failor B H, Moran B, Ladd A J C. Nonequilibrium molecular dynamics via Gauss's principle of least constraint. *Phys Rev A* **28**(2): 1016–1021 (1983)

[34] Chen R L, Luo J B, Guo D, Lei H. Dynamic phase transformation of crystalline silicon under the dry and wet impact studied by molecular dynamics simulation. *J Appl Phys* **108**(108): 073521 (2010)

[35] Hu J Z, Merkle L D, Menoni C S, Spain I L. Crystal data for high-pressure phases of silicon. *Phys Rev B* **34**(7): 4679–4684 (1986)

Ruling CHEN. He received his Ph.D. degree in mechanical engineering from the Tsinghua University in China in 2009. Now he is an associate professor at Donghua University. His research areas cover the nanotribology, ultra-precision surface machining/etc.

Di ZHANG. Master student in inorganic chemistry major at the Shanghai University. His research interest is molecular dynamics simulation and ultra-precision surface machining.

RESEARCH ARTICLE

Tribological evaluation of environmentally friendly ionic liquids derived from renewable biomaterials

Cheng JIANG[1,2]**, Weimin LI**[1,2]**, Jingyan NIAN**[1]**, Wenjing LOU**[1,2,*]**, Xiaobo WANG**[1,2]

[1] *State Key Laboratory of Solid Lubrication, Lanzhou Institute of Chemical Physics, Chinese Academy of Sciences, Lanzhou 730000, China*

[2] *Qingdao Center of Resource Chemistry & New Materials, Qingdao 266100, China*

Abstract: Unlike most of the conventional ionic liquids (ILs) derived from non-renewable resources, five environmentally friendly ILs ([Ch][AA] ILs) derived from amino acids (AAs) and choline (Ch) were synthesized using biomaterials by a simple, green route: acid–base reaction of Ch and AAs. The thermal and corrosion properties, as well as viscosity, of the prepared ILs were examined. The results revealed that the anion structure of ILs plays a dominant role in their thermal and viscosity behavior. These ILs exhibited less corrosion toward copper, related to their halogen-, sulfur-, and phosphorus-free characteristics. The tribological behavior of the synthesized ILs was examined using a Schwingungs Reibung und Verschleiss tester, and the results indicated that these ILs exhibit good friction-reducing and anti-wear properties as lubricants for steel/steel contact. Results from energy-dispersive spectroscopy and X-ray photoelectron spectroscopy indicated that the good tribological properties of [Ch][AA] ILs are related to the formation of a physically adsorbed film on the metal surface during friction.

1 Introduction

Currently, toxicity, safety, and environmental compatibility of lubricants are attracting increasing attention as almost half of the lubricants are estimated to eventually enter the environment by evaporation, leakages, or spills, leading to adverse negative effects on the environment and ecosystem [1, 2]. Therefore, environmentally friendly lubricants have attracted extensive attention, and a considerable number of studies have been conducted in this field [3−8]. Generally, environmentally friendly lubricants are divided into two categories according to their raw material sources. The primary environmentally friendly lubricants are derived from nature resources and are utilized in the modern industry, e.g., natural vegetable oils [9], chemically modified vegetable oils [7, 8], genetically modified vegetable oils, and synthetic

lubricants derived from biomaterials [10−12]. On the other hand, petrochemical-derived lubricants with good biodegradability are considered as the second type of environmentally friendly lubricants, e.g., synthetic esters, polyether, and low-viscosity polyalphaolefins [1]. Among these environmentally friendly lubricants, synthetic lubricants derived from natural resources have attracted extensive scientific attention because of their flexible molecular structures, controllable performance, and renewable features, and recently, various biomaterials have been used as raw materials to develop environmentally benign lubricants [10−12].

Ionic liquids (ILs), which are solely composed of ions, are salts that are liquids with a melting point of around or less than 100 °C [13]. In the past two decades, ILs have attracted extensive attention in sustainable chemistry and industrial applications because of their low flammability, low vapor pressure, excellent thermal

---

stability, and high ionic conductivity [14–16]. Moreover, ILs exhibit excellent tribological performance because of the tribochemical reaction between the frictional pairs. In 2001, Liu and coworkers were the first to report alkylimidazolium ILs as lubricants with excellent friction-reducing and anti-wear properties [17]. Since their report, ILs have been extensively investigated as lubricants and lubricant additives [18, 19]. However, most of the conventional ILs reported typically contain tetrafluoroborate (BF_4^-), hexafluorophosphate (PF_6^-), and bis(trifluoromethylsulfonyl)imide ($TFSI^-$) anions. Halogen-containing ILs are more prone to reaction with water, generating haloid acid; haloid acid can cause severe metal corrosion and environmental pollution [20, 21]; the same issues are also observed for sulfur- and phosphorus-containing ILs [22]. Therefore, in view of environmental protection, it is crucial to develop halogen-, sulfur-, and phosphorus-free ILs. Recently, some exploratory studies have been reported. Aspartic-acid- and glutamic-acid-derived ammonium-cation-based ILs have been reported as efficient anti-wear and friction-reducing additives for mineral base oil [23]. Song et al. have prepared tetrabutylammonium-based amino acid ILs and reported excellent tribological performance for steel/steel, steel/copper, and steel/aluminum contacts [24].

Choline (Ch), a water-soluble nutrient, is an important component of lecithin and sphingomyelin, and it is typically categorized as a B-complex vitamin. Ch is a promising candidate as the cation for ILs, and some choline-based ILs have been reported to exhibit low toxicity and facile biodegradability [25]. On the other hand, amino acids (AAs) are common cost-effective biomaterials, which are abundant in nature and readily available in bulk. [Ch][AA] ILs were prepared with Ch and AAs by a simple method. Different from conventional ILs containing halogen-, sulfur-, and phosphorus in their molecules, [Ch][AA] ILs have been reported to be environmentally friendly, sustainable, non-toxic, and biodegradable materials [26, 27]. Several studies have reported the preparation of novel [Ch][AA] ILs, and their potential applications in various fields have been investigated [28, 29]. Recently, Mu and coworkers have reported lignin-[Ch][AA] ILs as non-corrosive green lubricants [30]. Nevertheless, to the best of our knowledge, few systematic studies on the

structure and properties of Ch-based ionic liquids as environmentally friendly lubricants have been reported.

In this study, five [Ch][AA] ILs were designed and synthesized with an identical cation (choline), but different anions (i.e., AAs), by a green route with only water as the by-product. The effects of anion symmetry and alkyl chain length on the viscosity, thermal stability, corrosion, and tribological properties of [Ch][AA] ILs were examined. In addition, the tribological mechanism of the green ILs was discussed on the basis of energy-dispersive spectroscopy (EDS) and XPS results.

2 Experimental method

2.1 Materials

Choline hydroxide (48–50 wt% in water, Tokyo Chemical Industry Co., Ltd.) was used as received. L-glycine (>99 wt%), L-alanine (>98 wt%), L-isoleucine (>98 wt%), L-phenylalanine (>98 wt%), and L-serine (98 wt%) were purchased from Sinopharm Chemical Reagent Co., Ltd., and used without further treatment. A conventional halogen-containing IL, e.g., 1-hexyl-3-methylimidazolium bis(trifluoromethylsulfonyl)imide ($[C_6mim][NTf_2]$), was prepared according to a previously reported method and used for the comparison of the tribological properties [31].

2.2 Synthesis of [Ch][AA] ILs

Figure 1 shows the synthetic route of [Ch][AA] ILs according to a previously reported method [32]. First, 0.1 mol AAs (e.g., 7.58 g L-glycine, 9.09 g L-alanine, 13.38 g L-isoleucine, 16.86 g L-phenylalanine, and 10.72 g L-serine) were dissolved in 30 mL of water, and then choline hydroxide (24.7 g, 0.1 mol) was added dropwise into the AA solution with stirring. Second, the AA was neutralized using an equimolar choline hydroxide aqueous solution by stirring at room temperature for 18 h. Water was then evaporated under
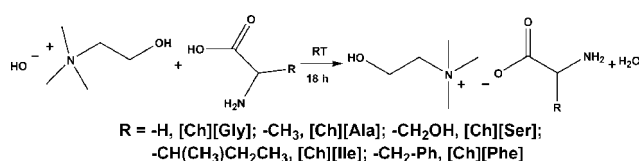

R = -H, [Ch][Gly]; -CH₃, [Ch][Ala]; -CH₂OH, [Ch][Ser]; -CH(CH₃)CH₂CH₃, [Ch][Ile]; -CH₂-Ph, [Ch][Phe]

Fig. 1 General synthetic route for [Ch][AA] ILs.

vacuum at 65 ℃, and excess AAs were precipitated using methanol. Next, the prepared choline glycine ([Ch][Gly]), choline alanine ([Ch][Ala]), choline isoleucine ([Ch][Ile]), choline phenylalanine ([Ch][Phe]), and choline serine ([Ch][Ser]) ILs were dried at 65 ℃ under vacuum for 24 h. The data for the [Ch][AA] IL structures confirmed by proton nuclear magnetic resonance (^{1}H NMR) spectroscopy are reported below:

[Ch][Gly]: δ: 3.15 (2H, s, CH_2NH$_2$), 3.17 (9H, s, N(CH_3)$_3$), 3.48–3.50 (2H, m, CH$_2$CH_2OH), 4.01–4.05 (2H, m, CH$_2$CH_2N).

[Ch][Ala]: δ: 1.19–1.21 (3H, d, CH_3CH), 3.17 (9H, s, N(CH_3)$_3$), 3.27–3.32 (1H, q, CHNH$_2$), 3.47–3.50 (2H, m, CH$_2$CH_2OH), and 4.01–4.05 (2H, m, CH$_2$CH_2N).

[Ch][Ser]: δ: 3.18 (9H, s, N(CH_3)$_3$), 3.31–3.34 (1H, m, CHNH$_2$), 3.49–3.51 (2H, t, CH$_2$CH_2OH), 3.65–3.74 (2H, m, CHCH_2OH), 4.02–4.06 (2H, m, CH$_2$CH_2N).

[Ch][Ile]: δ: 0.83–0.88 (3H, t, CH_3CH$_2$, 3H, d, CHCH_3, overlap), 1.10–1.15 (1H, m, CH_2CH$_3$), 1.35–1.37 (1H, m, CH_2CH$_3$), 1.61–1.64 (1H, m, CHCH$_3$), 3.06 (1H, d, CHNH$_2$), 3.17 (9H, s, N(CH_3)$_3$), 3.47–3.49 (2H, t, CH$_2$CH_2OH), 4.00–4.04 (2H, m, CH_2OH).

[Ch][Phe]: δ: 2.81–2.86 (1H, m, C$_6$H$_5$CH_2), 2.96–3.00 (1H, m, C$_6$H$_5$CH_2), 3.14 (9H, s, N(CH_3)$_3$), 3.47 (2H, m, CHCH_2OH), 3.88–4.04 (2H, m, CH$_2$CH_2N), 7.25–7.36 (5H, m, C$_6H_5$CH$_2$).

2.3 Characterization of [Ch][AA] ILs

Before characterization, all of the [Ch][AA] ILs were dried under vacuum at 65 ℃ for 48 h. The structures of [Ch][AA] ILs were confirmed by ^{1}H NMR (400 MHz) spectroscopy. Differential scanning calorimetry (DSC 200F3, Netzsch) was employed to record the glass transition temperatures (T_g). First, samples were heated to 120 ℃ to evaporate the solvent from the ILs, cooled to −100 ℃ with liquid nitrogen, and finally heated to 100 ℃ at a rate of 10 ℃·min^{-1}. The decomposition temperatures (T_d) of the samples were recorded on an STA449F3 instrument (TGA, Netzsch) at a heating rate of 10 ℃·min^{-1} under nitrogen. An SYP1003-III kinematic viscosity tester was used to measure the kinematic viscosity of the prepared ILs at 40 and 100 ℃.

2.4 Copper strip corrosion test

The copper strips used in this experiment were 10 mm in length, 10 mm in width, and 3 mm in thickness. Before corrosion tests, all of the copper strips were polished using an abrasive paper, followed by cleaning by ultrasonication in acetone for 10 min. The samples were immersed in the IL solutions and heated at 100 ℃ for 72 h. After the test, the copper strips were washed with acetone, and the corrosion level was confirmed according to the corrosion standard tint board.

2.5 Tribological tests

The friction and wear tests were carried out using an Optimol SRV-IV oscillating reciprocating friction and wear tester. The upper ball with a diameter of 10 mm was composed of AISI 52100 steel (hardness of approximately 59–61 HRC). The upper ball reciprocally slides against the lower stationary discs (Φ 24 mm × 7.9 mm) at an amplitude of 1 mm. The lower stationary discs were composed of AISI 52100 steel, with a hardness of approximately 61–64 HRC. All tests were conducted at 20 ℃ for 30 min at a frequency of 25 Hz, a load of 100 N, and a relative humidity of 30%–40%. The volume loss of the lower disc was measured using a MicroXAM-3D non-contact surface mapping microscope profilometer. Scanning electron microscopy (SEM) and EDS analysis images were recorded on an SEM instrument (JSM-5600LV, JEOL). The chemical composition of the wear scars was confirmed by X-ray photoelectron spectroscopy (XPS), and XPS profiles were recorded on a PHI-5702 electron spectrometer (Perkin-Elmer, USA). Before SEM and XPS analysis, the lower discs were cleaned by ultrasonication in acetone for 20 min to remove the residual lubricants on the surface.

3 Result and discussion

3.1 Thermal analysis

Figure 2(a) shows the DSC curves of the prepared ILs, and Table 1 summarizes the T_g of the ILs. As can be observed in Fig. 2(a), all five ILs do not exhibit melting temperatures in the range of the measured temperature, and their T_g values ranged between −62.2 and −48.2 ℃. [Ch][Gly] exhibited the lowest T_g of −62.2 ℃. With the increase in the anion size (from glycine, alanine,
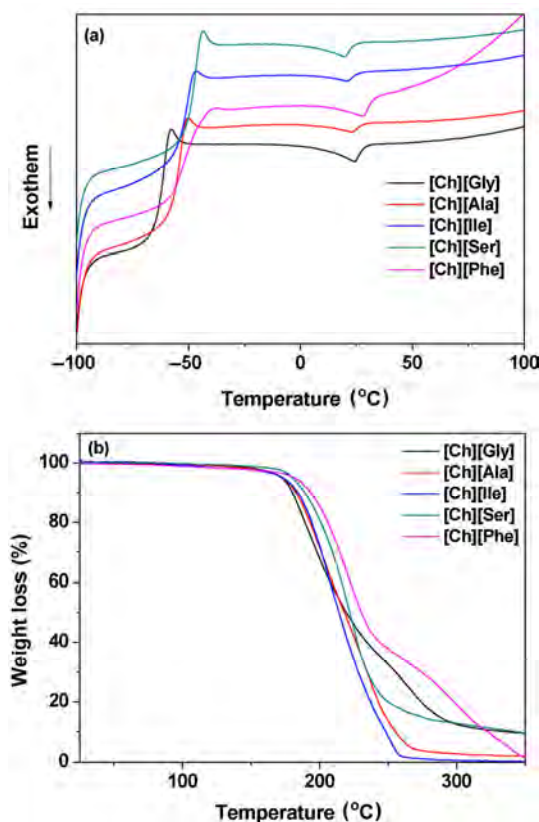
Fig. 2 DSC (a) and TG (b) curves of [Ch][AA] ILs.

Table 1 Physical properties of [Ch][AA] ILs.

ILs	Kinematic viscosity (mm²/s)		Viscosity Index	T_g (°C)	T_d (°C)
	40 °C	100 °C			
[Ch][Gly]	330.10	28.70	118	−62.2	173.8
[Ch][Ala]	385.18	26.45	92	−54.9	179.6
[Ch][Ser]	475.76	30.05	91	−48.2	186.6
[Ch][Ile]	1742.78	68.17	92	−52.0	183.6
[Ch][Phe]	2641.96	65.10	57	−50.5	195.0

and isoleucine to phenylalanine anions) of the ILs, the T_g increased. For [Ch][Ser], the introduction of a hydroxyl group led to the highest T_g (−48.2 °C), which can be explained by the strong hydrogen-bond interactions between its molecules [29, 32]. The thermal decomposition properties of the ILs were examined by measuring the weight loss as a function of temperature. Figure 2(b) shows the results, and Table 1 summarizes the T_d of ILs. From Fig. 2(b), the five ILs were stable up to 170 °C, indicative of good thermal stability. The thermal stability of the five ILs were closely related to their molecular structures: With the

increase in the alkyl chain length of the anion group, T_d increased. The thermal stability of the five ILs increased in the order of [Ch][Gly] < [Ch][Ala] < [Ch][Ile] < [Ch][Ser] < [Ch][Phe]. The highest T_d was observed for [Ch][Phe] (195 °C), which was explained by the presence of the phenyl substituent in its anion group.

3.2 Viscosity

Viscosity is defined as the resistance of a fluid to flow, reflecting the manner in which molecules interact to resist motion. Viscosity affects the ability of a lubricant to form a lubricating film, which is considered as one of the most important properties of lubricants. Viscosity is closely related to the chemical structures of the lubricant, as well as their molecular size and shape. To investigate the structure–viscosity relationship of the AA–Ch-based ILs, the kinematic viscosity of the synthesized ILs were measured at 40 and 100 °C. Table 1 summarizes the results. The anion group of the prepared ILs significantly affected their kinematic viscosity: The increase in the size of the anion group possibly led to the increased viscosity of the ILs, related to the strong van der Waals interactions [31, 33]. [Ch][Gly] and [Ch][Ala] with a short chain length exhibited a lower viscosity compared to [Ch][Ile] and [Ch][Phe]. [Ch][Ser] exhibited a higher kinematic viscosity compared to [Ch][Gly] and [Ch][Ala], which can be explained by the strong hydrogen-bond interactions between hydroxyl groups. A hydroxyl group is present in the anion of [Ch][Ser], and two hydroxyl groups are present in its molecular structure; as a result, hydrogen bonds among hydroxyl groups can be easily formed, thereby increasing its viscosity [34]. The different viscosities for the developed ILs suggested that a large number of [Ch][AA] ILs with different viscosities and properties can be obtained by simply changing the anion groups.

3.3 Corrosion

The widely employed copper strip corrosion test is a straightforward method to measure the corrosion of lubricants. In this study, the copper strip corrosion test was carried out to investigate the corrosion properties of the synthesized [Ch][AA] ILs. Figure 3 shows the photographs of the copper strips after the
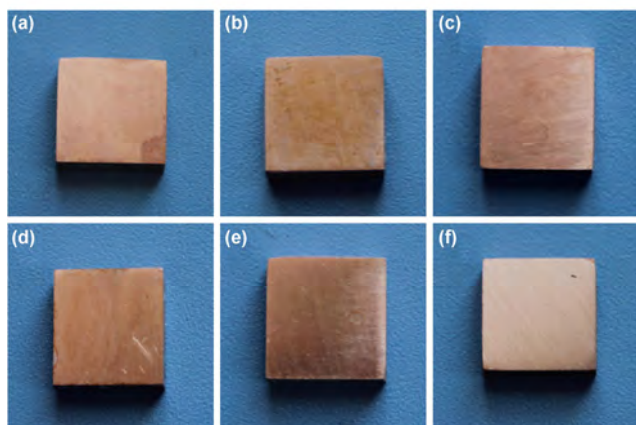
Fig. 3 Photographs of the copper strips after immersion in (a) [Ch][Gly]; (b) [Ch][Ala]; (c) [Ch][Ser]; (d) [Ch][Ile]; (e) [Ch][Phe]. (f) is the photograph of the copper strip before the corrosion test.

test, and the test strips are compared with the standards to determine the corrosion level. From the copper strips tested with the green ILs, almost no corrosion was detected, with a corrosion grade of 1a or 1b in Fig. 3. The non-corrosive property of these ILs is possibly related to the absence of halogen, phosphorus, and sulfur in their molecules.

3.4   Tribological properties

The tribological properties of the synthesized ILs were tested using a Schwingungs Reibung und Verschleiss (SRV) tester. A conventional halogen-containing IL, e.g., [C$_6$mim][NTf$_2$], was used for comparison. Figure 4 shows the evolution of the friction coefficient of these lubricants at room temperature. All lubricants exhibited a relatively short running-in time. The coefficient of friction (COF) of all the tested lubricants increased in the order of [Ch][Gly] < [Ch][Ala] < [Ch][Ile], [C$_6$mim][NTf$_2$], [Ch][Ser] < [Ch][Phe]. The lowest COF was observed for [Ch][Gly] (0.085), which showed a 20% reduction compared to the traditional IL [C$_6$mim][NTf$_2$]. No friction modifiers or other lubrication additives were present in ILs, and the friction properties of [Ch][AA] ILs were not dominated by the performance of the boundary additives. As shown in Table 1, an increase in the anion size of [Ch][AA] ILs resulted in the increase in viscosity. [Ch][Phe] exhibited significantly higher viscosity compared to [Ch][Gly] and [Ch][Ala], and the inferior anti-friction performance of [Ch][Phe] compared to

[Ch][Gly] and [Ch][Ala] indicated a greater dependence on lubricant viscosity for [Ch][AA] ILs [35]. The above results suggested that the friction-reducing behavior of the developed halogen-, phosphorus-, and sulfur-free ILs is comparable or even better than the traditional halogen-containing ILs, with the exception of [Ch][Phe]. Figure 5 shows the wear volume of the steel discs with different lubricants. The wear volume losses of [Ch][Gly] and [Ch][Ala] were greater than that of [C$_6$mim][NTf$_2$], while those of [Ch][Ile], [Ch][Ser], and [Ch][Phe] were considerably less than that of [C$_6$mim][NTf$_2$]. The lowest wear volume was observed for ILs with the longest alkyl chain [Ch][Phe], with a 46% wear reduction compared to [C$_6$mim][NTf$_2$]. Similar trends were observed between the wear scar diameter (WSD) of the ball lubricated with ILs and the wear volume of the discs (Table 2). The anti-wear
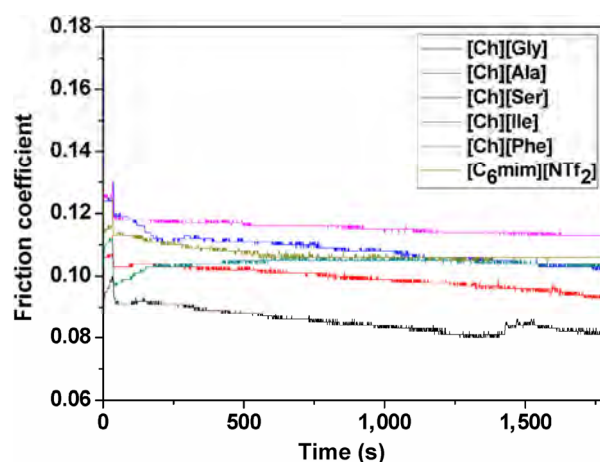

Fig. 4 Evolution of the friction coefficients of the system lubricated with [Ch][AA] ILs and [C$_6$mim][NTf$_2$].
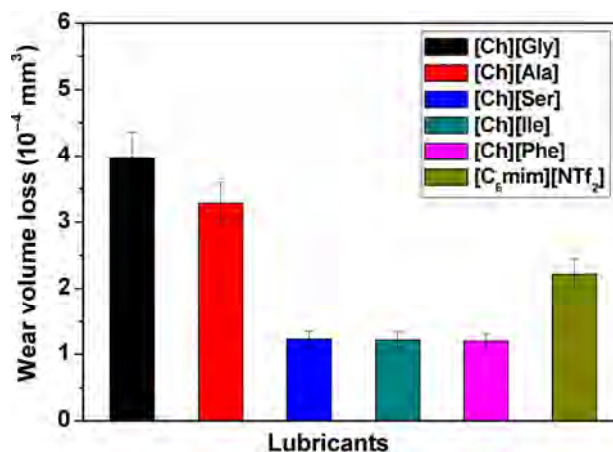

Fig. 5 Evolution of the wear volume loss of steel discs lubricated with [Ch][AA] ILs and [C$_6$mim][NTf$_2$].

Table 2 Ball wear diameter after the SRV test for different ILs.

Lubricant	[Ch][Gly]	[Ch][Ala]	[Ch][Ser]	[Ch][Ile]	[Ch][Phe]	[C$_6$mim][NTf$_2$]
WSD (mm)	0.337	0.333	0.293	0.302	0.297	0.343

property of [Ch][AA] ILs is thought to be related to the effective boundary films between friction pairs. To characterize the boundary films, *in situ* average contact resistance measurement was carried out using the SRV tester [36, 37]. Figure 6 shows the contact resistance change using [Ch][AA] ILs and [C$_6$mim][NTf$_2$] as the lubricants. [Ch][Ala] and [Ch][Gly] ILs exhibited an extremely low contact resistance for the sliding contact, while [Ch][Ile], [Ch][Ser], and [Ch][Phe] exhibited considerably higher contact resistance, indicating that the significantly thicker films lubricated with [Ch][Ile], [Ch][Ser], and [Ch][Phe] ILs exhibit considerably effective anti-wear properties.

3.5 Surface characterization

Figure 7 shows the SEM micrographs and 3D optical microscopic images of steel discs lubricated with different ILs: All wear scars were obtained under the same conditions. As can be observed in the SEM micrographs, the worn surfaces lubricated by [Ch][Gly] and [Ch][Ala] exhibited severe scuffing and significantly wider and deeper wear scars, which were further confirmed by the 3D optical microscopic images. From the SEM micrograph of the worn area lubricated with [C$_6$mim][NTf$_2$], an extremely rough surface was

Fig. 6 Contact resistance of [Ch][AA] ILs and [C$_6$mim][NTf$_2$] recorded using the SRV tester.

observed, with several small furrows and scratches, while the wear depth was considerably reduced compared to [Ch][Gly] and [Ch][Ala] ILs. The worn surfaces lubricated with [Ch][Ile], [Ch][Ser], and [Ch][Phe] were comparatively smoother, and severe scuffing was considerably reduced. The widths and depths of the wear scars lubricated with [Ch][Ile], [Ch][Ser], and [Ch][Phe] were smaller and shallower, as shown in the 3D optical microscopic images. This result is consistent with those obtained for the measured wear volume and wear diameter in Fig. 5 and Table 2, respectively.

The chemical composition of the wear scars was confirmed by EDS and XPS after tribological tests. From the EDS images of the worn steel surface in Fig. 8, C, O, Cr, and Fe were abundant on the discs lubricated with [Ch][Gly] and [Ch][Ser]. However, nitrogen was not detected by EDS possibly because of its low content. XPS was also carried out to accurately analyze the composition of the surface after lubrication by [Ch][AA] ILs. No obvious difference was observed in the XPS spectra of C1s, O1s, N1s, and Fe2p after lubrication with [Ch][Gly] and [Ch][Ser] (Fig. 9). The peaks of Fe2p were observed at approximately 725.1 and 711.2 eV (Fig. 9), corresponding to Fe$_2$O$_3$, Fe$_3$O$_4$, Fe(OH)O, and FeOOH. A wide O1s peak was observed at 531.2–530.0 eV, corresponding to Fe$_2$O$_3$, Fe$_3$O$_4$, Fe(OH)O, and FeOOH [38]. The iron surface may easily undergo oxidation during sliding, with the formation of an oxide layer. A N1s absorption peak was not observed in the XPS spectrum, indicating that the excellent tribological properties of [Ch][AA] ILs may lead to the formation of a physically adsorbed film rather than the tribochemical reaction films on the friction pairs. During the tribological process, the carboxyl groups from AA anions are easily adsorbed on the positively charged metallic surface via electrostatic attractions, which effectively prevent the frictional pairs from direct contact [24, 39]. This physically adsorbed film may have been thoroughly cleaned by ultrasonication, leading to the absence of N in the EDS and XPS
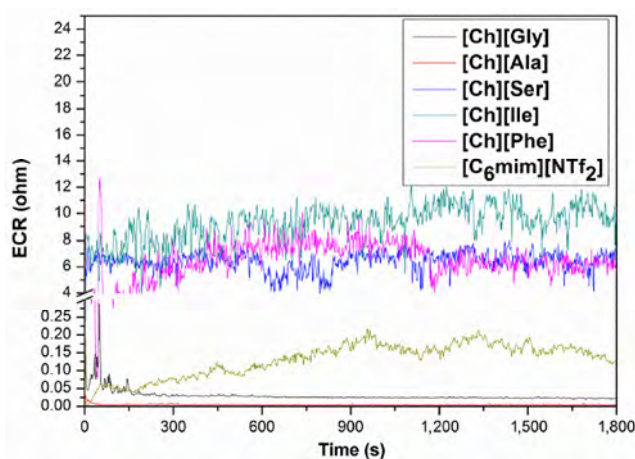
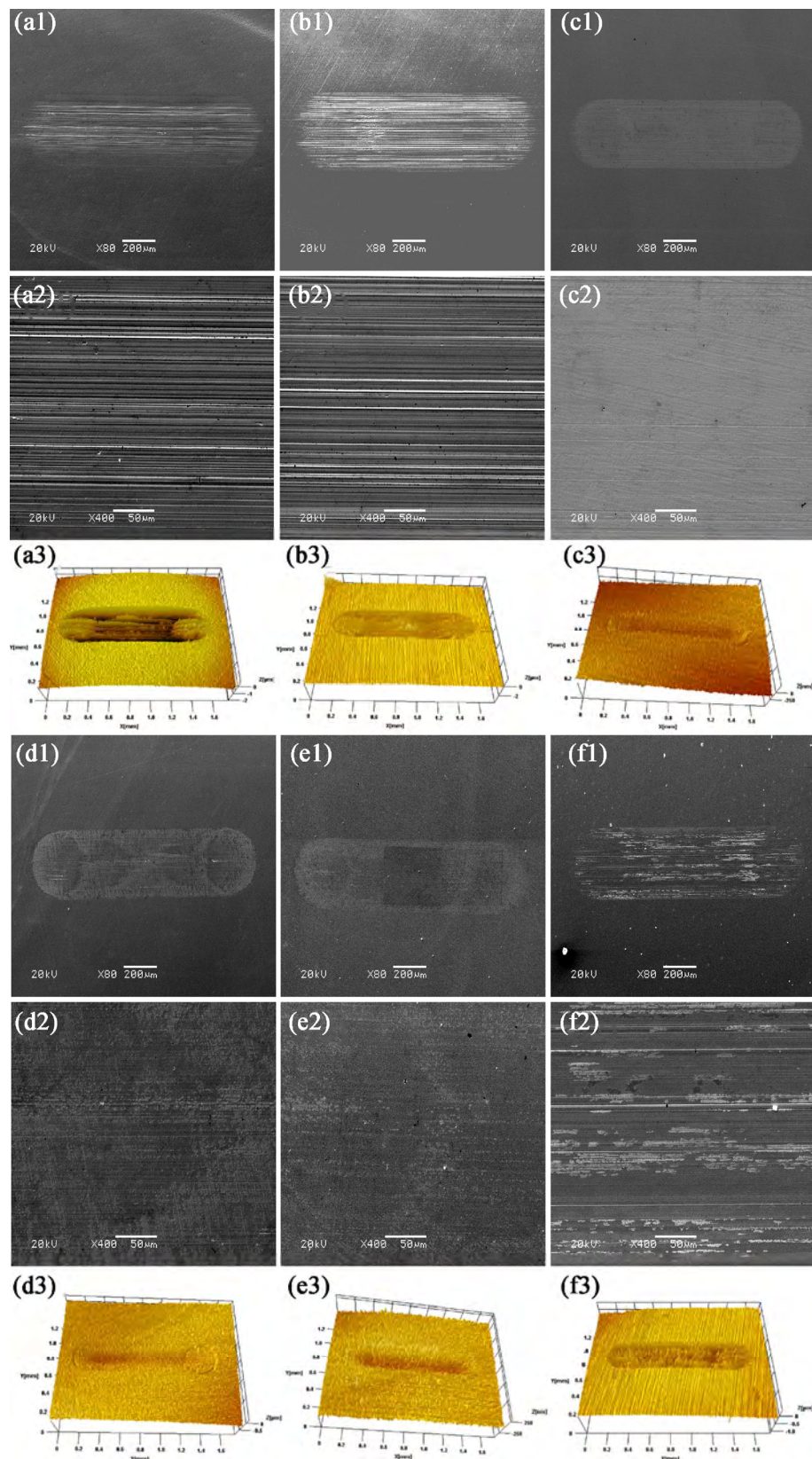**Fig. 7** SEM micrographs and 3D optical microscopic images of the worn steel discs with different lubricants: [Ch][Gly] (a1, a2, and a3); [Ch][Ala] (b1, b2, and b3); [Ch][Ile] (c1, c2, and c3); [Ch][Ser] (d1, d2, and d3); [Ch][Phe] (e1, e2, and e3); and [C_6mim][NTf_2] (f1, f2, and f3).

Element	wt %	at %
C	5.49	21.09
N	0.00	0.00
O	0.35	1.00
Cr	1.54	1.36
Fe	92.63	76.55

Element	wt %	at %
C	4.84	18.95
N	0.00	0.00
O	0.36	1.06
Cr	1.62	1.47
Fe	93.18	78.52
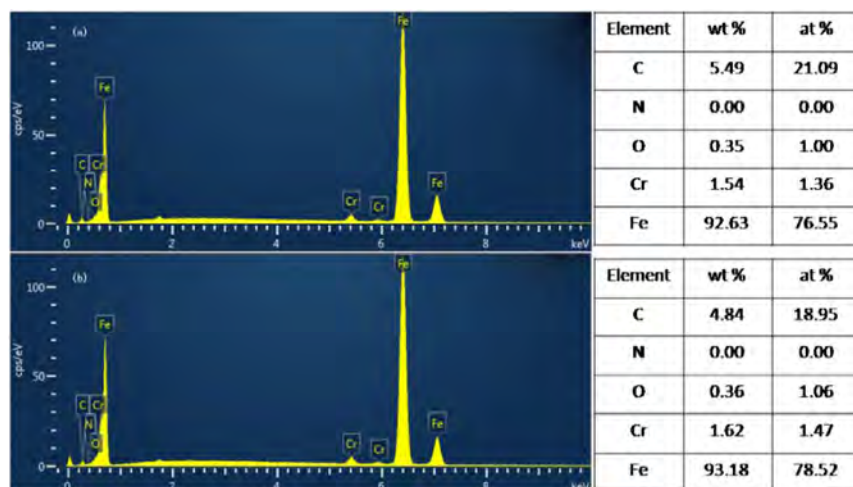
Fig. 8 EDS imaging profiles for the worn steel surface lubricated with (a) [Ch][Gly] and (b) [Ch][Ser].
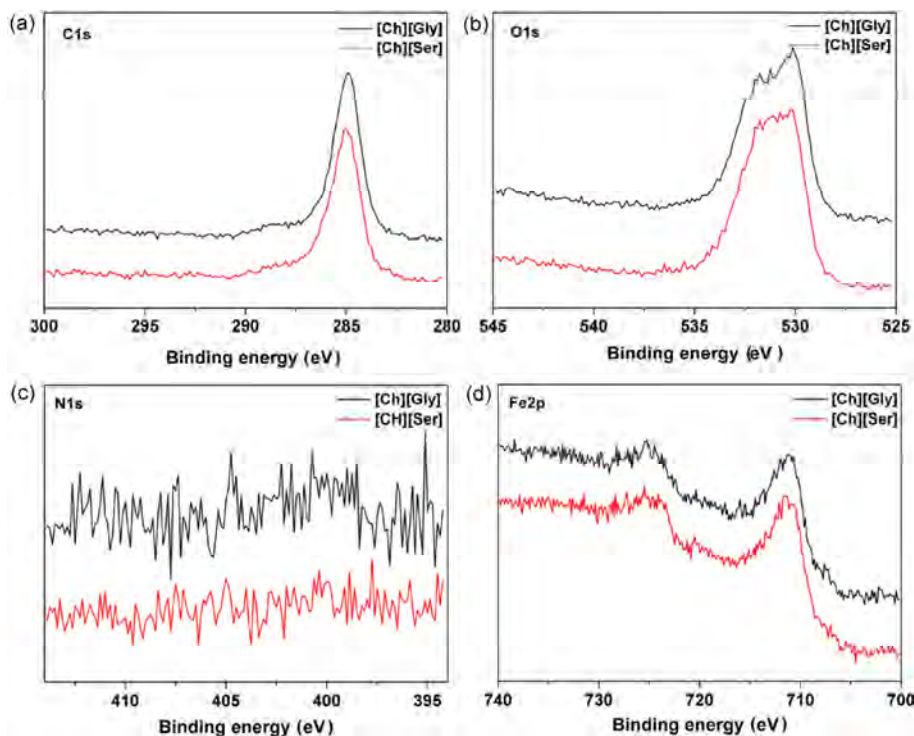
Fig. 9 C1s, O1s, N1s, and Fe2p XPS region scans for wear scars with [Ch][Gly] and [Ch][Ser] lubricants.

images. The halogen-, sulfur-, and phosphorus-free ILs were more prone to form a physically adsorbed film on friction pairs. This result is in good agreement with those reported previously [23, 24, 30].

4 Conclusion

In this study, five environmentally friendly halogen-, sulfur-, and phosphorus-free [Ch][AA] ILs were synthesized by a simple, green method with only water as the by-product. The results indicated that the physical and thermal properties of ILs are closely related to their molecular structures. The copper strip test suggested that ILs exhibit slight corrosion toward copper at 100 ℃ for 72 h. In addition, [Ch][AA] ILs also exhibited good tribological properties for steel/steel contact, which are comparable to conventional [C$_6$mim][NTf$_2$]. The excellent tribological properties

of [Ch][AA] ILs were related to the formation of a physically adsorbed film on the metallic surface, which can effectively prevent the friction pairs from direct contact during rubbing. Notably, because of the abundance of AAs in nature, different [Ch][AA] ILs can be obtained by simply changing amino acids. The design, synthesis, lubricating properties, and tribological mechanism of other [Ch][AA] ILs still need to be further examined. Overall, the excellent tribological properties, low toxicity, high biodegradability, cost-effectiveness, as well as halogen-, sulfur-, and phosphorus-free characteristics of these [Ch][AA] ILs make them promising candidates for use as green lubricants in the modern industry.

Acknowledgments

References

[1] Boyde S. Green lubricants. Environmental benefits and impacts of lubrication. *Green Chemistry* **4**(4): 293–307 (2002)

[2] Hörner D. Recent trends in environmentally friendly lubricants. *Lubrication Science* **18**(4): 327–347 (2002)

[3] Salimon J, Salih N, Emad Y. Biolubricants: Raw materials, chemical modifications and environmental benefits. *European Journal of Lipid Science and Technology* **112**(5): 519–530 (2010)

[4] Song Z H, Liang Y M, Fan M J, Zhou F, Liu W M. Lithium-based ionic liquids as novel lubricant additives for multiply alkylated cyclopentanes (MACs). *Friction* **1**(3): 222–231 (2013)

[5] Raghunanan L, Narine S S. Engineering green lubricants I: optimizing thermal and flow properties of linear diesters derived from vegetable oils. *ACS Sustainable Chemistry & Engineering* **4**(3): 686–692 (2016)

[6] Raghunanan L, Narine S S. Engineering Green Lubricants II: Thermal transition and flow properties of vegetable oil-derived diesters. *ACS Sustainable Chemistry & Engineering* **4**(3): 693–700 (2016)

[7] Erhan S Z, Sharma B K, Liu Z S, Adhvaryu A. Lubricant base stock potential of chemically modified vegetable oils.

Journal of Agricultural and Food Chemistry **56**(19): 8919–8925 (2008)

[8] Erhan S Z, Asadauskas S. Lubricant basestocks from vegetable oils. *Industrial Crops and Products* **11**(2–3): 277–282 (2000)

[9] Sharma B K, Perez J M, Erthan S Z. Soybean oil-based lubricants: A search for synergistic antioxidants. *Energy & Fuels* **21**(4): 2408–2414 (2007)

[10] Li W M, Jiang, C, Chao M R, Wang, X B. Natural garlic oil as a high-performance, environmentally friendly, extreme pressure additive in lubricating oils. *ACS Sustainable Chemistry & Engineering* **2**(4): 798–803 (2014)

[11] Chandrasekaran S R, Murali D. Antioxidants from slow pyrolysis bio-oil of birch wood: application for biodiesel and biobased lubricants. *ACS Sustainable Chemistry & Engineering* **4**(3): 1414–1421 (2016)

[12] Gusain R, Dhingra S, Khatri O P. Fatty-acid-constituted halogen-free ionic liquids as renewable, environmentally friendly, and high-performance lubricant additives. *Industrial & Engineering Chemistry Research* **55**(4): 856–865 (2016)

[13] Earle M J, Seddon K R. Ionic liquids. Green solvents for the future. *Pure and Applied Chemistry* **72**(7): 1391–1398 (2000)

[14] Patel D D, Lee J-M. Applications of ionic liquids. *The Chemical Record* **12**(3): 329–355 (2012)

[15] Rogers R D, Seddon K R. Ionic liquids-solvents of the future? *Science* **302**(5646)：792–793 (2003)

[16] Plechkova N V, Seddon K R. Applications of ionic liquids in the chemical industry. *Chemical Society Reviews* **37**(1): 123–150 (2008)

[17] Ye C F, Liu W M, Chen Y X, Yu L G. Room-temperature ionic liquids: A novel versatile lubricant. *Chemical Communications* (21): 2244–2245 (2001)

[18] Bermúdez M-D, Jiménez A-E, Sanes J, Carrión F-J. Ionic liquids as advanced lubricant fluids. *Molecules* **14**(8): 2888–2908 (2009)

[19] Zhou F, Liang Y M, Liu W M. Ionic liquid lubricants: designed chemistry for engineering applications. *Chemical Society Reviews* **38**(9): 2590–2599 (2009)

[20] Swatloski R P, Holbrey J D, Rogers R D. Ionic liquids are not always green: hydrolysis of 1-butyl-3-methylimidazolium hexafluorophosphate. *Green Chemistry* **5**(4): 361–363 (2003)

[21] Gusain R, Singh R, Sivakumar K L N, Khatri O P. Halogen-free imidazolium/ammonium-bis(salicylato) borate ionic liquids as high performance lubricant additives. *RSC Advances* **4**: 1293–1301 (2014)

[22] Nosonovsky M, Bhushan B. Green tribology: principles, research areas and challenges. *Philosophical Transactions of the Royal Society a-Mathematical Physical and Engineering Sciences* **368**(1929): 4677–4694 (2010)

[23] Khatri P K, Thakre G D, Jain S L. Tribological performance evaluation of task-specific ionic liquids derived from amino acids. *Industrial & Engineering Chemistry Research* **52**(45): 15829–15837 (2013)

[24] Song Z H, Liang Y M, Fan M J, Zhou F, Liu W M. Ionic liquids from amino-acids: fully green fluid lubricants for various contacts. *RSC Advances* **4**(37): 19396–19402 (2014)

[25] Petkovic M, Ferguson J L, Gunaratne H Q N, Ferreira R, Leitão M C, Seddon K R, Rebelo L P N, Pereira C S. Novel biocompatible cholinium-based ionic liquids-toxicity and biodegradability. *Green Chemistry* **12**(4): 643–649 (2010)

[26] Nagendramma P, Kaul S. Development of ecofriendly/ biodegradable lubricants: An overview. *Renewable and Sustainable Energy Reviews* **16**(1): 764–774 (2012)

[27] Hou X D, Liu Q P, Smith T J, Li N, Zong M H. Evaluation of toxicity and biodegradability of cholinium amino acids ionic liquids. *Plos One* **8**(3): 1–7 (2013)

[28] Moriel P, García-Suárez E J, Martínez, M, García A B, Montes-Morán M A, Calvino-Casilda V, Bañares M A. Synthesis, characterization, and catalytic activity of ionic liquids based on biosources. *Tetrahedron Letters* **51**(37): 4877–4881 (2010)

[29] Tao D J, Cheng Z, Chen F F, Li Z M, Hu N, Chen X S. Synthesis and thermophysical properties of biocompatible cholinium-based amino acid ionic liquids. *Journal of Chemical & Engineering Data* **58**(6): 1542–1548 (2013)

[30] Mu L W, Shi Y J, Guo X J, Ji T, Chen L, Yuan R X, Brisbin L, Wang H Y, Zhu J H. Non-corrosive green lubricants: strengthened lignin- choline amino acid ionic liquids interaction via reciprocal hydrogen bonding. *RSC Advances* **5**(81): 66067–66072 (2015)

[31] Bonhôte P, Dias A-P, Papageorgiou N, Kalyanasundaram K, Grätzel M. Hydrophobic, highly conductive ambient-temperature molten salts. *Inorganic Chemistry* **35**(5): 1168–1178 (1996)

[32] Liu Q P, Hou X D, Li N, Zong M H. Ionic liquids from renewable biomaterials: synthesis, characterization and application in the pretreatment of biomass. *Green Chemistry* **14**(2): 304–307 (2012)

[33] Song Y X, Xia Y Q, Liu Z L. Influence of cation structure on physicochemical and antiwear properties of hydroxyl-functionalized imidazolium bis(trifluoromethylsulfonyl)imide ionic liquids. *Tribology Transactions* **55**(6): 738–746 (2012)

[34] Li J J, Zhang C H, Luo J B. Superlubricity achieved with mixtures of polyhydroxy alcohols and acids. *Langmuir* **29**(17): 5239–5245 (2013)

[35] Lawes S D A, Hainsworth S V, Blake P, Ryder K S, Abbott A P. Lubrication of steel/steel contacts by choline chloride ionic liquids. *Tribology Letters* **37**(2): 103–110 (2010)

[36] Cai M R, Liang Y M, Zhou F, Liu W M. Anticorrosion imidazolium ionic liquids as the additive in poly(ethylene glycol) for steel/Cu-Sn alloy contacts. *Faraday Discussions* **156**(1): 147–157 (2012)

[37] Fan M J, Song Z H, Liang Y M, Zhou F, Liu W M. Laxative inspired ionic liquid lubricants with good detergency and no corrosion. *ACS Applied Materials & Interfaces* **6**(5): 3233–3241 (2014)

[38] NIST X-ray Photoelectron Spectroscopy Database 20, Version 4.1: National Institute of Standards and Technology (NIST) Material Measurement Laboratory (MML). http://srdata.nist.gov/xps/, 2017.

[39] Jiménez A E, Bermúdez M D. Imidazolium ionic liquids as additives of the synthetic ester propylene glycol dioleate in aluminium–steel lubrication. *Wear* **265**(5–6): 787–798 (2008)

Wenjing LOU. She received her PhD degree in Lanzhou Institute of Chemical Physics, Chinese Academy of Sciences in 2007. Her current position is an associate researcher in the State Key Laboratory of Solid Lubrication at Lanzhou Institute of Chemical Physics, Chinese Academy of Sciences. Her research areas include nanofluids, nanoparticle lubricant additives, and high performance lubricants.

Cheng JIANG. She received her PhD degree in Lanzhou Institute of Chemical Physics, Chinese Academy of Sciences in 2013. After then, she worked as an assistant research fellow in State Key Laboratory of Solid Lubrication at Lanzhou Institute of Chemical Physics, Chinese Academy of Sciences. Her research interests mainly focus on high performance lubricants.

Jingyan NIAN. He received his master degree in physical chemistry in 2012 from Northwest Normal University, Lanzhou, China. During his undergraduate, he joined the State Key Laboratory of Solid Lubrication at Lanzhou Institute of Chemical Physics, Chinese Academy of Sciences. His current position is an assistant research fellow. His research area covers the atomic-scale friction, superlubricity, and space lubrication.

Powder metallurgy processed metal-matrix friction materials for space applications

Yelong XIAO[1], Pingping YAO[1,*], Kunyang FAN[1], Haibin ZHOU[1], Minwen DENG[1], Zongxiang JIN[2]

[1] *State Key Laboratory of Powder Metallurgy, Central South University, Changsha 410083, China*

[2] *Shanghai Key Laboratory of Spacecraft Mechanism, Shanghai 201108, China*

Abstract: Owing to the increasing demand for tribological brakes for space applications, the development of novel materials and advanced technologies is necessary. This paper presents the design, characterization, and realization of powder metallurgy processed metal-matrix friction materials intended for the above-mentioned tribological brakes. Selecting appropriate ingredients, which provides an effective way to tailor the properties of the friction material, is evolving as a strategy to meet the design requirements. The tribological behaviors of the friction material are experimentally investigated under different conditions, and special attention is focused on the vacuum tribology. Examinations and analyses of the friction surface and subsurface corroborate the wear mechanism. In addition, the erosion resistances of the friction material are evaluated by exposure tests of ultraviolet irradiation and atomic oxygen. Finally, present and potential space applications of the friction material are also introduced based on experimental studies.

1 Introduction

The success of space missions depends critically on the reliability of space mechanisms and this in turn is dependent on the life and functionality of their component parts [1]. Space tribology is the management of friction and wear processes in those parts that have a tribological element, and focuses on anti-friction and anti-wear properties [2–4]. However, reports concerning tribological brakes that execute the braking operations, clutching operations, or overload protection of spacecraft or space mechanism are limited, especially in certain fields like friction materials.

Although tribological brakes represent only a tiny fraction of the spacecraft's cost, they are responsible for avoiding single-point failures that cripple or debilitate expensive spacecraft, such as brake failures for the docking mechanism determining the rendezvous and docking of spacecrafts. The purposes of brakes within the anticipated operational scenario are the following: precise velocity control; stable, limited, selectively controlled output frictional torque; long lifetime; and high reliability. In addition, unlike traditional brake systems, for space mechanisms only one brake should take on two or more of the aforementioned functions so as to reduce payload weight and size and, thus, the cost of missions.

The mechanical, environmental, and endurance requirements of space applications exceed the capabilities of available brake technology, resulting in a demand for novel materials and technologies that are more advanced. Lv et al. [5] fabricated carbon and aramid fibers reinforced polyimide composites for application in spacecrafts. Hawthorne et al. [6] demonstrated that polymeric and some ceramic materials exhibit low sliding friction. Some ceramic-based materials show stable friction characteristics, with low wear rates, and thus are potentially suitable

---

* Corresponding author: Pingping YAO, E-mail: yaopingpingxx@sohu.com

for use in long-life space mechanisms such as the brakes in the space station remote manipulator system. Baker et al. [7] examined the tribological properties of a ceramic material for a brake intended for the European Robotic Arm (ERA) under different conditions. Unfortunately, the ceramic material is susceptible to non-linear and "dysfunctional" effects when subjected to testing in standard thermal and pressure environments.

In 2003, Central South University initiated and pioneered the study of novel friction materials for space applications in China [8–10]. Consequently, after eight years, a powder metallurgy processed metal-matrix friction material was used in the docking mechanism for the "Shenzhou" docking mission. In this paper, selected highlights of a fourteen-year study of powder metallurgy processed metal-matrix friction materials for space applications will be presented, particularly in the area of friction materials design.

2 Experimental procedures and materials

2.1 Experimental procedures

2.1.1 Friction and wear test

Friction and wear behaviors of metal-matrix friction materials were tested with a ring-on-ring braking test system (Fig. 1) which was equipped with a low-temperature vacuum chamber. The friction pairs of the friction materials with 2Cr13 stainless steel (0.16-0.35 C, 12-14 Cr, ≤1.0 Si, ≤0.035 P, ≤0.03 S, ≤1.0 Mn, and Fe balance, HRC 40±2) as counterparts were machined into rings with an 80 mm outer diameter and a 50 mm inner diameter. The counterpart surface was tumbled to a mean surface roughness, R_a, of 0.2 μm.

The tests were performed by accelerating the rotation shaft with the counterpart ring to the desired rotational speed. When this speed was attained, the motor power was switched off and the friction ring was loaded closely against the counterpart ring at a desired normal pressure until the rotation shaft completely stopped rotating. This test was repeated 10 times for each specimen. This test system was equipped with a computerized data acquisition and control system for controlling and monitoring of various parameters. The test parameters are given in Table 1.
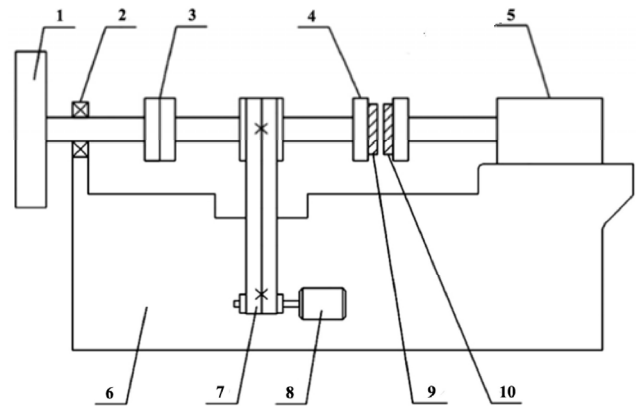

Fig. 1 A schematic diagram of the ring-on-ring braking test system: 1-flywheel, 2-bearing, 3-clutch, 4-rotation shaft, 5-air cylinder, 6-concrete base, 7-feed belt, 8-motor, 9-counterpart ring, 10-friction ring.

Table 1 Test parameters employed in wear tests.

Parameters	Values
Rotational speed (rpm)	3000
Nominal contact pressure (MPa)	0.016, 0.032, 0.048, and 0.064
Vacuum pressure (Pa)	$1\times10^0 - 1\times10^{-2}$, and 1×10^{-3}
Temperature (°C)	Room temperature (25), 0, −20, and −40

During each test period, the instantaneous friction coefficient (μ) can be calculated as

$$\mu = \frac{2M}{F_a(r_0 + r_i)} \tag{1}$$

where M is the measured frictional torque, r_0 is the half outer diameter of rings, r_i is the half inner diameter of rings, and F_a is the normal force.

The mean friction coefficient (μ_{mean}) is defined as

$$\mu_{\text{mean}} = \frac{1}{(t_1 - t_c)} \int_{t_c}^{t_1} \mu(\tau) \mathrm{d}\tau \tag{2}$$

where t_1 is the lock-up time (rotational speed = 0), t_c is the time at which rings are brought in contact, and $\mu(t)$ is the instantaneous friction coefficient.

The frictional stability (FS) is defined as

$$\text{FS} = \frac{\mu_{\text{mean}}}{\mu_{\text{max}}} \tag{3}$$

where μ_{max} is the maximum friction coefficient.

During wear tests, the wear rate (ω) is defined as

$$\omega = \frac{m_0 - m_i}{n} \tag{4}$$

where m_0 is the weight of friction rings before wear tests, m_i is the weight of friction rings after wear tests, and n is the number of cycles.

The amount of wear was determined by weighing friction rings before and after wear tests using a precision electronic balance with an accuracy of 0.001 g. The morphologies of the friction surface and subsurface were observed using scanning electron microscopy (SEM).

2.1.2 Equipment to evaluate brakes for space applications

The tribological performances of the brakes for space applications were evaluated using a multi-disc clutch brake system at the Shanghai Key Laboratory of Spacecraft Mechanism. The brake system was mounted inside a special ground simulation system which was equipped with temperature control in a range between −120 °C and +180 °C and could be evacuated to a residual pressure of 1×10^{-5} Pa.

In this study, the ground simulation testing procedure we have proposed is the same as that published in our previous work [9], and will not be described in detail here. The frictional torque of the brakes was measured with a torque sensor, and the data was automatically sent for processing to a computer.

2.1.3 Irradiation test

Atomic oxygen (AO) and ultraviolet irradiation (UV) experiments were carried out in ground simulation facilities under a vacuum environment (1×10^{-3} Pa). AO irradiation was performed by impingement with a mean translational kinetic energy of 5 eV and flux of 5.2×10^{15} atoms·cm^{-2}·s^{-1}. This is equal to the impact energy of AO on the surfaces of spacecraft in the actual low earth orbit (LEO) space environment. The exposure period was controlled at 480 min. UV irradiation was performed with a wavelength range of 115–400 nm and the energy flux was determined to be about six fold that of the solar constant. The exposure period was controlled at 600 min, being equivalent to 60 sun hours. In AO/UV combining irradiation experiments, samples were irradiated firstly by AO, and then by UV.

During irradiation tests, the mass loss rate (Δm) is

defined as

$$\Delta m = \frac{m - m_1}{S} \tag{5}$$

where m is the weight of samples before irradiation tests, m_1 is the weight of samples after irradiation tests, and S is the irradiated area. The mass loss was determined by weighing samples before and after irradiation tests using a precision electronic balance with an accuracy of 0.001 g.

2.2 Materials design issues

Metal-matrix friction composites can be defined as a metallic matrix (usually an alloy of Cu, Fe, or Ni) containing lubricant components and friction components. Due to their excellent tribological properties and adaptability to working conditions, those materials fabricated via powder metallurgy route hold great promise for space applications. The properties of the composites can be tailored by selecting appropriate constituents in order to meet the design requirements.

2.2.1 Metal matrix

The metallic constituents employed in the friction material provide strength, high temperature stability, oxidation resistance, and high thermal conductivity [11]. Generally, the contents of the metal matrix should be controlled in the range of 40–80 wt%. Copper and iron have been found to be promising candidates for practical use as the matrix phase. In order to determine the preferable matrix, the total amount of Cu and Fe in this study was 70 wt%. Different weight fractions of Cu were added in the range of 0 wt%, 10 wt%, 20 wt%, 30 wt%, 40 wt%, 50 wt%, 60 wt%, and 70 wt%. Thus, the additions of Fe were correspondingly in the range of 70 wt%, 60 wt%, 50 wt%, 40 wt%, 30 wt%, 20 wt%, 10 wt%, and 0 wt%, respectively. The contents of other ingredients were fixed (5–7 wt% Sn, 5–7 wt% graphite, 6–8 wt% MoS_2, 5–7 wt% SiO_2, 4–8 wt% others).

Figure 2(a) shows μ_{mean} and FS as a function of Cu content. A significant decrease was observed in the μ_{mean} values with an increase in Cu content up to 30 wt% after which a slightly decreasing trend was observed. Vibrations created by brakes are often harmful during space operations. Steady operations
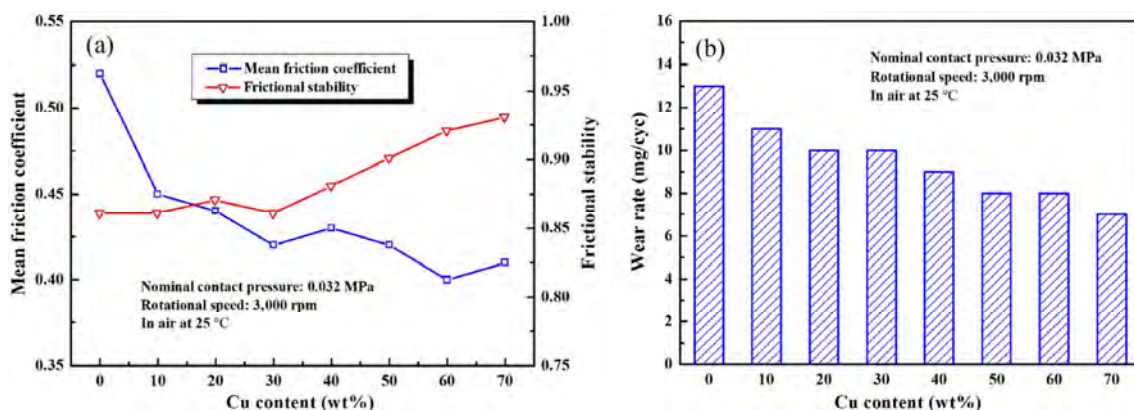
Fig. 2 Variations of (a) μ_{mean} and FS, and (b) wear rate with Cu content.

and lower vibration depend on FS. The greater the FS, the steadier and lower the vibrations. The FS was low and stable at Cu contents below 30 wt% and then increased at Cu contents above 30 wt%. The effects of Cu content on the wear rate are summarized in Fig. 2(b). With increasing Cu content, the wear rate reduced significantly.

The strength and hardness of Fe are higher than those of Cu, so the hard Fe particles resisted the microcutting actions of the counterpart and abrasives more effectively during the course of friction. Simultaneously, the accumulation of Fe particles removed from the friction material on the surface enhanced the friction resistance between two contacting surfaces. Secondly, compared with Cu, Fe was more prone to adhering to the steel counterpart, so Fe particles tended to weld with the counterpart under the influences of the applied load and frictional heat [12]. This resulted in the increase in the friction coefficient, the decrease in FS, and the increase in the wear rate. Thirdly, Cu dissipated frictional heat more effectively, so it can improve the tribological properties owing to the superior thermal conductivity. Hence, copper was selected to be the metal matrix. Furthermore, the addition of Sn to materials contributed to improve the strength and hardness of the copper matrix.

2.2.2 Lubricant components

Lubricants like graphite or MoS_2 impart smoother and vibration less engagement during the course of friction, and also provide anti-seizure characteristics and enhance wear resistance [13]. The combined effects

of graphite and MoS_2 on the tribological properties were evaluated. The total amount of graphite and MoS_2 in this study was 12 wt%. Different weight fractions of graphite, in the range of 12 wt%, 10 wt%, 8 wt%, 6 wt%, 4 wt%, 2%, and 0 wt%, were added. The respective amounts of MoS_2 added were 0 wt%, 2 wt%, 4 wt%, 6 wt%, 8 wt%, 10 wt%, and 12 wt%. The contents of other ingredients were fixed (43−60 wt% Cu, 5−7 wt% Sn, 5−8 wt% Fe, 5−7 wt% SiO_2, 5−7 wt% $CaCO_3$, 8−12 wt% others).

Figure 3(a) presents the variations of μ_{mean} and FS with the mass ratio of graphite to MoS_2. μ_{mean} was almost unchanged with an increase in the mass ratio up to 6:6, and then promptly increased and rapidly reached a relatively stable value at the mass ratio above 6:6. FS was almost insensitive to the change of graphite and MoS_2 content. As shown in Fig. 3(b), the wear rate slightly increased with increasing the mass ratio to 8:4 and reached the lowest value when the mass ratio was 6:6, and then significantly increased with increasing the mass ratio.

In our previous work [8], it was found that solid-solid phase reactions occurred between MoS_2 and other constituents in the sintering process. The reaction products were complicated Mo_2C, $Cu_{10.98}Mo_{18}S_{24}$, Cu_7S_4, and $CaMoO_4$. Just like graphite and MoS_2, $Cu_{10.98}Mo_{18}S_{24}$, and Cu_7S_4 acting as lubricants were responsible for the desired effect of friction force stabilization. Mo_2C and $CaMoO_4$ were homogeneously embedded in the matrix, and acted as abrasives resulting in dispersion strengthening and could enhance the friction resistance and improve the wear-resistance to some extent. Nevertheless, as a result of the production of new
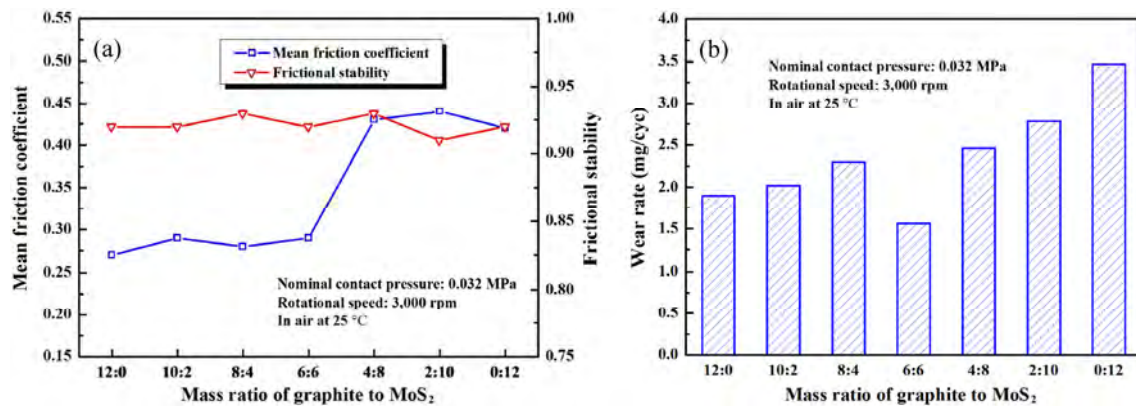
Fig. 3 Variations of (a) μ_{mean} and FS, and (b) wear rate with mass ratio of graphite to MoS$_2$.

compounds, the abrasive level increased with increasing MoS$_2$ content, the hardness of materials ascended, while compression strength descended, resulting in the increase in the friction coefficient and wear rate. However, there was an equilibrium mass of lubricant and abrasive that was achieved by tailoring the mass ratio of graphite to MoS$_2$, at which point (i.e., a mass ratio was 6:6) the friction material attained outstanding comprehensive properties.

2.2.3 Friction components

Abrasives, such as SiO$_2$, SiC, or mullite are used to provide the desired friction coefficient and protect against the negative effects of lubricants [11]. The effects of SiO$_2$ content on the friction and wear behaviors were studied. The total amount of SiO$_2$ and Cu in this study was 60 wt%. Different weight fractions of SiO$_2$, in the range of 0 wt%, 2 wt%, 4 wt%, 6 wt%, 8 wt%, 10 wt%, and 12 wt%, were added. Thus, the additions of Cu were correspondingly in the range of

60 wt%, 58 wt%, 56 wt%, 54 wt%, 52 wt%, 50 wt%, and 48%. The contents of other ingredients were fixed (5–7 wt% Sn, 5–8 wt% Fe, 5–7 wt% graphite, 6–8 wt% MoS$_2$, 3–5 wt% Al$_2$O$_3$, 6–10 wt% others).

Figure 4(a) presents μ_{mean} and FS as a function of the SiO$_2$ weight fraction. μ_{mean} was noticeably enhanced by the addition of SiO$_2$ into the friction formulations. A significant increase occurred in FS upon increasing SiO$_2$ content up to 6 wt% after which a slight decreasing trend was observed. The influences of SiO$_2$ content on the wear rate are shown in Fig. 4(b). The wear rate decreased upon decreasing SiO$_2$ content to below 6 wt% and then increased at SiO$_2$ concentrations above 6 wt%.

Due to its high strength and hardness, SiO$_2$ prevented the movement between two friction surfaces resulting in a higher friction coefficient. The amount of hard inclusions penetrating the friction layer obviously increased with increasing SiO$_2$ content, so the friction coefficient correspondingly increased.
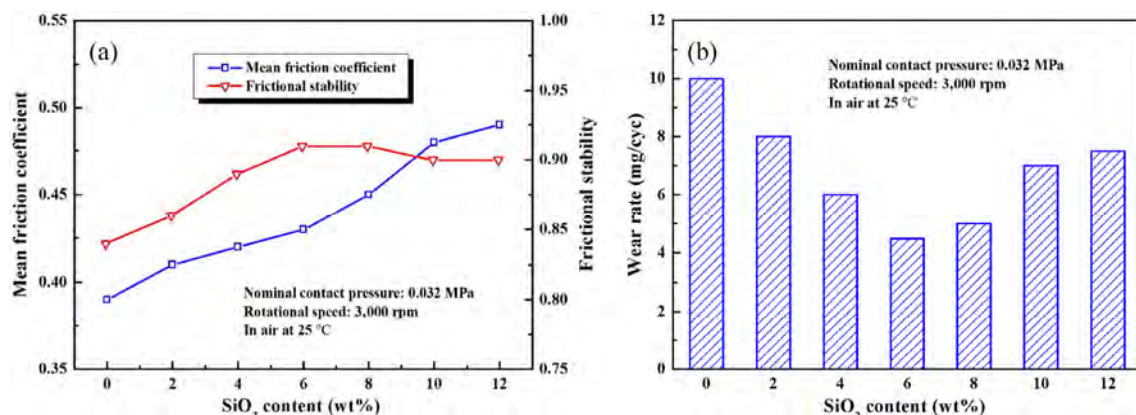

Fig. 4 Variations of (a) μ_{mean} and FS, and (b) wear rate with SiO$_2$ content.

Simultaneously, the broken and crushed SiO_2 particles exfoliated from the friction material brought about particle abrasion and eliminated adhesive wear resulting in improved frictional stability. Ceramic reinforcements in the form of particulates were widely incorporated in soft and ductile materials like copper to relieve the extent of wear deformation in the subsurface region. Consequently, the wear resistance of the friction material was considerably improved [14]. SiO_2 particulate could not react with the matrix and formed a weak bond with the matrix due to the slight wettability [12]. Therefore, the mechanical properties of the friction material dramatically deteriorated with SiO_2 content in excess of 6 wt%, leading to deterioration of the wear resistance.

Based on the above results, the chemical compositions of metal-matrix friction materials whose properties were tested under different conditions in sections below were obtained, as shown in Table 2. Friction materials were made by a powder metallurgy process that involved powder processing, pressure compaction, and pressure sintering. The source powders were weighed with the given proportion, mixed in a V-type mixer for 6–8 h and then cold compacted under a pressure of 350–500 MPa. The green compacts placed on the steel backing plates were sintered at 780–850 °C with a pressure of 1.5–2.5 MPa in a bell furnace saturated with hydrogen.

Table 2 Chemical compositions of metal-matrix friction materials.

Element	Cu	Sn	Fe	Graphite	MoS$_2$	SiO$_2$	CaCO$_3$	Al$_2$O$_3$	Others
Content (wt%)	43–60	5–7	5–8	5–7	6–8	5–7	5–7	3–5	6–8

3 Experimental results

3.1 Effects of nominal contact pressure on tribological properties

Figure 5(a) shows the influences of changes in the nominal contact pressure on μ_{mean} and FS. μ_{mean} significantly decreased with the increase of the nominal contact pressure, whereas FS slightly increased with the increase in the nominal pressure. The relationship between the nominal contact pressure and the wear rate is shown in Fig. 5(b). There was a slight increase in the wear rate with increasing nominal contact pressure up to 0.048 MPa after which a decreasing trend was observed.

The sliding movement occurred in very small areas at the asperities over time. The ruptures or breaks at the asperities and lubricants removed from the friction material brought about the generation of wear debris and friction layer, resulting in the steady-state friction characteristics and the decrease in the friction coefficient.

An increase in the load led to an increase in the wear rate. The wear behavior was attributed to the formation of the friction layers, mainly on the friction material. The friction force due to the ploughing action between the surfaces increased the temperature and broke the friction layers, resulting in an increase in the strength of the connections and metallic contact between the surfaces. This effect resulted in adhesion and increased the deformation at the surface layers, leading to further loss of the friction material. However, above that critical load, the accumulation

Fig. 5 Variations of (a) μ_{mean} and FS, and (b) wear rate with nominal contact pressure.

and compaction of wear debris and some constituents exfoliated from the friction material gave rise to the generation of a thicker and denser surface layer, providing wear protection [8].

3.2 Effects of vacuum pressure on tribological properties

Figure 6(a) shows the effects of varying vacuum levels on μ_{mean} and FS. In comparison with those in low vacuum, the friction material in air exhibited a higher friction coefficient and lower frictional stability, whereas the friction coefficient was slightly lower and the frictional stability was almost unchanged in high vacuum. The wear rate of the friction material under different vacuum pressures is summarized in Fig. 6(b). A significant increase in the wear rate in vacuum compared with that in air was observed.

The composition of the surface layer formed on the friction material was found to have a strong influence on the frictional response. At the friction speed of 3,000 rpm, a large quantity of frictional heat was generated during the course of friction. Frictional heat could lead to sufficiently high surface temperature that resulted in relatively thick oxides on the contacting surfaces in air. The oxide layer with hard particles and wear debris plowed the counterface, and as mentioned in the previous subsection, the fracture of the oxide layer was observed. This caused increased wear due to spalling of the oxide layer and more metallic contact between the interacting surfaces, resulting in a corresponding increase in the μ_{mean} and wear rate. In vacuum, it was difficult to regenerate the adsorbed film and oxide layer. Wear debris

dispersed in the course of milling and accumulated continually on the surface, forming a surface layer. The surface layer was rich in graphite and metal sulfides. The solid lubricant-rich layer, which provided improved wear resistance, stability, and reduced the friction coefficient could be produced between contact surfaces [8, 15].

On the other hand, in terms of the theory proposed by Bowden and Tabor, the friction resistance is derived from the formation of cold-weld junctions between surfaces [16, 17]. By assuming that all micro-contacts are plastically deformed and the stress is equal to the penetration hardness, σ_0, of the material, the friction coefficient can be written as

$$\mu = \frac{\tau_c}{\sigma_0} \tag{6}$$

σ_0 is a constant of the selected material, so the friction coefficient is determined by the shear strength τ_c of the surface layer. The shear strength of oxide layer is greater than that of the friction layer in the presence of softer inclusions [17]. Hence, the friction coefficient of the friction material in air was higher than that in vacuum.

3.3 Effects of ambient temperature on tribological properties

The space environment differs greatly from that on earth, as it contains a high vacuum, temperature that fluctuates from −120 to 150 °C due to the influence of sunlight, and harsh space irradiation [2]. Due to the susceptibility to cold-shortness, metal-metal pairs are
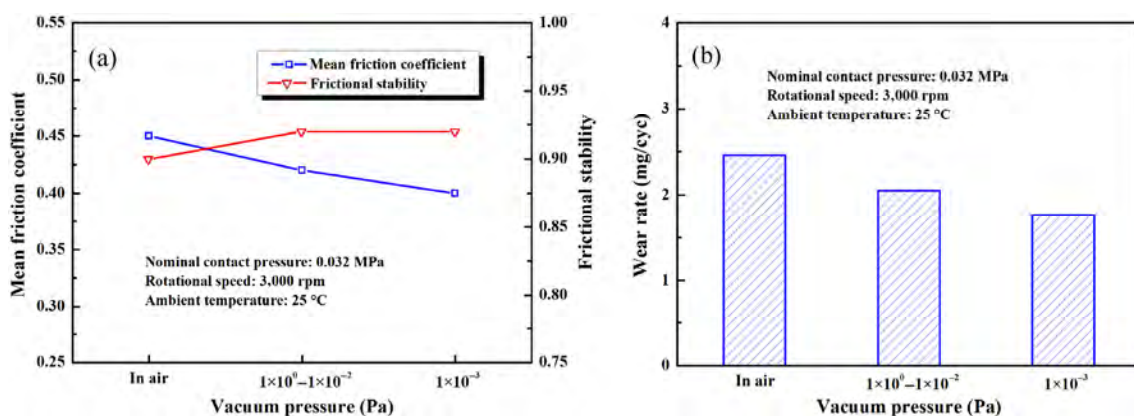

Fig. 6 Variations of (a) μ_{mean} and FS, and (b) wear rate with vacuum pressure.

seldom used at cryogenic temperatures [18]. Therefore, it is fundamentally important to investigate the effect of low temperature on the friction behaviors of the friction material.

Figure 7 shows the variations of μ_{mean} and FS with ambient temperature in vacuum. μ_{mean} was almost insensitive to the ambient temperature. Certain differences in FS are presented at different ambient temperatures. Nonetheless, the values of FS exceeded 0.9. This implies that the friction material exhibited the excellent tribological properties in a certain temperature range. During the friction process, the friction material containing high contents of non-metallic constituents could overcome the drawbacks of adhesion, cold-welding, and cold-shortness in high vacuum at a low temperature [8].

3.4 Wear mechanism

In air, due to the sufficient frictional heat, the continuous supply of O and occurrence of the tribo-oxidation promoted the formation of oxides during the friction process. The oxide layers were prone to spalling at low applied loads, whereas, the surface layers were formed and developed by trapping and compacting oxides, wear debris, and the powder on the constituents at certain applied loads. In addition, since the metal matrix wrapped up high contents of non-metallic ingredients it reduced the adhesive wear, cold-welding, and cold-shortness to a large extent.

As illustrated in Fig. 8, during the friction process, the hard three-body abrasives and peak asperities of the steel counterpart penetrated into the surface
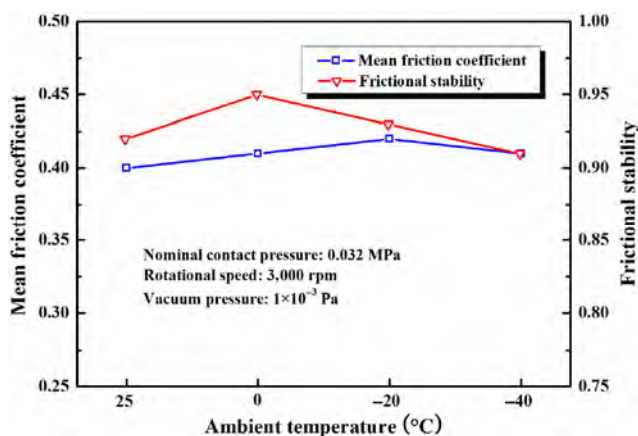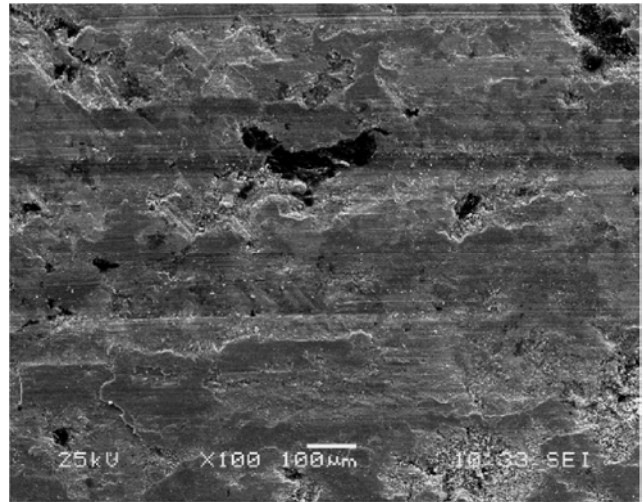

Fig. 8 SEM micrograph showing the worn surface with a number of furrows.

layer. Furrows were generated on the worn surface under the synergistic effects of normal pressure, the tangential stress, and frictional heat. This process is a manifestation of abrasive wear mechanisms.

As the friction process proceeded, subsurface microcracks were generated as seen in Fig. 9(b) due to the cyclic-plastic deformation. The microcracks then propagated to the worn surface where pits and spallation were found, as shown in Fig. 9(a). The fatigue wear was operative.

3.5 AO and UV erosion resistance

Table 3 presents mass loss rates of the friction material irradiated with atomic oxygen and ultraviolet rays, as well as their synergistic effects. During single AO exposure, a mass gain was detected, whereas mass loss was found upon exposures to single UV and AO+UV irradiation. It can also be seen that in AO+UV exposure, the mass loss was greater than that in single UV exposure. The mechanical bonding interface was formed among constituents of the friction material. In UV exposure, UV radiation might break those mechanical bonds with low binding energy and result in mass loss. In AO exposure, the friction material interacted with the incident AO beam, and the metal-matrix might be oxidized by interaction with oxygen atoms, resulting in the formation of a stable chemical reaction film on the surface. However, in AO+UV exposure, UV radiation might break bonds between the
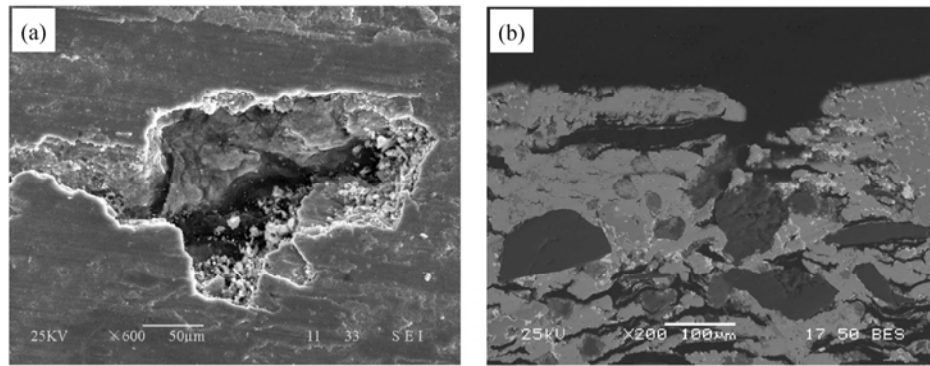

Fig. 7 Variations of μ_{mean} and FS with ambient temperature.

Fig. 9 SEM observations of (a) the worn surface and (b) the subsurface.

Table 3 Mass changes of the friction material under different exposure conditions.

Irradiations	Mass loss rate (mg/cm^2)
AO	−0.17
UV	0.22
AO+UV	0.35

chemical reaction film and the matrix, and accelerate the process of AO erosion. However, the results show that irradiations caused no significant mass loss of the friction material.

4 Present and potential applications

For reliably connecting and disconnecting two spacecrafts, the docking mechanism (Fig. 10(b)) has to provide shock absorption upon initial contact. The forced alignment of spacecrafts prior to locking spacecrafts together pushes them apart and produces positive separation [19]. To avoid a disastrous collision during berthing between two spacecrafts, the brake in the docking mechanism is required to execute the braking of the chaser spacecraft. In addition, it is

necessary to achieve the clutching operation in order that it can controllably release and separate two spacecrafts along a preselected separation axis [9]. When the machine is overloaded it results in failure of components such as shafts, burning of motors, and rupturing of gear teeth. The brake acts as an overload protector for safeguarding the docking mechanism.

As illustrated in Fig. 10(a), the friction pairs of the brake for docking mechanism consisted of friction discs made from powder metallurgy processed metal-matrix material and steel counterpart discs. M and FS of this brake were demonstrated by testing in air, vacuum, low temperature vacuum, and in environmental cycling, as shown in Table 4. As can be seen, the brake could recover the stable frictional torque characteristics under different environments. Vibrations created by the brake are often harmful and classical torque ripple values of 15% of frictional torque were typically attained. The FS values exceeded 0.9 in different environments, indicating that the brake could steadily execute braking operation, clutching operations, and overload protection during the berthing and disconnecting between spacecrafts. This brake
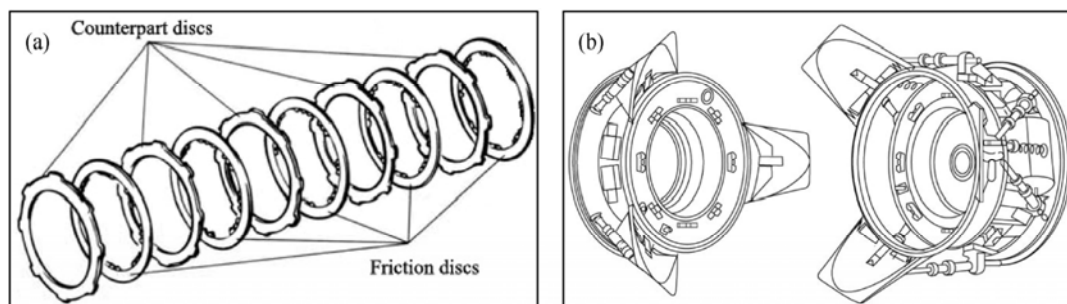

Fig. 10 Schematic view of (a) the friction pairs for (b) the docking mechanism.

Table 4 *M* and FS of the brake for docking mechanism under different conditions.

Types of operation	In air at 25 °C (before tribological testing in vacuum)		In vacuum at 25 °C		In vacuum at −20 °C	
	M (N·m)	FS	*M* (N·m)	FS	*M* (N·m)	FS
Braking operation	6.60–6.92	0.979	6.63–7.19	0.940	7.02–7.26	0.980
Clutching operation	6.62–7.01	0.974	6.51–6.92	0.973	6.66–6.97	0.980
Overload protection	37.57–42.34	0.968	36.32–38.30	0.973	38.63–39.76	0.989
Types of operation	In vacuum at −45 °C		In vacuum at 75 °C		In air at 25 °C (after tribological testing in vacuum)	
	M (N·m)	FS	*M* (N·m)	FS	*M* (N·m)	FS
Braking operation	6.88–7.38	0.958	6.83–7.50	0.934	6.73–6.88	0.989
Clutching operation	6.56–6.91	0.975	7.02–7.43	0.966	6.58–6.72	0.989
Overload protection	42.82–44.77	0.980	38.77–41.02	0.968	36.85–39.63	0.973

was successfully applied to the rendezvous and docking missions of "Shenzhou-8", "Shenzhou-9", "Shenzhou-10", "Shenzhou-11", and "Tianzhou-1" spacecrafts.

Fundamental studies on the properties of powder metallurgy processed metal-matrix materials under different conditions show that those materials could be of high interest for space related applications. Other potential space related applications for those materials include indexing mechanisms, robot arms, motor units, etc. Relevant work in those fields is also being conducted at Central South University.

5   Conclusions

Powder metallurgy processed metal-matrix friction materials hold great promise for space applications due to their outstanding comprehensive properties. In this paper, selected highlights of the study of the friction material at Central South University are presented. The important conclusions resulting from the above study as follows.

Cu-Sn alloys were selected to be the matrix phase, which provided strength, high temperature stability, oxidation resistance, and high thermal conductivity. There was an equilibrium mass of lubricant and abrasives achieved by tailoring the contents of the friction and lubricant components, at which point the friction material exhibited the desired level of coefficient of friction and excellent frictional stability with less wear loss. Chemical compositions of the friction materials were obtained based on experimental studies.

In comparison with those in low vacuum, the friction material exhibited higher μ_{mean} and lower FS in air, however μ_{mean} was slightly lower and FS remained almost unchanged in high vacuum, and a significant increase in the wear rate in vacuum compared with that in air was observed. μ_{mean} significantly decreased whereas FS slightly increased with an increase in *P*. A slight increase in the wear rate was observed with increasing *P* up to 0.048 MPa after which a decreasing trend was observed. The friction material containing high contents of non-metallic ingredients can reduce the adhesion, cold-welding, and cold-shortness to a large extent. The wear mechanism was a complex mixture of oxidation, abrasive wear, and fatigue wear. No significant mass loss of the friction material was observed under different irradiations.

A powder metallurgy processed metal-matrix friction material was successfully applied to the docking mechanism of the "Shenzhou" mission. Relevant works in other potential space related applications such as indexing mechanism and robotic arms are being conducted by our group.

References

[1] Roberts E W. Space tribology: its role in spacecraft mechanisms. *J Phys D: Appl Phys* **45**: 1–17 (2012)

[2] Fan X Q, Xue Q J, Wang L P. Carbon-based solid-liquid lubricating coating for space applications-A review. *Friction* **3**(3): 1–13 (2015)

[3] Jones W R, Jansen M J. Tribology for space applications. *Proc Inst Mech Eng Part J* **222**(8): 997–1004 (2008)

[4] Voevodin A A, Zabinski J S. Nanocomposite and nano-structured tribological materials for space applictions. *Compos Sci Technol* **65**(2): 741–748 (2005)

[5] Lv M, Zheng F, Wang Q H, Wang T M, Liang Y M. Friction and wear behaviors of carbon and aramid fibers reinforced polyimide composites in simulated space environment. *Tribol Int* **92**: 246–254 (2015)

[6] Hawthorne H M, Kavanaugh J. The tribology of space mechanism friction brake materials. *Canadian Aeronautics and Space Journal* **36**(2): 57–61 (1990)

[7] Baker F C, Favre E, Mozzon J M, Crausaz A, Jurients P. European robotic arm (ERA) manipulator joint system motor unit and tribological brake. *Proc 8th European Symposium* **438**: 111–118 (1999)

[8] Yao P P, Xiao Y L, Deng J W. Study on space copper-based powder metallurgy friction material and its tribological properties. *Adv Mater Res* **284**–**286**: 479–286 (2011)

[9] Xiao Y L, Yao P P, Zhou H B, Zhang Z Y, Gong T M, Zhao L, Zuo X T, Deng M W, Jin Z X. Friction and wear behavior of copper matrix composite for spacecraft rendezvous and docking under different conditions. *Wear* **320**: 127–134 (2014)

[10] Yao P P, Xiao Y L, Zhou H B, Jin Z X. Tribological and mechanical properties of materials for friction pairs used to space docking. *Adv Mater Res* **538**–**541**: 1929–1934 (2012)

[11] Asif M, Chandra K, Misra P S. Characterization of iron based hot powder brake pads for heavy duty applications. *Int J Mech Mater Eng* **8**(2): 94–104 (2012)

[12] Xiong X, Chen J, Yao P P, Li S P, Huang B Y. Friction and wear behaviors and mechanisms of Fe and SiO_2 in Cu-based P/M friction materials. *Wear* **262**: 1182–1186 (2007)

[13] Österle W, Dmitriev A I. The role of solid lubricants for brake friction materials. *Lubricants* **4**(1): 1–22 (2016)

[14] Tjong S C, Lau K C. Tribological behaviour of SiC particle-reinforced copper matrix composites. *Mater Lett* **43**: 274–280 (2000)

[15] Kato H, Takama M, Iwai Y, Washida K, Sasaki Y. Wear and mechanical properties of sintered copper-tin composites containing graphite or molybdenum. *Wear* **1**–**6**: 573–578 (2003)

[16] Bowden F P, Tabor D. *The Friction and Lubrication of Solids*, *Part 2*. Oxford (UK): Clarendon, 1964.

[17] Popov V L. *Contact Mechanics and Friction, Physical Principles and Applications*. Springer, 2010.

[18] Wigley D A. *Materials for Low-temperature Use*. Oxford (UK): Oxford University Press, 1978.

[19] Fehse W. *Automated Rendezvous and Docking of Spacecraft*. Cambridge (UK): Cambridge University Press, 2003.

Yelong XIAO. He received his master degree in materials science and engineering in 2012 from Central South University, Changsha, China. He is currently a Ph.D. student at the same university. His research interests include the design, preparation, and characterization of metal matrix friction materials.

Pingping YAO. He received his master and Ph.D. degrees in materials science and engineering from Central South University, Changsha, China. He joined Powder Metallurgy Research Institute at Central South University from 1992. His current position is a professor, the supervisor of Ph.D. students. His research areas cover the friction materials, anti-friction materials, and anti-wear materials, and their mechanical and tribological performances, and their applications in spacecraft, aircraft, high-speed trains and so on.

RESEARCH ARTICLE

Galvanically induced potentials to enable minimal tribochemical wear of stainless steel lubricated with sodium chloride and ionic liquid aqueous solution

Tobias AMANN[1*], **Felix GATTI**[1,2], **Natalie OBERLE**[1], **Andreas KAILER**[1], **Jürgen RÜHE**[3]

[1] *Fraunhofer Institute for Mechanics of Materials IWM, Woehlerstr. 11, Freiburg 79108, Germany*

[2] *Institute for Macromolecular Chemistry, University of Freiburg, Freiburg 79104, Germany*

[3] *IMTEK - Department of Microsystems Engineering, University of Freiburg, Georges-Koehler-Allee 103, Freiburg 79110, Germany*

Abstract: The effect of galvanically induced potentials on the friction and wear behavior of a 1RK91 stainless steel regarding to tribocorrosion was investigated using an oscillating ball-on-disk tribometer equipped with an electrochemical cell. The aim of this investigation is to develop a water-based lubricant. Therefore 1 molar sodium chloride (NaCl) and 1% 1-ethyl-3-methylimidazolium chloride [C_2mim][Cl] water solutions were used. Tribological performance at two galvanically induced potentials was compared with the non-polarized state: cathodic potential-coupling with pure aluminum- and anodic potential-coupling with pure copper. Frictional and electrochemical response was recorded during the tests. In addition, wear morphology and chemical composition of the steel were analyzed using scanning electron microscopy (SEM) and X-ray photoelectron spectroscopy (XPS), respectively.

The galvanically induced cathodic polarization of the stainless steel surface results in electrochemical corrosion protection and the formation of a tribolayer. Cations from the electrolyte (sodium Na^+ and 1-ethyl-3-methylimidazolium [C_2mim]$^+$) interact and adhere on the surface. These chemical interactions lead to considerably reduced wear using 1 NaCl (86%) and 1% 1-ethyl-3-methylimidazolium chloride [C_2mim][Cl] (74%) compared to the nonpolarized system. In addition, mechanical and corrosive part of wear was identified using this electrochemical technique. Therefore this method describes a promising method to develop water-based lubricants for technical applications.

Keywords: sliding wear; tribochemistry; potential controlled friction and wear; galvanic coupling; ionic liquids; tribolayer formation

1 Introduction

Friction and wear occurs in mechanically driven technical systems and causes enormous economic costs, which are estimated up to ≈ 6% U.S. gross national product [1]. In combination with the possibility to diminish the environmental impact of tribological applications, it is inevitable to increase the energy efficiency and durability of their components in sliding or rolling contacts [2–4]. These challenges have been identified and are reflected in current research, which focusses increasingly on energy efficiency, sustainability and "green" tribology [5]. Therefore current research topics in the field of tribology consist in the development of water-based lubrication [6] and the reduction of friction losses to increase the energy efficiency of technical systems [7]. However, there is a common disregard of tribochemical effects in friction

---

and wear, though especially rolling and sliding bearings in machines and systems that are exposed to environmental influences or only lubricated by surrounding media (e.g., pumps) are subjected to increased corrosive wear. For engineering materials it is a common scenario to be exposed simultaneously to mechanical damage and electrochemical corrosion [8]. Under these conditions complex tribochemical reactions and surface interactions take place, which lead to corrosive wear [9]. As a consequence, the sliding surfaces of bearings and mechanical seals may be severely damaged after only a short period of use [10]. For the affected technical equipment, devices, and machines there is a need to reduce the damage caused by tribochemical reactions to increase the service life and durability.

To prevent tribocorrosion, corrosion resistant materials, coatings, or lubricants are used. Since 2001 ionic liquids (ILs) have been identified as novel substances with promising tribological properties as lubricants [11–13] and as additives [14–18]. In addition, it has been reported that ILs can be used at electrified interfaces to improve friction and wear [19, 20]. Li et al. have recently shown that ionic liquids even form solvation layers on surfaces that are strongly influenced by electric potentials and may effectively prevent solid-solid contact in nanotribological contacts enable extremely low friction coefficients [20]. But also other surfactant containing aqueous solutions can be used to actively influence friction and wear by the application of electrochemical potentials [21–24]. These investigations were conducted using an external voltage generator. This experimental approach has been frequently published and is called potential controlled friction (PCF) [25, 26]. The relevant surface mechanisms that influence the tribochemical behavior are variation of electric double layers [27] electro-kinetic effects, chemisorption, and physisorption of surfactants and chemical reactions [28].

Fundamental investigations on the nanoscale revealed that dynamic superlubricity can be realized accompanied by the elimination of wear [29]. Atomic force microscopy (AFM) studies using surfactant micelles between silica surfaces showed liquid superlubricity [30]. Realizing this state of vanishing friction and wear on the macroscale would come along with high energy

savings and increased lifetime of technical applications. Due to these findings bridging the gap between concepts of superlubricity, wearless sliding, and friction control on the microscopic and macroscopic level are the current challenges in this research field [31]. The hypothesis of this work is based on two tribological mechanisms which arise due to the interaction of ionic molecules on a polarized interface. On the one hand the steel surface is electrochemically protected against corrosion reactions [32, 33]. On the other hand the polarized surface in combination with ionic molecules can lead to the formation of very stable interfacial layer as it was shown using AFM-measurements [20]. The molecular orientation of the ILs strongly influence the tribological behavior [34]. Moreover, it was found that Na^+ ions enhance molecular ordering of water and lead to longer mechanical relaxation times [35]. Even the adhesion and friction characteristics can be controlled using nanoparticulate polymer brushes [36]. Ionic liquids have already been investigated as additives in water lubrication in combination with ceramics [37–40]. Furthermore using a protic ionic liquid ultra-low friction was achieved at the water-lubricated sapphire–stainless steel interface [41]. In addition, it was found that the running-in process reduces with increasing IL/water concentration which is accompanied with more pronounced adhesive and corrosive wear [39]. From a chemical point of view it must be noticed that 1-ethyl-3-methylimidazolium chloride [C2mim][Cl] ionic liquid is hydrophilic and can cause decomposition into the HCl in presence of water and humidity, which has detrimental effect towards metallic tribo-surfaces [11]. As a result, since last five years halogen-free ionic liquids are gaining significant attention [42]. The miscibility of IL with water is strongly affected by the composition of the anion [43]. For example ILs with chloride $[Cl]^-$ are complete miscibility with water whereas $[PF_6]^-$ containing ILs are almost total immiscible. In addition, the miscibility gets worse with increasing alkyl chain length of the cation. The formation of electric double layers, tribochemical reactions, chemisorption, and interfacial electro-kinetic effects are identified as the most important mechanisms which induce modified friction and wear behavior in electrochemically affected tribological systems and have been discussed elsewhere

[20, 27, 28, 44, 45]. In the ionic liquid solution, cations adsorb along the surface at negative potentials and arrange into ion/ion pair layers near the interface [44, 45]. This arrangement is more pronounced at higher polarization [44]. Especially 1-ethyl-3-methylimidazolium [C_2mim] with its rigid and inflexible side chains is able to sternly adsorb with a high packaging density within the interfacial (innermost) layer and the transition zone [25]. But it must be noticed that water can strongly change viscosity, polarity, and surface tension in contrast to the pure IL [46]. Consequently, understanding surface interactions, tribochemistry and electro-chemical phenomena and ordering of molecules on the tribological interface are identified as key factors to realize tribological applications using aqueous lubricants [32]. Both factors, the good miscibility with water and the capability to adsorb with a high packaging density were decisive that 1-ethyl-3-methylimidazolium chloride ionic liquid [C_2mim][Cl] was used for this investigation.

The aim of this study is to influence these two mechanisms in macroscopic tribological contacts to control chemical (electrochemical corrosion protection) and mechanical (formation of tribolayer) wear.

Since external electrical supplies are normally too difficult to apply in real technical systems, we did not induce electrochemical potentials externally but simply used galvanic couplings of two suitable materials. In analogy to galvanic corrosion protection techniques using sacrificial anodes, the galvanic coupling relocates electrochemical reactions to the less noble metal surface. This offers the opportunity to protect tribological contacts against accelerated chemical wear [47]. In a chloride environment for example there is a rapid passive film breakdown due to hydrolysis [48, 49]. Recently published own work using ILs [50], aqueous solutions of ILs [51], and sodium chloride [52, 53], we showed how strongly electrochemical potentials, applied in a three-electrode configuration [54], can improve friction, wear, and reduce tribocorrosive reactions. The Effect of potential in tribocorrosion of passive materials such as stainless steel has been previously studied and some degradation mechanisms have been already proposed [55, 56]. In addition, Vieira et al. found that during rubbing, a galvanic coupling between the worn and unworn area are generated

due to the mechanical removal of the passive layer and proposed a galvanic model for describing this effect [57].

The approach of this work is to design a tribosystem, in which tribochemical mechanisms and conditions are most favourable. In this article we show that electrochemical potentials can be generated by combining metals with significantly different corrosion potentials (galvanic coupling) to reach minimal wear in sliding surfaces in aqueous solutions with sodium chloride and an ionic liquid.

2 Methods and materials

Friction tests were carried out with a reciprocating ball-on-disk tribometer (diameter ball: 12.7 mm, Co. Optimol Instruments SRV-4) using two different electrolytes (Fig. 1). The test parameters were set to 10 N normal force, 1 mm stroke, and 20 Hz oscillation frequency at room-temperature. Each test was performed three times with test duration of 1.0 h.

A stainless steel disk (Sandvik Bioline 1RK91TM, precipitation hardened, 12%Cr-9%Ni-4%Mo-2%Cu, ASTM A564, UNS S46910) with a silicon carbide (SiC) ball as counter body were used as tribological test samples. 1RK91 was used because it combines the properties of ordinary austenitic stainless and low alloyed ferritic steels. The arising galvanic potential during the tribological tests, due to different material combination, was measured using a potentiostat with a reference electrode (Ag/AgCl). To measure the
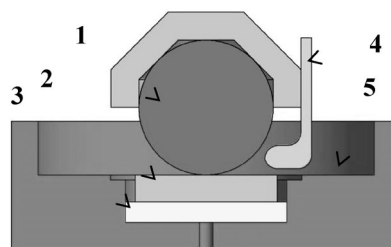

Fig. 1 Sketch of the electrically insulated test setup with ball-on-disk geometry. 1. Reciprocating SiC ball; Galvanic cell due to different material combinations: 2. Upper stainless steel disk (1RK91 in contact with SiC ball); 3. Used materials for lower disk: copper (Cu), aluminium (Al), and teflon (PTFE); 4. Ag/AgCl-reference electrode to measure the induced electrochemical potential; 5. Electrolyte reservoir filled with lubricant (1 molar sodium chloride (NaCl) and 1% imidazolium-based ionic liquid [C_2mim][Cl]).

generated galvanic potential the lower disks (galvanic cell) was connected as counter electrode. The contact area with electrolyte was 250 mm² and with the galvanic coupled metal 240 mm². To form a galvanic cell pure copper (Cu) as more noble and pure aluminum (Al) as less noble material than 1RK91 was used with a contact area with electrolyte of 210 mm². Friction tests using PTFE were performed as reference without galvanic coupling due to electric insulation of the material. Surface profiles (Fig. S1 in Electronic Supplementary Material (ESM)), topographies (Fig. S2 in ESM), characteristics (Table S1 in ESM) and chemical composition (Table S2 in ESM) of the used samples are included in the supporting information. As electrolytes aqueous solution (deionized water) of 1 molar sodium chloride (NaCl) and 1 wt% (1% by weight) of the imidazolium-based ionic liquid [C_2mim][Cl] (Co. Iolitec, Fig. S3, Table S3) were used. After each friction test the ball and disk were analyzed using color 3D Laser Microscope (VK-9700K, Co. Keyence) to evaluate and quantify wear. Raman microscopy spectra of the wear track to analyze oxidation products were measured using an InVia Renishaw Ramanscope system. The measurements were carried out in air using a He-Ne laser with a wavelength of 532 nm. All spectra were taken three times using a 50× microscope objective, an integration time of 40 s at a laser intensity of 50%. The spectral window was between 100 and 1,600 cm⁻¹. In addition, scanning electron microscopy (Hitachi S3400N, Type II) and XPS-analysis (X-ray photoelectron spectroscopy, Leybold MAX 100; argon ion sputtering with sputter rate: 2.5 nm/min; 1 kV; 500 nA; diameter test point ~ 200 μm) was used to analyze the wear pattern and the chemical composition of the tribolayer on the 1RK91 material.

3   Results and discussion

3.1   Induced galvanic potential

Self-corrosion potentials of Al (–806 mV vs. Ag/AgCl) is about 600 mV more negative that of Cu (–210 mV vs. Ag/AgCl) as shown in Fig. 2(a). By coupling 1RK91/copper (Cu) and 1RK91/aluminum (Al) nearly the same open circuit potential on the stainless steel is formed as for pure Al and Cu (Fig. 2(a)). In a galvanic cell, the base metal is the anode and the
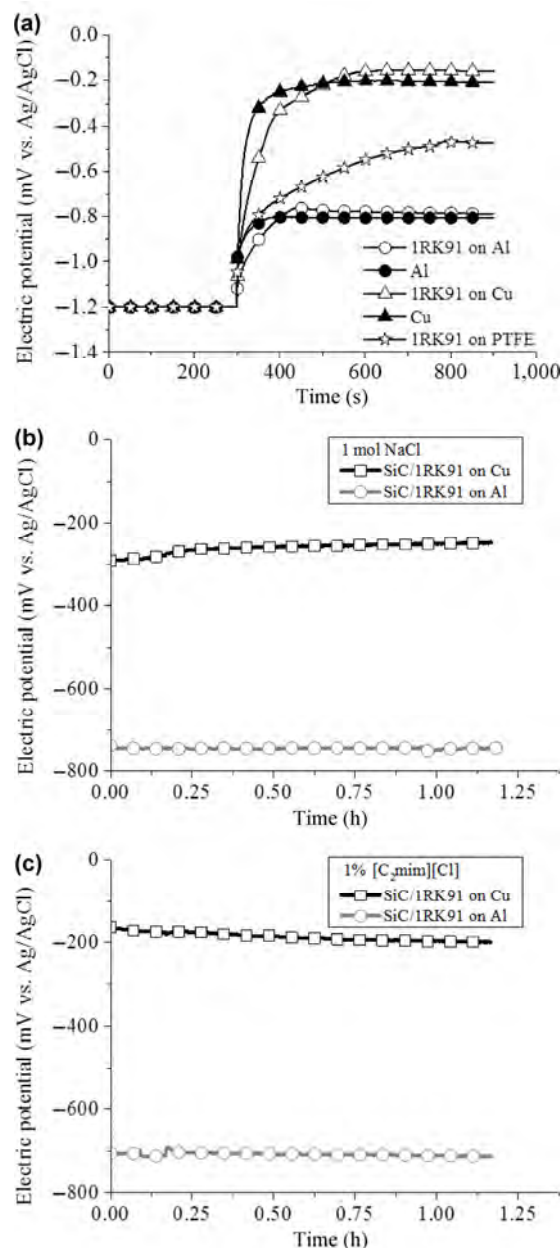

Fig. 2   Electrochemical investigations: (a) Self-corrosion potentials of Al and Cu (filled symbols) and open circuit potential using different material combinations in 1 mol NaCl solution were steel 1RK91 was set as working electrode (unfilled symbols). Induced galvanic potential during tribological test using 1 molar NaCl (b) and 1% [C_2mim][Cl] (c) aqueous solution during tribological test (copper and aluminum contacted as working electrode).

more noble the cathode. This polarization results in an accelerated corrosion of the anode. Due to material combinations different galvanic potentials form: In the material combination 1RK91/Copper (Cu) the stainless steel acts as the anode, whereas in contact with Aluminum (Al) it is set to the cathode. Without

galvanic coupling an electric potential of –470 mV vs. Ag/AgCl develops and according to the coupling material 1RK91 shows a cathodic (Al) and anodic (Cu) polarization. Figure 2(b) illustrates the development of the potential during the friction test using 1 molar NaCl as electrolyte. In contrast to measurement shown in Fig. 2(a) the electric potential was measured using the coupling material (Al, Cu) as working electrode. The arising potential is quite stable during the whole test with a value of –250 mV for 1RK91/Cu and –750 mV vs. Ag/AgCl for 1RK91/Al and shows nearly the same value as shown in Fig. 2(a). Nearly the same values are measured using 1% [C$_2$mim][Cl] (1RK91/Cu: –200 mV and 1RK91/Al: –715 mV vs. Ag/AgCl, Fig. 2(c)). The absolute difference in the arising anodic and cathodic potential, due to varied material combination, is about ±300 mV for both electrolytes.

3.2 Friction tests

The results of the friction tests are illustrated in Fig. 3. The tribotests were reproduced three times and showed a good reproducibility. The highest coefficient of friction (COF) was measured at cathodic polarization (1RK91/Al), whereas at nonpolarized state (1RK91/PTFE) the lowest COF was found for both electrolytes. In contrast to cathodic polarization there is a running-in behavior observable at anodic and nonpolarized condition within in the first 20 min. The COF from the friction diagrams (Fig. 3(a),(b)) were integrated to calculate the friction work (Fig. 3(c), Table S4 in ESM). There is nearly no difference between the two electrolytes, but the material combination strongly influences the friction work. The combination 1RK91/Al leads to the highest friction work, but there is also a slightly increase, when the combination 1RK91/Cu was tested. Consequently, compared to the non-polarized system at (1RK91/PTFE), cathodic polarization (1RK91/Al) resulted in a 45% increase of friction with NaCl and 36% with the ionic liquid. Anodic polarization (1RK91/Cu) led to an increase of 15% and respectively 2%.

3.3 Wear analysis

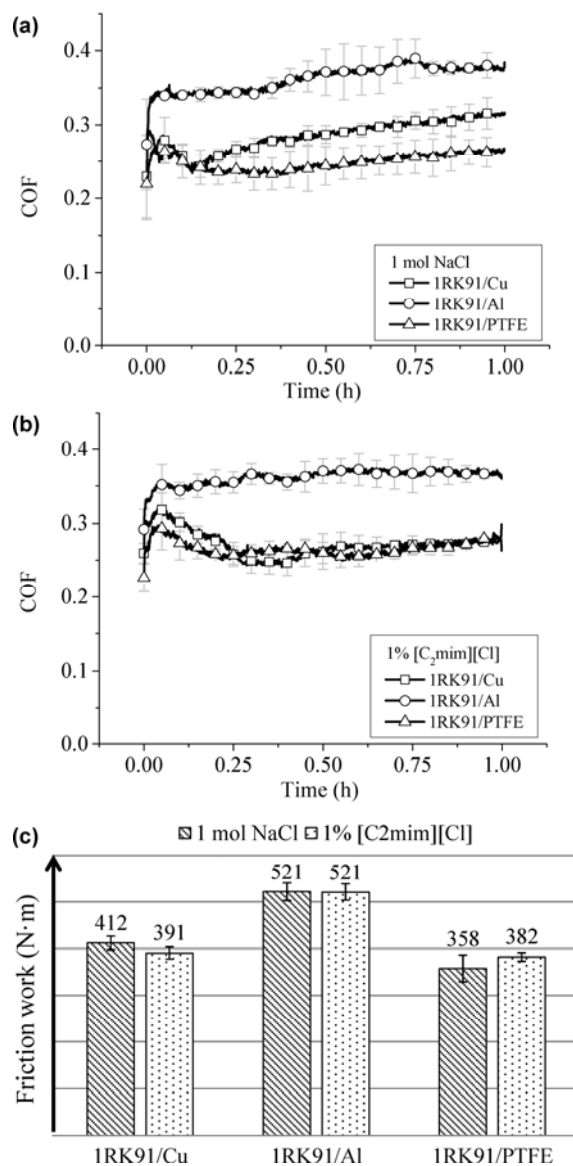Figure 4 illustrates the wear volume of the 1RK91 disk and the SiC ball after friction test.

Fig. 3 Mean value of the coefficient of friction using different material combinations with 1 molar NaCl (a) and 1% [C$_2$mim][Cl] (b) as electrolyte. (c) Overview of the mean value of the friction work using different material combinations with 1 molar NaCl and 1% [C$_2$mim][Cl] as electrolyte.

Obviously, the polarization of the disk has a strong impact on the wear volume: At cathodic potential, when tribocorrosion processes are suppressed, the total wear volume of ball and disk is decreased by 86% in 1 molar NaCl and 74% in 1% [C$_2$mim][Cl], in relation to the non-polarized system. In contrast, under anodic potential with accelerated corrosion conditions, severe wear occurs, at which the wear volume is increased by 69% in NaCl electrolyte and 23% in [C$_2$mim][Cl] solution compared to 1RK91/PTFE.

In addition, the wear volume is also strongly affected by the electrolyte. Using 1% [C$_2$mim][Cl] the wear volume was clearly reduced for the material combinations 1RK91/PTFE (48%) and 1RK91/Cu (62%), whereas no further decrease of wear volume was observed at cathodic polarization. The wear volume of ball and disk is nearly equal without polarization. In contrast, wear volume ratio of ball and disk decreases at cathodic polarization (~0.4) and increases at anodic potential using 1% IL (Fig. 4(c)). The values of the wear volume are listed in Table S5 in ESM and the images of wear track are illustrated in Fig. S4 in ESM (ball) and Fig. S5 in ESM (disk). Due to solid material contact during friction test wear grooves in sliding direction arise and therefore roughness increases for all combinations (Fig. S6) in ESM. Hence the friction and wear properties do not depend on a surface smoothing effect.
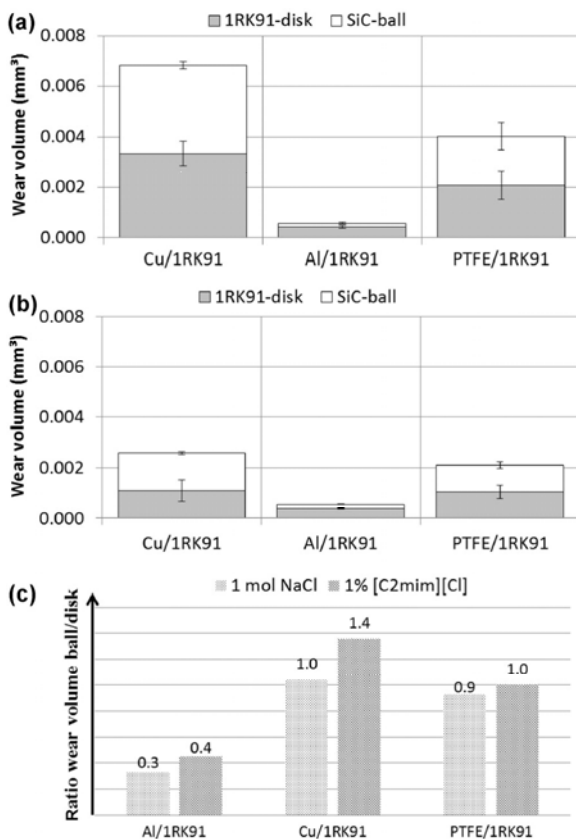

Fig. 4 Wear volumes of ball and disk after friction test with three different galvanic coupling elements (copper, aluminium and Polytetrafluoroethylene) in contact with steel 1RK91 disk using two different electrolytesafter tribotest (10 N, 20 Hz, RT, 1 mm, 1 h): (a) 1 molar NaCl solution; (b) 1% [C$_2$mim][Cl]; (c) Ratio of wear volume of ball and disk.

Within the dynamic corrosion model published by Iwabuchi et al. [58, 59] the wear volume W is composed of the mechanical wear M_0, static corrosion volume C_0 and the synergistic factor ΔW, where W_d is called the dynamic corrosion factor:

$$W = M_0 + C_0 + \Delta W = M_0 + W_d \tag{1}$$

Due to sliding friction protective surface layer on the stainless steel gets destroyed and accelerated corrosion and wear mechanisms of fresh metal surface occur. Based on this model and the assumption that corrosive processes are completely suppressed it is possible to quantify the corrosive attack during these friction tests. Wear at friction tests without polarization (1RK91/PTFE) is composed according to Eq. (1) whereas wear after test at cathodic polarization (1RK91/Al) can be regarded as the pure mechanical wear. The dynamic corrosion factor generates from the difference in wear between these two testing conditions. As shown in Fig. 5(a) mechanical wear (M_0) is the same using both solutions but the proportion of mechanical wear to the dynamic corrosion factor (M_0:W_d) is much lower using 1% IL (1:5) than 1 mol NaCl (1:13). This means that the dynamic corrosion can be strongly reduced using ionic liquid in contrast to sodium chloride. Regarding the amount of cathodic and anodic polarization based on the OCP of 1RK91 a correlation with total wear volume can be found (Fig. 5(b)).

In addition, wear analysis of the 1RK91 disks using scanning electron microscope were performed after tribotest (Fig. 6). The metallic surface and horizontal wear tracks in sliding direction are clearly visible after friction test at anodic polarization and no corrosion products are detectable. At nonpolarized condition there is little change on the surface visible after friction test and at cathodic polarization the worn surface appears quite different. It can be assumed that these changes are caused by tribochemical reactions.

3.4 Investigation of tribolayer

The worn surface was furthermore analyzed using Raman-spectroscopy to identify tribochemical reaction products. Oxides were identified based on literature data of different steel materials [60–63]. Steel 1RK91 shows Raman signals for Cr-O (800 cm^{-1}), FeOOH
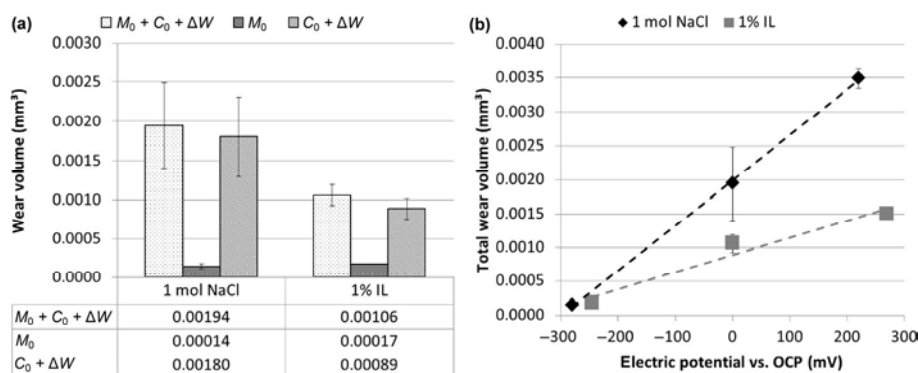
Fig. 5 (a) Determination of wear components based on dynamic corrosion model; (b) Correlation of total wear volume and galvanically induced electric potential.
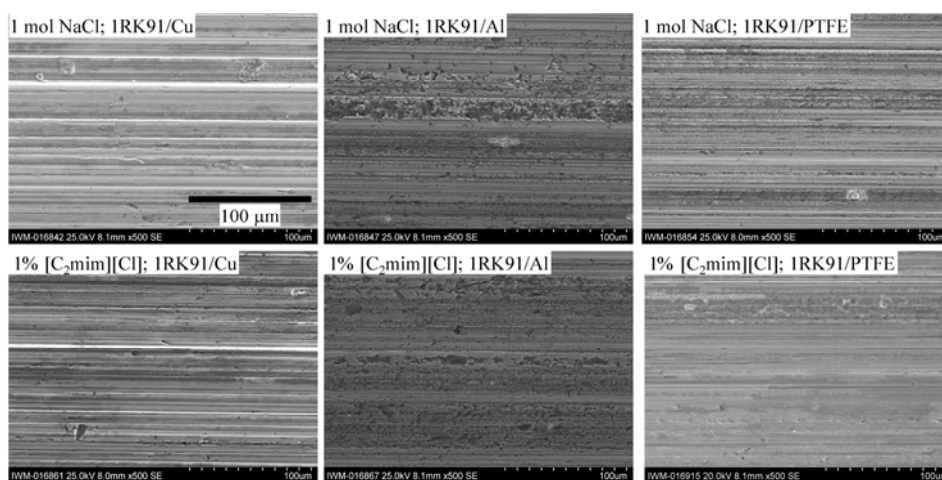

Fig. 6 Wear analysis of the 1RK91 disks using scanning-electron-microscope after tribotest (10 N, 20 Hz, RT, 1 mm, 1 h) at different polarizations.

(645 cm^{-1}) and Cr$_2$O$_3$ (540 cm^{-1}) in its unworn state. As listed in Table 1 and in accordance with the SEM images (Fig. 6) no further oxidation products were detected on the worn surface at anodic polarization. In contrast, without polarization more oxidation products are found on the wear track whereat cathodic polarization results in the strongest tribochemical changes as additional Fe$_2$O$_3$ is detected. The Raman spectra are given in Fig. S7 in ESM.

Using XPS-analysis the findings from Raman-spectroscopy were verified and, in addition, the thickness and chemical composition of the tribolayer was investigated. Therefore the atomic concentration of different elements and molecules were measured in relation to the sputter depth using 1% [C$_2$mim][Cl] (Fig. 7). 1RK91 exhibits an oxide layer of ≈150 nm. After friction test at cathodic polarization (1RK91/Al)

a tribolayer of ≈800 nm was found consisting of carbon compounds (≈25 nm), chromium oxide (≈500 nm), and iron oxide (≈800 nm). At oppositional conditions with material combination 1RK91/Cu the anodic potential leads to a formation of a ≈350 nm thick tribolayer on the wear scar assembled of carbon compounds within the first ≈100 nm and chromium oxide till ≈350 nm without detection of iron oxide. Especially the content of chromium oxide and iron oxide strongly differs between anodic and cathodic conditions. Nearly the same thickness (≈350 nm) and chemical composition of the tribo-layer is detected without using an induced electrochemical potential (1RK91/PTFE). The only difference to anodic polarization is the higher amount of iron oxide in the tribo-layer at nonpolarized condition (Fig. 7(e)). Therefore it can be concluded, that in the case of cathodic polarization by aluminum, a

Table 1 Raman signals (cm^{-1}) measured in the wear track of the 1RK91 disks after tribotest.

Oxides	1 mol NaCl			1 % [C$_2$mim][Cl]		
	1RK91/Cu	1RK91/Al	1RK91/PTFE	1RK91/Cu	1RK91/Al	1RK91/PTFE
Fe$_2$O$_3$	—	490; 390; 280; 220	—	—	500	—
FeOOH/Fe$_3$O$_4$	—	1320	1350	1345	1330	1345
FeOOH	—	—	725	—	—	740
Cr$_2$O$_3$	—	680	545	—	690	540
Cr-O	800	—	925; 875	890	—	—
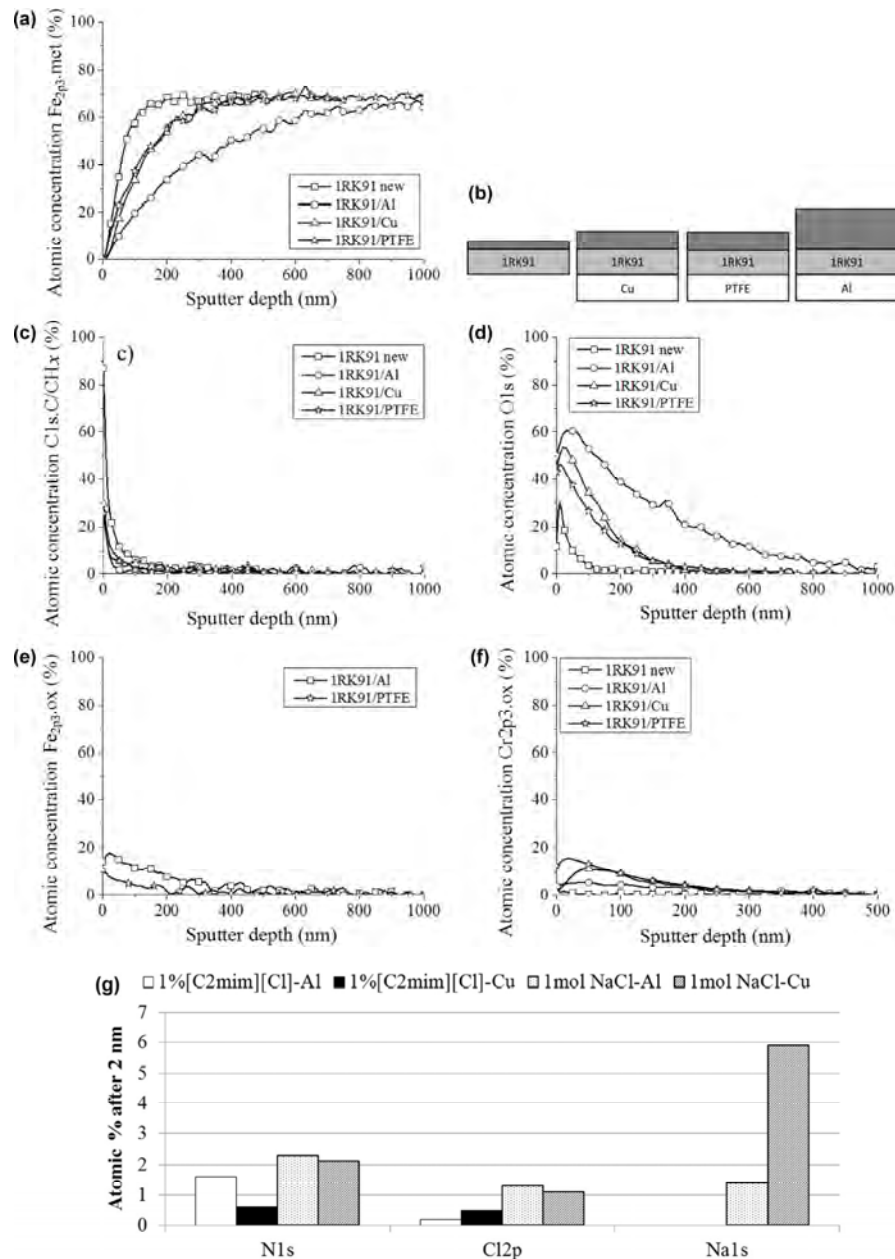
Fig. 7 XPS-analysis (sputter rate ≈10 nm/min) of new 1RK91 material and wear scars on the disks after tribotest (10 N, 20 Hz, RT, 1 mm, 1 h) using [C$_2$mim][Cl] with the different material combinations, e.g. polarizations: (a) metallic Fe$_2$p$_3$; (b) schematically illustration of tribo-layer thickness on 1RK91 after tribo-test; (c) C1s.C/CHx; (d) O1s; (e) Fe$_2$p$_3$ oxide; (f) Cr$_2$p$_3$ oxide; (g) result of high resolution analysis of the first 2 nm.

stronger stabilization of the oxide layer predominates, whereby the formed oxide, which does not oxidize back, protects the surface more strongly from wear. Due to the way of galvanic coupling different tribochemical reactions occur during friction test on the anode and cathode. Combination of steel and copper causes an anodic polarization of the steel which is accompanied by high wear due to accelerated corrosion reactions. The generated oxides are permanently removed by friction so that no wear products were found on the wear track. The same tribochemical reactions arise in the nonpolarized state when coupling steel with PTFE with the difference that the corrosion isn't externally accelerated by an electrochemical potential. In this case only a small amount of oxidation products was found in the wear track (complete depth profiles including all elements are illustrated in Figs. S8 and S9 in ESM).

Additional XPS-measurements at high resolution constrain that both the cation and anion participated in the tribo-chemical thin film formation within the first 2 nm (Fig. 7(g)). The same result was found for the 1 mol NaCl solution as Na and Cl was detected on the tribolayer.

In contrast, if 1RK91 is galvanically coupled with aluminum the steel surface should be electrochemically protected against corrosion. Surface analyses reveal that tribochemical reactions also occur on the wear track forming oxide layers, though the reaction kinetics are strongly retarded and therefore the wear volume is quite low. But it must be noticed that the corrosion resistance of the galvanically contacted lower aluminum disc is greatly reduced by aqueous salts, particularly in contact with dissimilar metals. This leads to pitting corrosion of the aluminum. The galvanically induced cathodic polarization of the steel surface results in electrochemical corrosion protection and the formation of a mechanically stable tribolayer.

4   Conclusions

The global challenge concerning friction and wear consists in the development of eco-friendly, sustainable and energy efficient lubricants. The problems by evolving such tribological systems, especially water-based lubricants, are complex tribochemical reactions resulting in corrosion and accelerated wear. Moreover,

pure water is inapplicable for tribological systems due to its low viscosity and high corrosivity. Application of external electrochemical potentials can be utilized to influence the corrosion behavior, tribochemical reactions, and adsorption of ions on the surface. The aim of this investigation was to explore and evaluate the electrochemical effects of metallic material combinations on tribocorrosive wear using galvanically induced potentials. Therefore we used a stainless steel material in metallic coupling with Cu and Al to induce different electrochemical potentials, which we tested in an oscillating friction mode in two different electrolytes. Galvanically induced cathodic potentials in tribological tests have proven to be a valuable method to significantly reduce wear in combination with water-based lubricants compared to the non-polarized system. In conclusion, it was observed that the cathodic potential, which arises in an adapted galvanic cell, can be utilized to considerably reduce wear using 1 molar NaCl (86%) and 1% [C_2mim][Cl] (74%) electrolyte compared to the non-polarized system. In contrast, the galvanic coupling of stainless steel 1RK91 with the more noble copper results in an anodic polarization of the stainless steel leading to clearly enhanced wear. In addition, the electrolyte also affects the wear volume and the impact of galvanic potential: while NaCl solution leads to higher wear, at which mainly tribocorrosive mechanisms are relevant, the addition of an ionic liquid leads to potential-driven chemisorption effects that further reduce wear. It was found that mainly corrosive wear and not mechanical wear mechanisms are relevant in this tribological system. Therefore this technique is very promising to improve the tribological behavior of water-lubricated systems for technical applications. It is also noticeable that the galvanic potential is stable over the whole test duration. In contrast, friction work is increased for both polarizations compared to the non-polarized system, but isn't affected by the type of electrolyte. It is assumed that at negative potentials cations arrange into ion/ion pair layers with a high packaging density along the interface. XPS-measurements reveal that at cathodic polarization a thick tribolayer is formed and that both the cation and anion participated in the tribo-chemical thin film formation within the first 2 nm.

Acknowledgement

Electronic Supplementary Material: Supplementary material is available in the online version of this article at https://doi.org/ 10.1007/s40544-017-0198-y.

The surface characteristics and material compositions of the used materials are described in Figs. S1–S3 and Tables S1–S3. The corresponding wear values of Figs. 4–6 are listed in Tables S4 and S5. The wear patterns using laser scanning microscope are illustrated in Figs. S4 and S5. The resulting surface roughness on wear scar is shown in Fig. S6. The Raman spectra are given in Fig. S7. The complete profiles of XPS analysis of all detected elements on 1RK91 before and after tribological test are shown in Figs. S8 and S9.

References

[1] Persson B N J. *Sliding Friction*. Berlin, Heidelberg (Germany): Springer, 2000.

[2] Tzanakis I, Hadfield M, Thomas B, Noya SM, Henshaw I, Austen S. Future perspectives on sustainable tribology. *Renew Sustain Energy Rev* **16**(6): 4126–4140 (2012)

[3] Holmberg K, Andersson P, Erdemir A. Global energy consumption due to friction in passenger cars. *Tribol Int* **47**: 221–234 (2012)

[4] Mukhopadhyay A. Tribology: A potential source of energy savings in industry. *Propag A J Sci Commun* **2**(2): 165–168 (2011)

[5] Nosonovsky M, Bhushan B. Green tribology: Principles, research areas and challenges. *Philos Trans R Soc London Ser A* **368**(1929): 4677–4694 (2010)

[6] Dong C L, Yuan C Q, Wang L, Liu W, Bai X Q, Yan X P. Tribological properties of water-lubricated rubber materials after modification by MoS_2 nanoparticles. *Sci Rep* **6**: 35023 (2016)

[7] Zeng Q F, Dong G N, Martin J M. Green superlubricity of Nitinol 60 alloy against steel in presence of castor oil. *Sci Rep* **6**: 29992 (2016)

[8] Basumatary J, Nie M, Wood R J. The synergistic effects of cavitation erosion-corrosion in ship propeller materials. *J Bio Tribo Corros* **1**(2): 12 (2015)

[9] Celis J P, Ponthiaux P, Wenger F. Tribo-corrosion of materials: Interplay between chemical, electrochemical, and mechanical reactivity of surfaces. *Wear* **261**(9): 939–946 (2006)

[10] Gates R S, Hsu S M. Tribochemistry between water and Si_3N_4 and SiC: Induction time analysis. *Tribol Lett* **17**(3): 399–407 (2004)

[11] Somers A E, Howlett P C, MacFarlane D R, Forsyth M. A review of ionic liquid lubricants. *Lubricants* **1**(1): 3–21 (2013)

[12] Palacio M, Bhushan B. A review of ionic liquids for green molecular lubrication in nanotechnology. *Tribol Lett* **40**(2): 247–268 (2010)

[13] Ye C F, Liu W M, Chen Y X, Yu L Q. Room-temperature ionic liquids: A novel versatile lubricant. *Chem Commun* (21): 2244–2245 (2001)

[14] Qu J, Luo H M, Chi M F, Ma C, Blau P J, Dai S, Viola M B. Comparison of an oil-miscible ionic liquid and ZDDP as a lubricant anti-wear additive. *Tribol Int* **71**: 88–97 (2014)

[15] Anand M, Hadfield M, Viesca J L, Thomas B, Battez A H, Austen S. Ionic liquids as tribological performance improving additive for in-service and used fully-formulated diesel engine lubricants. *Wear* **334–335**: 67–74 (2015)

[16] Khemchandani B, Somers A, Howlett P, Jaiswal A K, Sayanna E, Forsyth M. A biocompatible ionic liquid as an antiwear additive for biodegradable lubricants. *Tribol Int* **77**: 171–177 (2014)

[17] Qu J, Barnhill W C, Luo H M, Meyer III H M, Leonard D N, Landauer A K, Kheireddin B, Gao H, Papke B L, Dai S. Dai, S. Synergistic effects between phosphonium-alkylphosphate ionic liquids and zinc dialkyldithiophosphate (ZDDP) as lubricant additives. *Adv Mater* **27**(32): 4767–4774 (2015)

[18] Somers A E, Khemchandani B, Howlett P C, Sun J Z, MacFarlane D R, Forsyth M. Ionic liquids as antiwear additives in base oils: Influence of structure on miscibility and antiwear performance for steel on aluminum. *ACS Appl*

Mater Interfaces **5**(22): 11544–11553 (2013)

[19] Kong L L, Huang W, Wang X L. Ionic liquid lubrication at electrified interfaces. *J Phys D Appl Phys* **49**(22): 225301 (2016)

[20] Li H, Wood R J, Rutland M W, Atkin R. An ionic liquid lubricant enables superlubricity to be "switched on" in situ using an electrical potential. *Chem Commun* **50**(33): 4368–4370 (2014)

[21] Ismail M, Harvey T, Wharton J, Wood R J K, Humphreys A. Surface potential effects on friction and abrasion of sliding contacts lubricated by aqueous solutions. *Wear* **267**(11): 1978–1986 (2009)

[22] Kelsall G H, Zhu Y Y, Spikes H A. Electrochemical effects on friction between metal oxide surfaces in aqueous solutions. *J Chem Soci Faraday Trans* **89**(2): 267–272 (1993)

[23] Brandon N P, Wood R J K. The influence of interfacial potential on friction and wear in an aqueous drilling mud. *Wear* **170**(1): 33–38 (1993)

[24] Su Y Y, Marek M. Reduction of friction during wire drawing by electrode control. *J Mater Eng Perform* **4**(2): 154–160 (1995)

[25] Chang Q Y, Meng Y G, Wen S Z. Influence of interfacial potential on the tribological behavior of brass/silicon dioxide rubbing couple. *Appl Surf Sci* **202**(1–2): 120–125 (2002)

[26] Meng Y G, Hu B, Chang Q Y. Control of local friction of metal/ceramic contacts in aqueous solutions with an electrochemical method. *Wear* **260**(3): 305–309 (2006)

[27] Chen Y J, Zuo Q Y, Huang P. Influence of electric double layers on elastohydrodynamic lubricating water film in line contact. *Proc Inst Mech Eng Part N J Nanoengineering Nanosyst* **227**(4): 196–198 (2013)

[28] Bai S X, Huang P, Men Y G, Wen S Z. Modeling and analysis of interfacial electro-kinetic effects on thin film lubrication. *Tribol Int* **39**(11): 1405–1412 (2006)

[29] Lantz M A, Wiesmann D, Gotsmann B. Dynamic super-lubricity and the elimination of wear on the nanoscale. *Nat Nanotechnol* **4**(9): 586–591 (2009)

[30] Li J J, Zhang C H, Cheng P, Chen X C, Wang W Q, Luo J B. AFM studies on liquid superlubricity between silica surfaces achieved with surfactant micelles. *Langmuir* **32**(22): 5593–5599 (2016)

[31] Urbakh M, Meyer E. Nanotribology: The renaissance of friction. *Nat Mater* **9**(1): 8–10 (2010)

[32] Rajauria S, Schreck E, Marchon B. Voltage assisted asymmetric nanoscale wear on ultra-smooth diamond like carbon thin films at high sliding speeds. *Sci Rep* **6**: 25439 (2016)

[33] Alazizi A, Draskovics A, Ramirez G, Erdemir A, Kim S H. Tribochemistry of carbon films in oxygen and humid environments: Oxidative wear and galvanic corrosion.

Langmuir **32**(8): 1996–2004 (2016)

[34] Watanabe S, Nakano M, Miyake K, Tsuboi R, Sasaki S. Effect of molecular orientation angle of imidazolium ring on frictional properties of imidazolium-based ionic liquid. *Langmuir* **30**(27): 8078–8084 (2014)

[35] Khan S H, Kramkowski E L, Hoffmann P M. NaCl-dependent ordering and dynamic mechanical response in nanoconfined water. *Langmuir* **32**(42): 10802–10807 (2016)

[36] Riley J K, Tilton R D. Sequential adsorption of nanoparticulate polymer brushes as a strategy to control adhesion and friction. *Langmuir* **32**(44): 11440–11447 (2016)

[37] Phillips B S, Zabinski J S. Ionic liquid lubrication effects on ceramics in a water environment. *Tribol Lett* **17**(3): 533–541 (2004)

[38] Omotowa B A, Phillips B S, Zabinski J S, Shreeve J M. Phosphazene-based ionic liquids: Synthesis, temperature-dependent viscosity, and effect as additives in water lubrication of silicon nitride ceramics. *Inorg Chem* **43**(17): 5466–5471 (2004)

[39] Xie G X, Liu S H, Guo D, Wang Q, Luo J B. Investigation of the running-in process and friction coefficient under the lubrication of ionic liquid/water mixture. *Appl Surf Sci* **255**(12): 6408–6414 (2009)

[40] Zhou Y, Qu J. Ionic liquids as lubricant additives: A review. *ACS Appl Mater Interfaces* **9**(4): 3209–3222 (2017)

[41] Espinosa T, Jiménez M, Sanes J, Jiménez A E, Iglesias M, Bermúdez M D. Ultra-Low friction with a protic ionic liquid boundary film at the water-lubricated sapphire-stainless steel interface. *Tribol Lett* **53**(1): 1–9 (2014)

[42] Gusain R, Gupta P, Saran S, Khatri O P. Halogen-free bis(imidazolium)/ Bis(ammonium)-Di[bis(salicylato)borate] ionic liquids as energy-efficient and environmentally friendly lubricant additives. *ACS Appl Mater Interfaces* **6**(17): 15318–15328 (2014)

[43] Wasserscheid P, Welton T. *Ionic Liquids in Synthesis*. 2nd ed. Weinheim (Germany): Wiley-VCH, 2007.

[44] Li H, Wood R J, Endres F, Atkin R. Influence of alkyl chain length and anion species on ionic liquid structure at the graphite interface as a function of applied potential. *J Phys Condens Matter* **26**(28): 284115 (2014)

[45] Plechkova N V, Seddon K R. *Ionic Liquids Uncoiled: Critical Expert Overviews*. Hoboken, New Jersey (USA): John Wiley & Sons, 2012.

[46] Seddon R K, Annegret S, Torres M J. Influence of chloride, water, and organic solvents on the physical properties of ionic liquids. *Pure Appl Chem* **72**(12): 2275–2287 (2000)

[47] Astarita A, Curioni M, Squillace A, Zhou X, Bellucci F, Thompson G E, Beamish K A. Corrosion behaviour of stainless steel-titanium alloy linear friction welded joints: Galvanic coupling. *Mater Corros* **66**(2): 111–117 (2015)

[48] Dawson J L, Ferreira M G S. Crevice corrosion on 316 stainless steel in 3% sodium chloride solution. *Corros Sci* **26**(12): 1027–1040 (1986)

[49] Sato N. The stability of localized corrosion. *Corros Sci* **37**(12): 1947–1967 (1995)

[50] Dold C, Amann T, Kailer A. Influence of electric potentials on friction of sliding contacts lubricated by an ionic liquid. *Phys Chem Chem Phys* **17**(16): 10339–10342 (2015)

[51] Amann T, Dold C, Kailer A. Potential controlled tribological behavior of water-based ionic liquids. *Key Eng Mater* **674**: 250–256 (2016)

[52] Amann T, Kailer A, Herrmann M. Influence of electrochemical potentials on the tribological behavior of silicon carbide and diamond-coated silicon carbide. *J Bio Tribo Corros* **1**: 30 (2015)

[53] Kailer A, Amann T, Krummhauer O, Herrmann M, Sydow U, Schneider M. Influence of electric potentials on the tribological behaviour of silicon carbide. *Wear* **271**(9–10): 1922–1927 (2011)

[54] Amann T, Kailer A, Krummhauer O, Gumbsch P. Vorrichtung und verfahren zum betrieb eines tribologisch belasteten bauteils. German Patent 102010009507 (Sep. 2011).

[55] Landolt D, Mischler S. *Tribocorrosion of Passive Metals and Coatings*. New Delhi (India): Woodhead Publishing, 2011.

[56] Bidiville A, Favero M, Stadelmann P, Mischler S. Effect of surface chemistry on the mechanical response of metals in sliding tribocorrosion systems. *Wear* **263**(1–6): 207–217 (2007)

[57] Vieira A C, Rocha L A, Papageorgiou N, Mischler S. Mechanical and electrochemical deterioration mechanisms in the tribocorrosion of Al alloys in NaCl and in NaNO$_3$ solutions. *Corros Sci* **54**: 26–35 (2012)

[58] Iwabuchi A, Sonoda T, Yashiro H, Shimizu T. Application of potential pulse method to the corrosion behavior of the fresh surface formed by scratching and sliding in corrosive wear. *Wear* **225–229**: 181–189 (1999)

[59] Sato Y, Iwabuchi A, Uchidate M, Yashiro H. Dynamic corrosion properties of impact-fretting wear in high-temperature pure water. *Wear* **330–331**: 182–192 (2015)

[60] Liu G, Xu Y L, Yang G X, Xiao X S, Chen X K, Zhang X K, Meng X J. Effects of alloy elements on oxidation resistance and stress-rupture property of P92 Steel. *Acta Metall Sin Engl Lett* **28**(2): 129–138 (2015)

[61] Lu J F, Tsai C J. Hydrothermal phase transformation of hematite to magnetite. *Nanoscale Res Lett* **9**(1): 230 (2014)

[62] Molchan I S, Thompson G E, Lindsay R, Skeldon P, Likodimos V, Romanos G E, Falaras P, Adamova G, Iliev B, Schubert T J S. Corrosion behaviour of mild steel in 1-alkyl-3-methylimidazolium tricyanomethanide ionic liquids for CO$_2$ capture applications. *RSC Adv* **4**(11): 5300–5311 (2014)

[63] Otero-Lorenzo R, Weber M C, Thomas P A, Kreisel J, Salgueiriño V. Interplay of chemical structure and magnetic order coupling at the interface between Cr$_2$O$_3$ and Fe$_3$O$_4$ in hybrid nanocomposites. *Phys Chem Chem Phys* **16**(40): 22337–22342 (2014)

Tobias AMANN. He received his Ph.D. degree in chemistry from University of Freiburg, Germany, in 2013. Since then, he is postdoctoral researcher in the Tribology Depart- ment of Fraunhofer Institute for Mechanics of Materials IWM, where his current position is deputy group manager. His main research fields are lubri- cants (liquid crystals, ionic liquids), electrotribology, and tribocorrosion.

Felix GATTI. He received his bachelor and master degrees in chemistry in 2017 from University of Freiburg, Germany. Currently he is a Ph.D. student in the Tribology Department of Fraunhofer Institute for Mechanics of Materials IWM. His research interests include graphene, ionic liquids, and tribocorrosion.

Natalie OBERLE. She received her bachelor degree in mechanical engineering in 2016 from Offenburg University of Applied Sciences, Germany. Currently she is working on her master thesis in the Tribology Department of Fraunhofer Institute for Mechanics of Materials IWM. Her research focuses on the tribological behavior of ionic liquids and hydrogen embrittlement.

Andreas KAILER. He received his doctoral degree in applied mineralogy at University Tübingen, Germany in 1999 and then joined the Tribology Department of Fraunhofer Institute for Mechanics of Materials, where his current position is group manager. His main research fields are tribology of ceramic materials, high temperature tribology, and tribocorrosion.

Jürgen RÜHE. He studied chemistry at the universities of Münster and Mainz. In 1989 he received his Ph.D. degree from the Johannes-Gutenberg University Mainz, Germany. Since 1999 he has a full professor position as the chair for chemistry and physics of interfaces at the Department of Microsystems Engineering (IMTEK) at the University of Freiburg. His main research fields are surfaces, polymer chemistry, and polymer physics.

Electronic Supplementary Material

Galvanically induced potentials to enable minimal tribochemical wear of stainless steel lubricated with sodium chloride and ionic liquid aqueous solution

Tobias AMANN[1*], **Felix GATTI**[1,2], **Natalie OBERLE**[1], **Andreas KAILER**[1], **Jürgen RÜHE**[3]

[1] *Fraunhofer Institute for Mechanics of Materials IWM, Woehlerstr. 11, Freiburg 79108, Germany*

[2] *Institute for Macromolecular Chemistry, University of Freiburg, Freiburg 79104, Germany*

[3] *IMTEK - Department of Microsystems Engineering, University of Freiburg, Georges-Koehler-Allee 103, Freiburg 79110, Germany*

1 Material

Fig. S1   Profile of 1RK91 disk and SiC ball (Wave System T8000, Co. Hommelwerke).
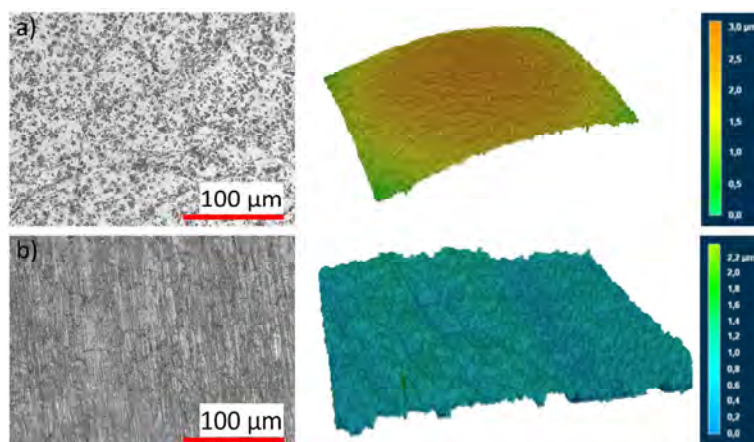
Fig. S2   Surface topography of the used materials using white light interferometry: a) SiC-ball; b) 1Rk91 disk.

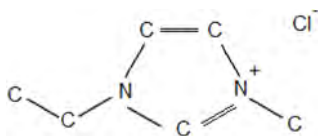* Corresponding author: Tobias AMANN, E-mail: tobias.amann@iwm.fraunhofer.de

Fig. S3 Chemical structure of the water-soluble ionic liquid 1-Ethyl-3-methylimidazolium chloride [C$_2$mim][Cl] (Co. Iolitec).

Table S1 Material characteristics.

Characteristics	1RK91	SiC
Ra (μm)	0.1	<0.1
Rz (μm)	1.0	0.3
E-modulus (GPa)	199	*380-430[1]*
Hardness HV0.031 (GPa)	571	*≥ 2200[1]*

1 supplier information CeramTec

Table S2 Chemical composition of 1RK91 (Co. Sandvik, manufacturer's data).

Element	C	Si	Mn	P	S	Cr	Ni	Mo	Cu	Ti	Al
Content (wt%)	≤0.02	≤0.5	≤0.5	≤0.02	≤0.005	12.0	9.0	4.0	2.0	0.9	0.4

Table S3 Properties ionic liquid 1-Ethyl-3-methylimidazolium chloride [C$_2$mim][Cl] (Co. Iolitec).

Characteristic	
Molecular weight	146.62 g/mol
Empirical formula	C$_6$H$_{11}$ClN$_2$
Melting point	77-79 °C
Purity	>98 %
Water content	5-10 %
Density	1.11 g/cm^3

2 Results

Table S4 Calculated friction work (10 N, 20 Hz, RT, 1 mm, 1 h).

Electrolyte	Material combination	Friction work (N·m)	
1 molar NaCl	1RK91/Cu	411.8	±4%
	1RK91/Al	521.4	±4%
	1RK91/PTFE	357.8	±8%
1 % [C$_2$mim][Cl]	1RK91/Cu	390.6	±3%
	1RK91/Al	520.8	±3%
	1RK91/PTFE	382.4	±2%

Table S5 Wear volume after tribotests (10 N, 20 Hz, RT, 1 mm, 1 h).

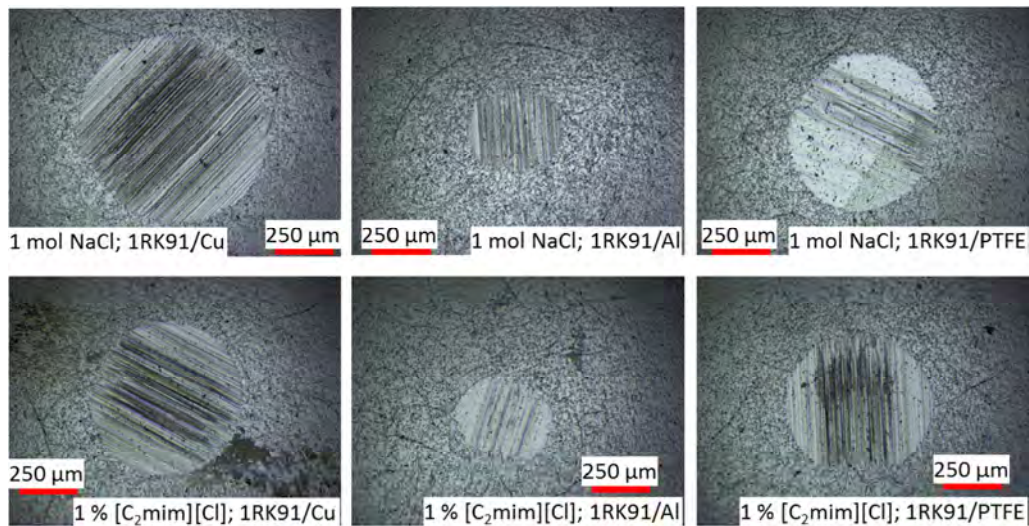| Electrolyte	Material combination	Wear volume (mm³)					
		Ball		Disk		Total	
1 molar NaCl	1RK91/Cu	0.0035	±4%	0.0033	±15%	0.0068	±9%
	1RK91/Al	0.0001	±24%	0.0004	±14%	0.0006	±17%
	1RK91/PTFE	0.0019	±28%	0.0021	±27%	0.0040	±27%
1 % [C$_2$mim][Cl]	1RK91/Cu	0.0015	±3%	0.0011	±39%	0.0026	±18%
	1RK91/Al	0.0002	±2%	0.0004	±8%	0.0006	±6%
	1RK91/PTFE	0.0011	±13%	0.0011	±26%	0.0021	±19%

Fig. S4 Wear analysis of the SiC balls using laser scanning microscope after tribotest (10 N, 20 Hz, RT, 1 mm, 1 h).
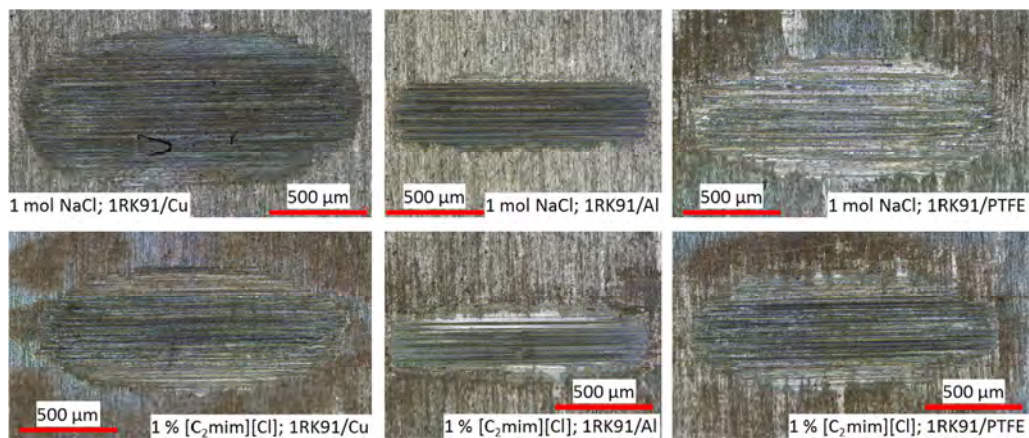

Fig. S5 Wear analysis of the 1RK91 disks using laser scanning microscope after tribotest (10 N, 20 Hz, RT, 1 mm, 1 h).
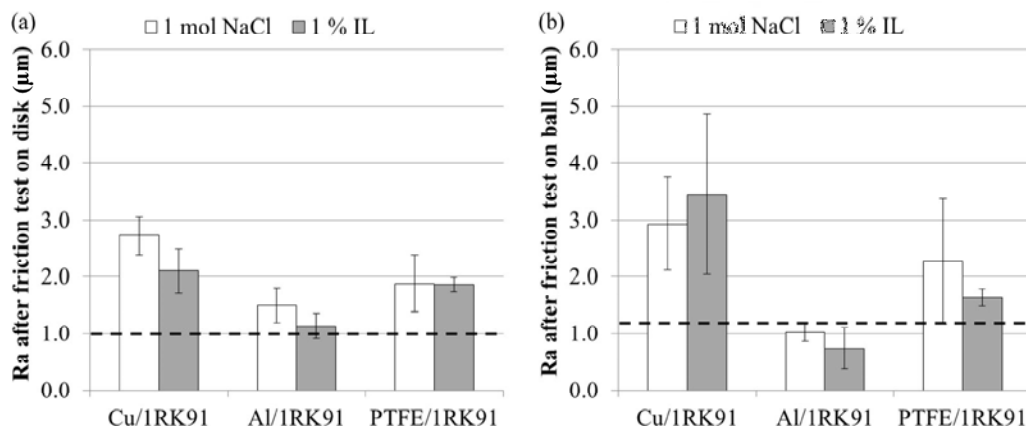

Fig. S6 Surface roughness R_a on wear scar after friction test measured using laser microscope: a) surface roughness on disk; b) surface roughness on ball. Dashed line indicates initial surface roughness of stainless steel 1RK91 disk and SiC ball.
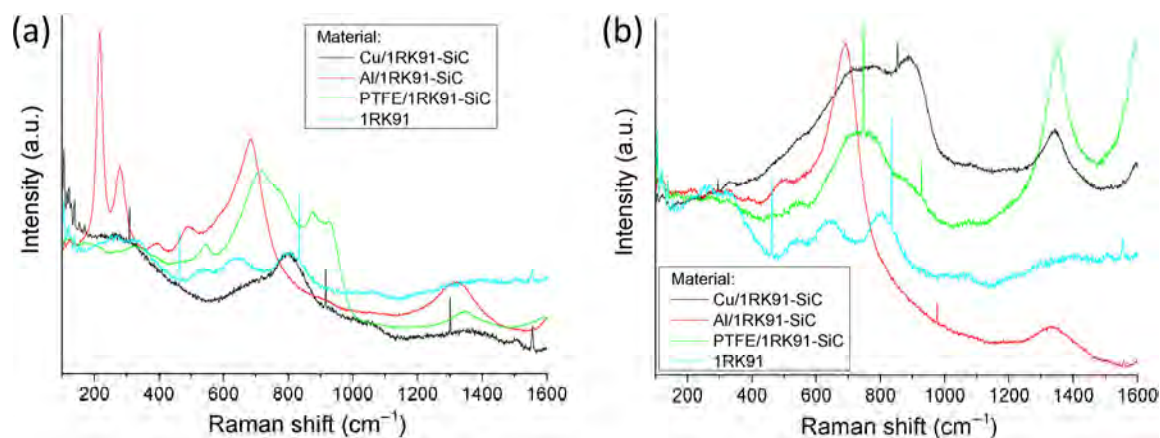
Fig. S7 Wear analysis using Raman-spectroscopy (50×; 3 measurements; 50%) of the 1RK91 disks after tribotest (10 N, 20 Hz, RT, 1 mm, 1 h) with the electrolyte: a) 1 molar NaCl solution; b) 1% [C_2mim][Cl].
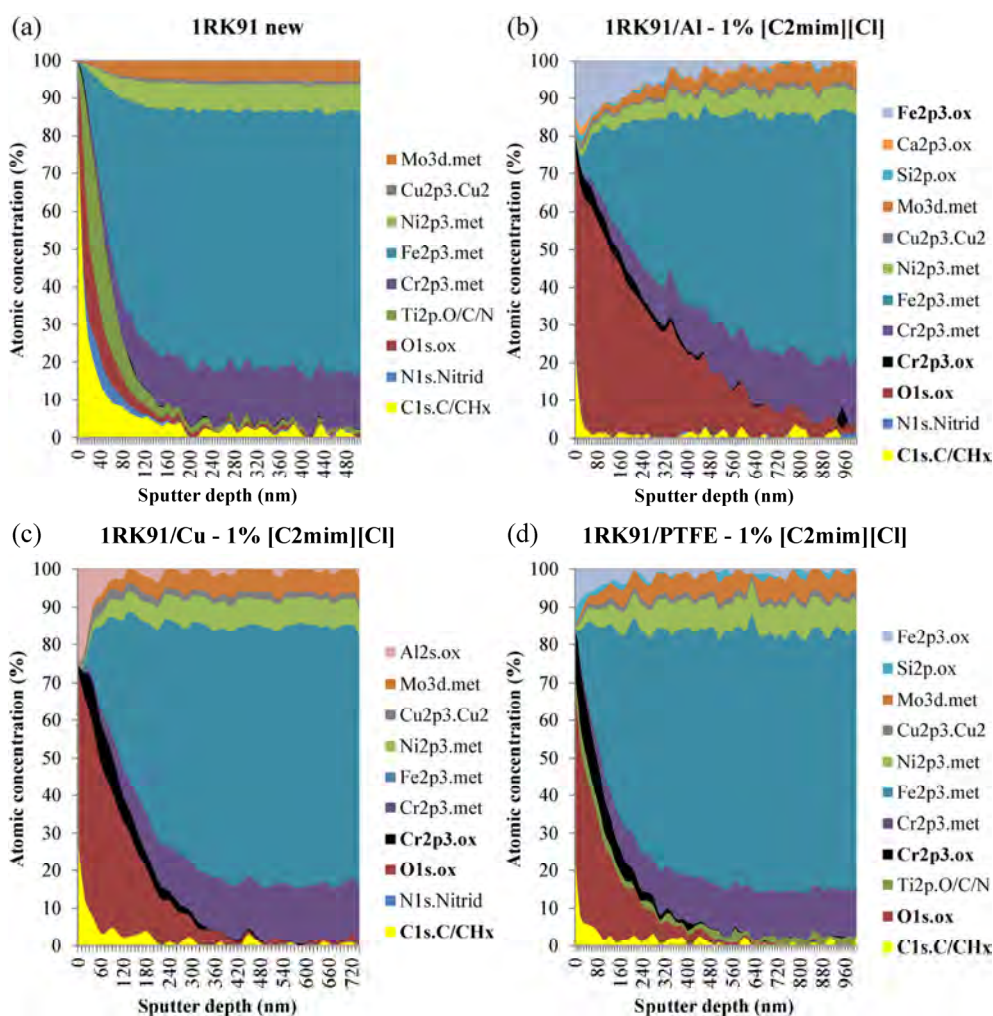

Fig. S8 XPS-analysis of new 1RK91 material a) and wear scars on the disks after tribotest (10 N, 20 Hz, RT, 1 mm, 1 h) using[C_2mim][Cl] with the material combinations: b) 1RK91/Al-SiC; c) 1RK91/Cu-SiC; d) 1RK91/PTFE-SiC.
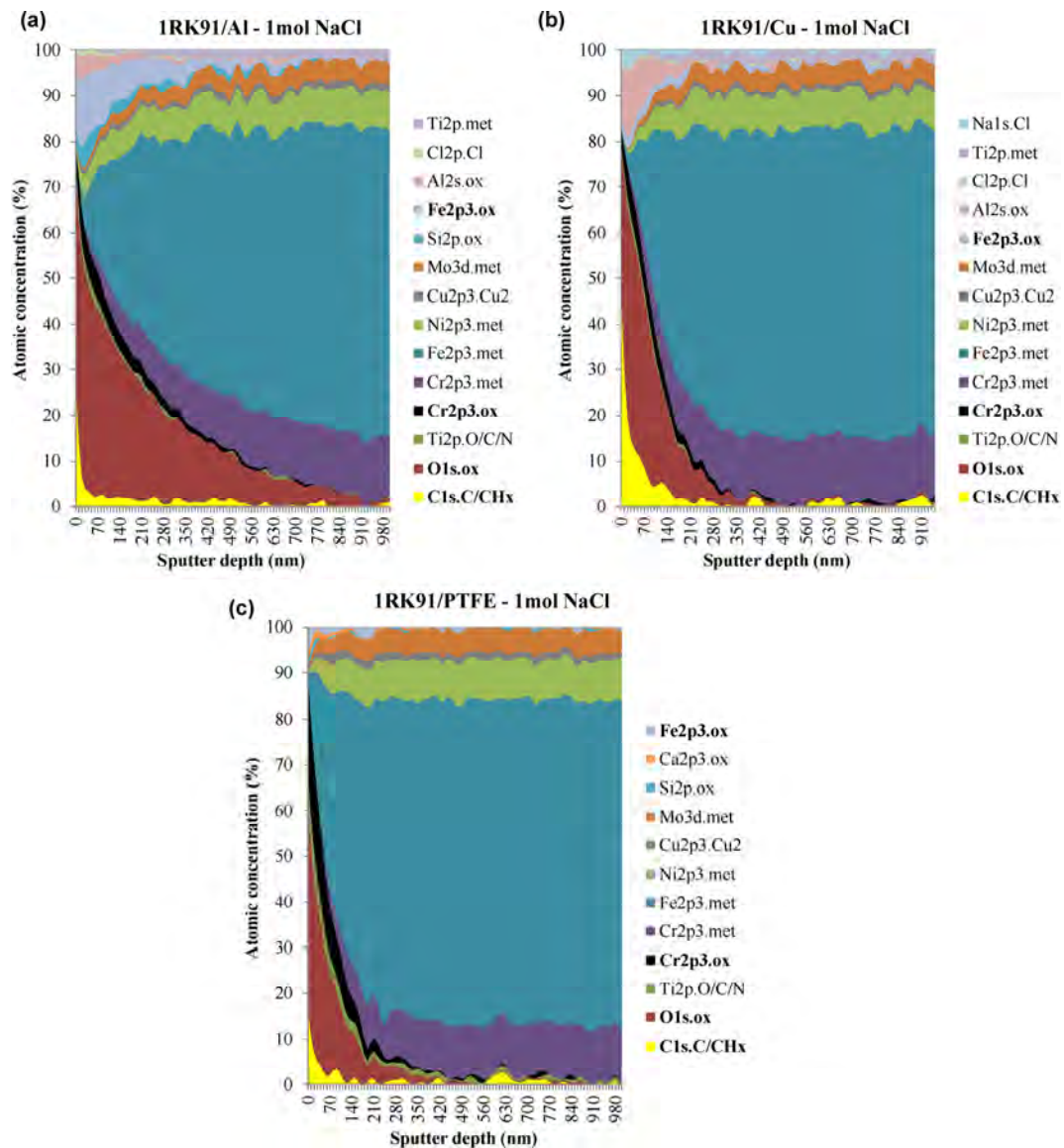
Fig. S9   XPS-analysis of wear scars on the 1RK91 disks after tribotest (10 N, 20 Hz, RT, 1 mm, 1 h) using 1 mol NaCl with the material combinations: a) 1RK91/Al-SiC; b) 1RK91/Cu-SiC; c) 1RK91/PTFE-SiC.